Justus-Liebig-Universität Gießen

I. Physikalisches Institut

# Enzyme-Modified Solution-Gated AlGaN/GaN Field-Effect Transistors for Quantitative Analysis of Covalently Immobilized Enzymes

Dissertation

zur Erlangung des Grades

Doktor der Naturwissenschaften

– Dr. rer. nat. –

vorgelegt dem

Fachbereich 07 - Mathematik und Informatik, Physik, Geographie

von

Diplom-Physikerin

Gesche Mareike Müntze

geboren am

03.02.1985

Gießen 2016

# Abstract

In this work enzyme-modified solution-gated AlGaN/GaN field-effect transistors (EnFETs) were prepared using the enzymes penicillinase (PenFETs) and acetylcholinesterase (AcFETs). Covalent immobilization of the enzymes on the gate surface was carried out via silanization with (3-aminopropyl)triethoxysilane followed by crosslinking with glutaraldehyde. The successful silanization was proven by X-ray photoelectron spectroscopy.

Quantitative analysis of the PenFET response curves at varied measurement conditions demonstrated the applicability of the used kinetic model for pH-sensitive solution-gated EnFETs. The quantitative analysis allowed the determination of the respective Michaelis constant as well as three normalized rate constants which describe the transport of protons, buffer molecules and substrate molecules through the EnFET/enzyme/electrolyte interface.

By evaluation of those four model parameters the influence of buffer concentration and pH-value on the PenFET response curves could be assessed. Furthermore, the extracted model parameters made an investigation of the stability of PenFETs and AcFETs possible. Here, PenFETs could be analyzed with the kinetic model over the course of 252 days while analysis of AcFETs was only feasible over the course of 77 days. In addition, analysis with the kinetic model allowed the quantitative comparison of the response curves of PenFETs and AcFETs, as well as the conclusion that the method used for the enzyme immobilization is highly reproducible.

Based on those results, AcFETs were successfully used for the detection of the neurotransmitter acetylcholine which was released by stimulated neuronal tissue cultivated on the gate surface. In the context of this work three types of neuronal tissue were investigated: isolated myenteric neurons from (4‐12) days old Wistar rats as well as myenteric neurons still embedded in the *muscularis propria* and coeliac ganglia from adult Wistar rats. In all casees, the response of an AcFET towards the release of acetylcholine could be linked to the activ-

ity of the covalently immobilized acetylcholinesterase by utilizing the reversible acetylcholinesterase blocker donepezil. These results demonstrate the realization of a functional neuron/AcFET hybrid.

# Zusammenfassung

In der vorliegenden Arbeit wurden Enzym-funktionalisierte AlGaN/GaN Feldeffekttransistoren (EnFETs) mit einem elektrolytischen Gate unter Verwendung der Enzyme Penicillinase (PenFETs) und Acetylcholinesterase (AcFETs) hergestellt. Die kovalente Anbindung der Enzyme an die Gateoberfläche erfolgte dabei durch Silanisierung mit 3-Aminopropyltriethoxysilan, gefolgt von der Verwendung des Crosslinkers Glutaraldehyd. Die Charakterisierung mittels Röntgenphotoelektronenspektroskopie zeigte die erfolgreiche kovalente Anbindung der Funktionalisierungsschicht.

Durch quantitative Analyse der PenFET Antwortkurven bei unterschiedlichen Messbedingungen konnte nachgewiesen werden, dass das verwendete kinetische Model für zur Modellierung von pH-sensitiven EnFETs mit einem elektrolytischen Gate ausgezeichnet geeignet ist. Anhand dieser Analyse war es möglich die Michaelis-Menten-Konstanten der Enzyme und drei normalisierte Geschwindigkeitskonstanten zu bestimmen, die den Transport von Protonen, Puffermolekülen und Substratmolekülen durch die EnFET/Enzym/Elektrolyt-Grenzfläche quantitativ beschreiben.

Mit Hilfe dieser vier Parameter wurde der Einfluss des pH-Wertes und der Pufferkonzentration auf die Antwortkurven von PenFETs sowie die Langzeitstabilität der AcFETs und PenFETs untersucht. Hierbei zeigte sich, dass PenFETs über einen Zeitraum von 252 Tagen auswertbare Antwortkurven lieferten, wohingegen AcFETs nur über einen Zeitraum von 77 Tagen messbar waren. Des Weiteren erlaubte die Analyse mit dem kinetischen Modell einen direkten quantitativen Vergleich der Antwortkurven der beiden EnFETs und ließ die Schlussfolgerung zu, dass die zur Enzym-Funktionalisierung verwendete Methode in hohem Maße reproduzierbar ist.

Auf Grundlage dieser Ergebnisse konnten AcFETs erfolgreich dazu benutzt werden, die Ausschüttung des Neurotransmitters Acetylcholin durch stimuliertes neuronales Gewebe, das auf der Gateoberfläche der AcFETs kultiviert

wurde, zu erfassen. Für diese Arbeit wurden isolierte myenterische Neuronen von acht bis zwölf Tage alten Wistar-Ratten, sowie *Ganglia coeliacum* und noch im Gewebe eingebettete myenterische Neuronen von ausgewachsenen Wistar-Ratten untersucht. In allen drei Fällen konnte durch die Verwendung des reversiblen Acetylcholinesteraseblockers Donepezil die Reaktion des AcFETs auf die Ausschüttung von Acetylcholin mit der Aktivität der kovalent auf der Gateoberfläche angebundenen Acetylcholinesterasen eindeutig in Verbindung gebracht werden. Die Realisierbarkeit einer funktionalen Neuron/AcFET-Hybridstruktur konnte somit gezeigt werden.

# Danksagung

An dieser Stelle möchte ich mich bei allen bedanken, die mich während meiner Promotion begleitet und unterstützt haben.

Mein herzlicher Dank gilt...

...Prof. Dr. Martin Eickhoff für die Möglichkeit dieses interdiziplinäre Dissertationthema in seiner Arbeitsgruppe zu bearbeiten. Du hast mich gefordert, gefördert und mir auch gesagt, wenn ich mal über das Ziel hinaus geschossen bin. Deine Denkanstöße und unsere fachlichen Diskussion haben wesentlich zum Gelingen dieser Arbeit beigetragen. Danke für Dein Vertrauen und die langjährige Unterstützung.

...Prof. Dr. Martin Diener vom Institut für Veterinär-Physiologie und -Biochemie für die erfolgreiche Zusammenarbeit bei der Realisierung einer Neuron/AcFET-Hybridstruktur und die Einführung in das Fachgebiet der Physiologie. Danke auch für ihre Bereitschaft das Korreferat dieser Arbeit zu übernehmen.

...Prof. Dr. Jürgen Janek und Prof. Dr. Markus Thoma für ihre Zusagen teil der Prüfungskommission zu sein.

...Dr. Julia Steidle und Ervice Pouokam, Ph.D. für ihre tatkräftige Unterstützung bei der Durchführung der Messungen neuronaler Aktivität und die Bereitstellung ihres Fachwissens. Ervice, du hast meinen Fragen sowie unseren fachlichen Diskussionen immer viel Zeit gewidmet und warst dabei stets voller Humor und Optimismus.

...der Arbeitsgruppe von Prof. Dr. Stefan Krischok an der Technischen Uni-

Verlass.

...allen Mitarbeitern des I. Physikalischen Instituts und der Arbeitsgruppe von Prof. Dr. Martin Diener für die gute Zusammenarbeit sowie das Teilen eures Wissens und eurer Fähigkeiten.

...meiner Familie für die immerwährende Unterstützung bei und neben der Promotion.

...Jochen Reinacher. Du hast mich ertragen, auch wenn ich bei allem Stress doch manchmal unausstehlich war. Du hast mich aufgebaut, wenn es gerade mal nicht so lief und mich immer daran erinnert, dass es wirklich irgendwann ein Ende hat. Danke!

# Table of Contents

*Table of Contents*

# List of Abbreviations

| | |
|---|---|
| 2DEG | two-dimensional electron gas |
| $\Delta U_{\mathrm{GS}}$ | change of the gate-source voltage |
| acetyl-CoA | acetyl coenzyme A |
| AcFET | acetylcholinesterase-modified AlGaN/GaN field-effect transistor |
| ACh | acetylcholine |
| AChE | acetylcholinesterase |
| ALD | atomic layer deposition |
| APTES | (3-aminopropyl)triethoxysilane |
| ATCh | acetylthiocholine |
| [ATCh] | acetylthiocholine concentration |
| B | base |
| BF | deprotonated buffer |
| $[\mathrm{BF}]^{\mathrm{E}}$ | buffer concentration in the bulk electrolyte |
| BSA | bovine serum albumin |
| $\mathrm{Ca_V}$ channels | voltage-gated calcium channels |
| Ch | choline |
| ChAT | choline acetyltransferase |
| CPA | cyclopiazonic acid |
| DNA | deoxyribonucleic acid |
| E | enzyme |
| $[\mathrm{E}]_0$ | density of enzymes on the gate area |
| EnFET | enzyme-modified field-effect transistor |
| ES | enzyme-substrate complex |
| FET | field-effect transistor |
| H | proton |
| [H] | proton concentration in the enzyme layer |
| $[\mathrm{H}]^{\mathrm{E}}$ | proton concentration in the bulk electrolyte |
| HA | acid |

| | |
|---|---|
| HBF | buffer |
| HBSS | Hanks' balanced salt solution |
| HEMT | high electron mobility transistor |
| HP | product |
| $IC_{50}$ | half maximal inhibitory concentration |
| $I_{DS}$ | drain-source current |
| $k_{BF}$ | transport rate constant of buffer |
| $\bar{k}_{BF}$ | normalized rate constant of buffer |
| $k_{H}$ | transport rate constant of protons |
| $\bar{k}_{H}$ | normalized rate constant of protons |
| $K_{M}$ | Michaelis constant |
| $k_{S}$ | transport rate constant of substrate |
| $k_{V}$ | normalized rate constant of the maximum reaction velocity of the enzymatic reaction |
| MAP2 | microtubule-associated protein 2 |
| N | non-protolytic product |
| nAChR | nicotinic acetylcholine receptors |
| P | deprotonated product |
| PBS | phosphate buffered saline |
| PenFET | penicillinase-modified AlGaN/GaN field-effect transistor |
| $s$ | sensitivity |
| S | substrate |
| [S] | substrate concentration in the enzyme layer |
| $[S]^{E}$ | substrate concentration in the bulk electrolyte |
| SGFET | solution-gated field-effect transistor |
| SNAP-25 | synaptosomal-associated protein 25 |
| SNARE | synaptosomal-associated protein receptor |
| $U_{DS}$ | drain-source voltage |
| $U_{GS}$ | gate-source voltage |
| $v_{max}$ | maximum reaction velocity of the enzymatic reaction |
| XPS | X-ray photoelectron spectroscopy |

# 1 Introduction

Biosensors are combinations of biochemical recognition elements and transducers [1] as schematically shown in Figure 1.1. The biochemical recognition element contributes its immanent specificity and selectivity while the transducer is responsible for the transfer of the biological signal generated by the biochemical recognition element into a readout. This readout can then be quantified by standard measuring techniques mainly in the electric domain, *id est* potentiometry, amperometry, conductometry and impedance measurement techniques [1]. Examples for the biochemical recognition element are enzymes [2], deoxyribonucleic acid (DNA) strands [3] or antibodies [4] which will generate a biological signal if exposed to an appropriate analyte.
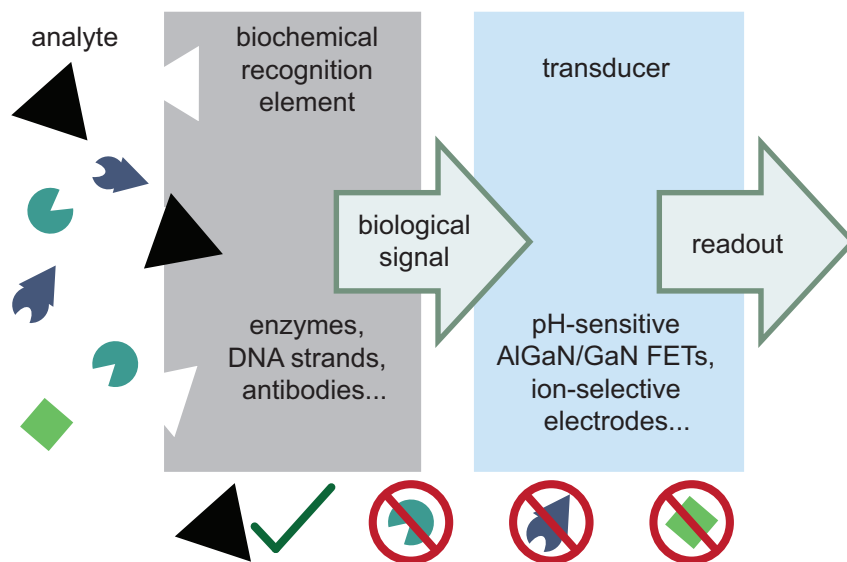


*Figure* 1.1 *Schematic representation of a biosensor.*

The commencements of biosensor research can be attributed to Clark and Lyons who devised an electrode system to monitor blood oxygen and carbon

dioxide levels as well as the blood pH of a patient during cardiovascular surgery in the 1960s [5]. Within the context of this work one finds as well first considerations of the use of enzyme-containing membranes in an electrode cell for the detection of glucose in whole blood. Since controlling the blood glucose level is as well crucial for diabetic patients, the high prevalence of diabetes was co-responsible for the emerging field of biosensor research, especially with regard to glucose sensing by means of the enzyme glucose oxidase [6].

At present, the interest in development, fabrication and characterization of biosensors is increasing [7] while the application area of biosensors has become diverse, including drug development [8, 9, 10], diagnostics [11, 12] and protein detection [4, 13].

Besides the detection of glucose with glucose oxidase-based biosensors, the development of acetylcholinesterase (AChE)-based biosensors has progressed especially with regard to their applicability in toxicity monitoring [14]. As the inhibition of AChE leads to an accumulation of the neurotransmitter acetylcholine (ACh) and thus dysfunction in the cholinergic neurotransmission [15, 16]; AChE-based biosensors can be used for the study of AChE inhibitors such as organophosphorus pesticides [17, 18, 19, 20] and other neurotoxins [21]. Another application field for AChE-based biosensors is the detection and quantification of the neurotransmitter ACh itself. This application is particularly important for geriatric medicine as a decreased level of brain ACh can be associated with memory disturbance [22]. In this context, the determination of ACh and the related choline acetyltransferase (ChAT) activity give insight into the pathogenesis of diseases such as Parkinson's disease [23] and Alzheimer's disease [24, 25, 26].

Since ACh is not only produced by cholinergic neurons but also by non-neuronal cells such as the urothelium [27], the colonic epithelium [28] and the airway epithelium [29], the detection of ACh also plays a role in the study of the non-neuronal cholinergic system [30].

At present, mainly methods sensitive in the (sub-)nmol-range are used to prove the cellular production and/or the release of ACh. Examples are liquid chromatography combined with the electrochemical detection of hydrogen peroxide [31], matrix-assisted laser desorption ionization time-of-flight mass spectrometry [32] and liquid chromatography in combination with electrospray ionization mass spectrometry [33]. Although being highly sensitive, these methods only offer a time resolution on the minute scale and *in situ* application is not pos-

sible. In contrast, AChE-based biosensors offer the advantage of possible *in situ* analysis with a time resolution on the (sub-)second scale [34]. The operating principles of AChE-based biosensors developed so far are diverse. Among those are fluorometric [19, 35, 36], amperometric [21, 25, 37, 38, 20] and potentiometric [18, 39, 34, 40, 41] biosensors. However, none of these sensors has been used for the actual *in situ* detection of ACh.

This *in situ* detection is demonstrated in the present work by utilizing an AChE-modified AlGaN/GaN field-effect transistor (AcFET), *id est* a potentiometric AChE-based biosensor, with an ACh detection limit of $1\,\mu M$ for the detection of ACh released by stimulated neurons. The thus obtained interface which transfers the neuronal activity, represented by the release of ACh, into an electric readout - here a change in the conductance of the AlGaN/GaN FET - is termed a neuron/AcFET hybrid as schematically depicted in Figure 1.2. One should note that the here discussed concept for monitoring neuronal activity is distinguished from concepts that use FETs for the detection of the electric field created by neuronal activity as done in the work of Fromherz *et al.* [42]. A more detailed description of a neuron/AcFET hybrid is outlined in section 2.3.
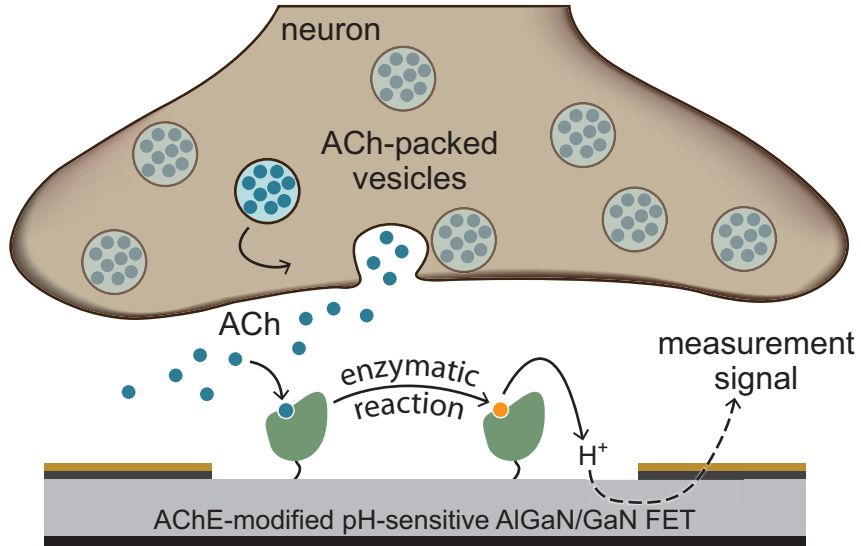


*Figure* 1.2 *Schematic of a neuron/AcFET hybrid. The neurotransmitter ACh released by the neuron is enzymatically degraded by the AChEs covalently bound the gate surface of the AlGaN/GaN FET. This leads to a change in pH which can be measured by the pH-sensitive AcFET.*

The basis for the AcFET sensing ACh and thus for its applicability in a neu-

ron/AcFET hybrid is the pH-sensitivity of AlGaN/GaN FETs which is discussed in section 2.1. Furthermore, AlGaN/GaN FETs show biocompatibility [43, 44, 45, 46] and chemical stability in aqueous electrolytes [47, 48] which are crucial requirements of the transducer for being suitable for a neuron/AcFET hybrid.

Besides the immanent properties of AlGaN/GaN FETs, the AcFET characteristics have to be investigated to ensure their functionality for experiments monitoring neuronal activity. Out of this reason, the AcFETs are quantitatively analyzed with regard to their stability and the reproducibility of the preparation method in section 4.2 by means of a kinetic model which is outlined in section 2.2.

Before, the validity of this model is assessed for the example of penicillinase-modified AlGaN/GaN FETs (PenFETs) in section 4.1. Here, the analysis based on the kinetic model allows quantification of their reproducibility and stability, as well as a quantitative discussion of the influence of pH and buffer concentration on the properties of the enzyme layer in terms of the Michaelis constant and three normalized rate constants which give insight into the kinetics of the FET/enzyme/electrolyte system.

In combination with the preparation method for AcFETs and PenFETs shown in sections 3.1 and 3.2, the kinetic model by Glab *et al.* [49] can even be used for the quantitative comparison of the response curves of PenFETs and AcFETs as shown in section 4.2. So far, quantitative comparison of different EnFET devices and their characteristics could not be shown even if the FETs used for enzyme-modified FETs (EnFETs) were prepared using standard silicon processing technology [50, 51, 52, 53, 54, 55]. A possible reason for this is that differing functionalization methods have been employed for enzyme immobilization, such as physisorption [53], aggregation with bovine serum albumin [50, 51, 55] and covalent binding with pyrroloquinoline quinine [52] or with glutaraldehyde on a hydrated $Si_3N_4$ surface [54]. In contrast to the preparation method used in this work (cf. section 3.2) those methods yield thick and hardly reproducible enzyme layers. Hence, the response curves of the thus prepared EnFETs are controlled by diffusion processes and modeling requires mathematically complex calculations of the concentration profiles within the enzyme layer [56, 57, 58, 59]. This requires in turn a detailed knowledge of the geometry of the enzyme layer, which is generally not known. Consequently, an application of diffusion models for quantitative comparison is difficult.

Subsequent to the quantitative characterization of PenFETs and AcFETs by means of the kinetic model by Glab *et al.* in sections 4.1 and 4.2, experiments for monitoring neuronal activity were conducted and analyzed according to the eligible measurement and evaluation routines stated in section 3.4. Within section 4.3, monitoring of neuronal activity could be shown on the examples of myenteric neurons still embedded in the *muscularis propria*, isolated myenteric neurons and a coeliac ganglion while their respective preparation is described in section 3.3. Further, it was possible to confirm the viability of the biological samples during and after the experiment by testing the samples' vitality according to the assays described in section 3.5.

In summary, the two main objectives of the presented work are the establishment of the kinetic model by Glab *et al.* as a suitable tool for the quantitative analysis of AlGaN/GaN EnFETs - even allowing the direct comparison of PenFETs and AcFETs - and the realization of a neuron/AcFET hybrid by utilizing an AlGaN/GaN AcFET with a ACh detection limit of $1\,\mu M$.

# 2 Fundamentals

In this introductory chapter a brief overview of the fundamental concepts needed to understand the content of this work is given.

The chapter starts with a compact introduction to the properties of AlGaN/GaN FETs, elucidating the formation of a two-dimensional electron gas (2DEG) in a $GaN/Al_xGa_{1-x}N/GaN$ heterostructure and the pH-sensitivity of solution-gated GaN/AlGaN/GaN field-effect transistors (GaN/AlGaN/GaN SGFETs). This pH-sensitivity is the basis for the application as EnFETs and allows the utilization of the kinetic model for pH-sensitive EnFETs from Glab *et al.* [49] that is outlined in the second section. Then, the chapter is concluded by illustrating the concept of a neuron/AcFET hybrid used to monitor neuronal activity by means of the released neurotransmitter ACh.

## 2.1 Properties of AlGaN/GaN Field-Effect Transistors

Group III-nitrides exist in the wurtzite and in the zinc blende crystal structure whereof the zinc blende crystal structure is the thermodynamically metastable phase [60]. The wurtzite crystal structure can be described by the lattice parameters $a_0$ and $c_0$ as well as the parameter $u_0$ which defines the distance between a nitrogen atom and the respective group III-atom along the $c$-direction in terms of $c$ as shown in Figure 2.1 on the example of GaN. If the $c$-direction coincides with the growth direction of *exempli gratia* GaN the polarity of the crystal is Ga-face whereas N-face polarity is obtained when growing anti-parallel to the $c$-direction.

In the wurtzite crystal structure each group III-atom is surrounded by four nitrogen atoms, and *vice versa*, forming a tetrahedron as shown in Figure 2.1a) for a gallium atom surrounded by four nitrogen atoms. As the electronegativ-

6

ity $\chi$ of nitrogen ($\chi$ = 3.04 [61]) is greater than the electronegativity of gallium ($\chi$ = 1.81 [61]) four microscopic dipoles arise within the tetrahedron which point towards the more electronegative nitrogen atom.

Compared to an ideal mathematical tetrahedron the tetrahedrons in wurtzite group III-nitrides are compressed along the $c$-direction while elongated in the $c$-plane. Hence, the microscopic dipoles do not compensate each other. In addition, the wurtzite crystal structure is non-centrosymmetric. Thus, the microscopic dipoles of each tetrahedron cannot cancel each other, resulting in a macroscopic spontaneous polarization $P_{\mathrm{SP}}$ antiparallel to the $c$-direction as shown in Figure 2.1b).
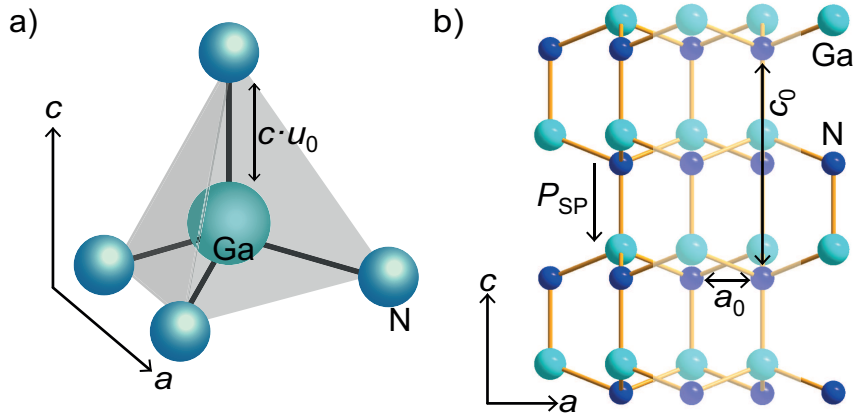


*Figure* 2.1 *Schematic illustration of a) the tetrahedral coordination of Ga and N atoms and b) the direction of the spontaneous polarization in wurtzite GaN. The direction of the a-axis and the c-axis are given.*

In case of GaN the spontaneous polarization is $-0.029\,\mathrm{C\,m^{-2}}$ and thus about 2.8 times smaller than the spontaneous polarization of AlN [62]. The reason for this is the greater difference in electronegativity of nitrogen and aluminum ($\Delta\chi$ = 1.63 [61]) compared to nitrogen and gallium ($\Delta\chi$ = 1.43) as well as the increase in the parameter $u_0$ from 0.376 to 0.380 (cf. Table 2.1). Concomitantly, the ratio $c_0/a_0$ decreases for AlN resulting in a higher microscopic dipole for each tetrahedron and thus an overall greater spontaneous polarization of AlN. Consequently, the spontaneous polarization of the alloy $\mathrm{Al}_x\mathrm{Ga}_{1-x}\mathrm{N}$, $P_{\mathrm{SP}}(x)$, is greater than the one of GaN. It can be calculated by assuming a linear dependency on the aluminum content $x$ according to equation 2.1 based on Vegard's law [63].

$$P_{\mathrm{SP}}(x) = (-0.029 - 0.52x)\,\mathrm{C\,m^{-2}} \tag{2.1}$$

In addition to spontaneous polarization, wurtzite epitaxial (Al, Ga)N thin films can exhibit piezoelectric polarization $P_{PE}$ oriented along the *c*-direction when the crystal is strained as discussed on the example of a GaN/Al$_x$Ga$_{1-x}$N/GaN heterostructure as shown in Figure 2.2.

*Table* 2.1 *Relevant band structure parameters for wurtzite GaN and AlN.*

| parameter | | GaN [reference] | | AlN [reference] | |
|---|---|---|---|---|---|
| $E_{gap}$ (0 K) | [eV] | 3.51 | [64] | 6.23 | [64] |
| $E_{gap}$ (300 K) | [eV] | 3.42 | [65] | 6.13 | [65] |
| | | | | | |
| $a_0$ (300 K) | [Å] | 3.189 | [63] | 3.112 | [63] |
| $c_0$ (300 K) | [Å] | 5.185 | [63] | 4.982 | [63] |
| $c_0/a_0$ | | 1.626 | [63] | 1.601 | [63] |
| $u_0$ | | 0.376 | [62] | 0.380 | [62] |
| | | | | | |
| $P_{SP}$ | [C m$^{-2}$] | −0.029 | [62] | −0.081 | [62] |
| $e_{31}$ | [C m$^{-2}$] | −0.49 | [62] | −0.60 | [62] |
| $e_{33}$ | [C m$^{-2}$] | 0.73 | [62] | 1.46 | [62] |
| $C_{13}$ | [GPa] | 106 | [66] | 108 | [67] |
| $C_{33}$ | [GPa] | 398 | [66] | 373 | [67] |

Up to a layer thickness $d$ of $(30 \pm 5)$ nm with a maximum aluminum content $x = (0.38 \pm 0.03)$ the Al$_x$Ga$_{1-x}$N layer grown on the subjacent GaN layer is pseudomorph [68]. Hence, the Al$_x$Ga$_{1-x}$N layer exhibits compressive strain along the growth direction and tensile strain perpendicular to the growth direction (cf. Figure 2.2) for $d < 30$ nm and $x < 0.38$. This results in a further distortion of the tetrahedrons which leads to an additional polarization, termed piezoelectric polarization $P_{PE}$. The magnitude and orientation of $P_{PE}$ can be calculated by Eq. 2.2 [63].

$$P_{PE}(x) = 2 \cdot \frac{a_{strained}(x) - a_0(x)}{a_0(x)} \left( e_{31}(x) - e_{33}(x) \cdot \frac{C_{13}(x)}{C_{33}(x)} \right) \qquad (2.2)$$

For solving Eq. 2.2, the piezoelectric constants $e_{31}(x)$ and $e_{33}(x)$, the elastic constants $C_{13}(x)$ and $C_{33}(x)$ as well as the lattice parameter $a_0(x)$ are obtained by linear interpolation of the respective values given for GaN ($x = 0$) and AlN ($x = 1$) in Table 2.1 following Vegard's law [68].

In case of tensile strain perpendicular to the growth direction, *id est* $[a_{strained}(x) - a_0(x)] > 0$, $[e_{31}(x) - e_{33}(x) \cdot C_{13}(x)/C_{33}(x)] < 0$ for all values

of $x$. Hence, $P_{PE} < 0$ and $P_{PE} \parallel P_{SP}$ (cf. Figure 2.2). It follows that the total polarization of the $Al_xGa_{1-x}N$ layer, $P(x) = P_{SP}(x) + P_{PE}(x)$, is significantly higher than the total polarization of each non-strained GaN layer $P(0) = P_{SP}(0)$ in the absence of external electric fields [62].

In analogy to the divergence of the electric polarization inducing a negative charge density $-\rho = \vec{\nabla}\vec{P}$, the abrupt change in the magnitude of polarization at a $GaN/Al_xGa_{1-x}N$ heterojunction causes a sheet charge density $\sigma$ at this interface. Its absolute value can be calculated by Eq. 2.3 [63].

$$
\begin{aligned}
|\sigma(x)| &= |P(x) - P(0)| \\
&= |P_{PE}(x) + P_{SP}(x) - P_{SP}(0)| \\
&= \left| 2 \cdot \frac{a - a_0(x)}{a_0(x)} \left( e_{31}(x) - e_{33}(x) \cdot \frac{C_{13}(x)}{C_{33}(x)} \right) + P_{SP}(x) - P_{SP}(0) \right|
\end{aligned}
\tag{2.3}
$$

In case of the Ga-face $GaN/Al_xGa_{1-x}N/GaN$ heterostructure shown in Figure 2.2a), the lower $GaN/Al_xGa_{1-x}N$ interface closer to the substrate carries a positive sheet charge density $+\sigma$ while the second (upper) $Al_xGa_{1-x}N/GaN$ interface carries a negative sheet charge density $-\sigma$. For a N-face $GaN/Al_xGa_{1-x}N/GaN$ heterostructure the sign of $\sigma$ is inverted at all interfaces (cf. Figure 2.2b)).
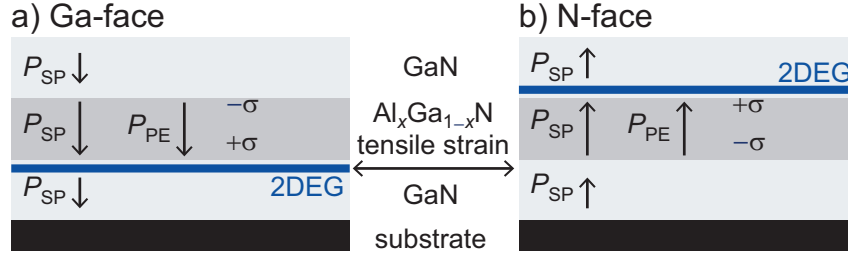


*Figure* 2.2 *Directions of spontaneous and piezoelectric polarization, $P_{SP}$ and $P_{PE}$, respectively, as well as the thus induced sheet charge density $\sigma$ of a pseudomorph $GaN/Al_xGa_{1-x}N/GaN$ heterostructure at the respective interfaces with a) Ga-face polarity and b) N-face polarity. The position of the 2DEG as well as the direction of the tensile strain in the $Al_xGa_{1-x}N$ layer are indicated also.*

As shown in Figure 2.3, the surface charges at the interfaces of the $Al_xGa_{1-x}N$ layer generate an electric field $\vec{E}$ which is in the order of $1\,MV\,cm^{-2}$ [63] and thus 10 times stronger than in other group III-V semiconductors [69]. Due to this electric field the conduction band and valence band are tilted. Free

electrons within the $Al_xGa_{1-x}N$ layer follow the electric field and compensate the positive sheet charge density at the respective $GaN/Al_xGa_{1-x}N$ interface. Thus, a 2DEG is formed if the triangular quantum well at the respective interface drops below the Fermi level $E_F$ [68].
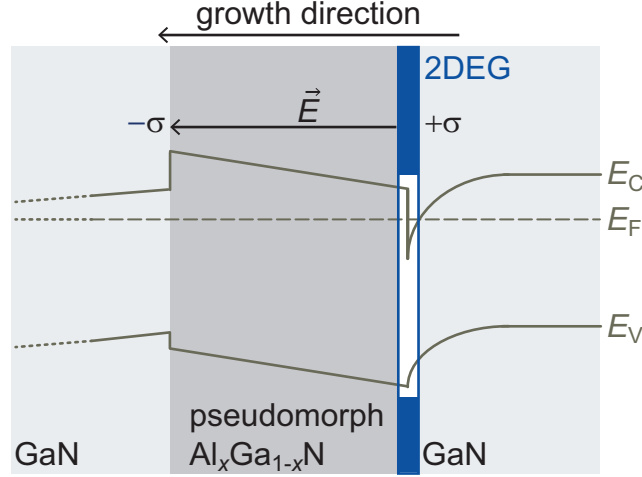


*Figure* 2.3 *Schematic representation of the band profile of a Ga-face $GaN/Al_xGa_{1-x}N/GaN$ heterostructure with the direction of the electric field $\vec{E}$ within the $Al_xGa_{1-x}N$ layer indicated. The boundary conditions for GaN in growth direction are not defined as represented by the dotted lines.*

Associated with the formation of a 2DEG is the sheet carrier concentration $n_S$ which depends on the aluminum content $x$, the thickness of the $Al_xGa_{1-x}N$ layer $d$ and the temperature $T$ as follows if all other parameters are fixed:

- With decreasing $T$, first $n_S$ decreases exponentially as carriers "freeze out" while for $T < 100\,K$ $n_S$ remains unaffected by changes in $T$ [70].

- With increasing $d$, $n_S$ increases [63].

- With increasing $x$, $n_S$ increases [63, 70].

Typical values for $n_S$ at $300\,K$ are in the order of $10^{13}\,cm^{-2}$ for $x \leq 0.4$ and $d$ up to $30\,nm$ [63] with a corresponding mobility of electrons in the 2DEG, $\mu_S$, of about $10^3\,cm^2\,V^{-1}\,s^{-1}$ [70]. Thus, transistors fabricated from $GaN/Al_xGa_{1-x}N/GaN$ heterostructures are high electron mobility transistors (HEMTs).

Figure 2.4 shows that $\mu_S$ increases with $T$ until it reaches constant values from $T \lesssim 100\,K$ which are decreasing with increasing $d$. In case of the $3\,nm$ sample

as well as in the case of the template, the decrease in $\mu_S$ for $T < 100\,\mathrm{K}$ is assigned to the absence of a 2DEG [70].
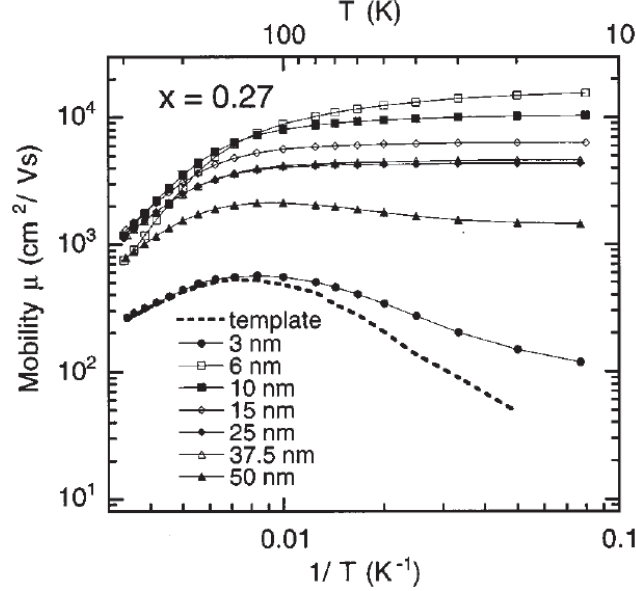


*Figure* 2.4 *Temperature-dependent electron mobility in $Al_{0.27}Ga_{0.73}N/GaN$ heterostructures with AlGaN barriers of different thickness. Reprinted with permission from [70]. Copyright 1999, AIP Publishing LLC.*

The increase in $\mu_S$ is attributed to the vanishing influence of optical phonon scattering which limits $\mu_S$ at room temperature [71]. For $T < 100\,\mathrm{K}$, $\mu_S$ is governed by interface roughness scattering and alloy disorder scattering [70]. The influence of both scattering mechanisms increases with increasing $n_S$. Hence, their influence depends as well on $d$ (cf. Figure 2.4) and $x$ as the increase of $d$ and/or $x$ leads to an increase in $n_S$ [63]. As a result of the increase in $n_S$ the electron wave function is located closer to the $Al_xGa_{1-x}N/GaN$ interface and thus penetrates deeper into the $Al_xGa_{1-x}N$ layer [70]. Hence, interface roughness scattering becomes dominant [72]. However, this scattering mechanism can be reduced by interfaces of high crystal quality [73] as well as the insertion of a thin AlN blocking layer at the $Al_xGa_{1-x}N/GaN$ interface [74]. Besides increasing $n_S$, an increase in $x$ also leads to an increases of the alloy disorder and the interface roughness, which reduces $\mu_S$ further. In contrast, an increase in $x$ reduces the penetration of the electron wave function into the $Al_xGa_{1-x}N$ layer by increasing the barrier height at the $GaN/Al_xGa_{1-x}N$ interface and thus increases $\mu_S$. *Id est*, the influence of alloy disorder scattering on $\mu_S$ is ambiguous [70].

11

A limitation of $\mu_S$ for $T < 100\,\mathrm{K}$ by strong temperature-dependent ionized impurity scattering is not observed as this scattering mechanism is screened for $n_S > 2 \cdot 10^{12}\,\mathrm{cm}^{-2}$ [70, 73, 75].

This behavior is also illustrated by Figure 2.5: The initial increase in $\mu_S$ is due to the improved screening of ionized impurities [70] while for $n_S > 2 \cdot 10^{12}\,\mathrm{cm}^{-2}$ $\mu_S$ starts to decrease again due to the increasing influence of interface roughness scattering and alloy disorder scattering.
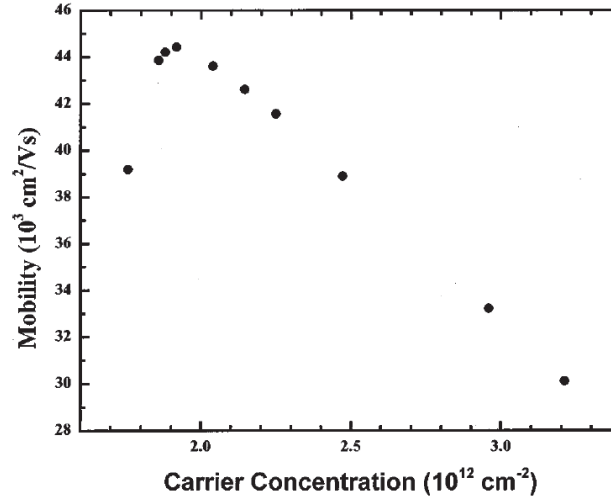


*Figure* 2.5 *Electron mobility in AlGaN/GaN heterostructures as a function of $n_S$ at $T = 0\,K$. Reprinted with permission from [75]. Copyright 2000, AIP Publishing LLC.*

Another way to increase $n_S$ in $\mathrm{GaN/Al}_x\mathrm{Ga}_{1-x}\mathrm{N/GaN}$ heterostructures is illumination. The electrons contributing to the increase in $n_S$ are attributed to the photoionization of deep level defects within the $\mathrm{Al}_x\mathrm{Ga}_{1-x}\mathrm{N}$ layer [76, 77] which are already ionized for photon energies smaller than the direct band gap $E_{\mathrm{gap}}$ of GaN [76, 78], *id est* photon energies smaller than $3.42\,\mathrm{eV}$ at $300\,\mathrm{K}$ [64]. Associated with the increase in $n_S$ is an increase in the conductivity which is equal to $e\,n_S\,\mu_S$ [63]. Hence, the decay times $\tau$ of the photo-induced increase in $n_S$ can be measured in terms of the photocurrent. As the photo-generated electrons are confined at the GaN-side of the interface and thus spatially separated from the ionized defects, following the electric field in the $\mathrm{Al}_x\mathrm{Ga}_{1-x}\mathrm{N}$ layer (cf. Figure 2.3), the decay time $\tau$ of the photocurrent is in the order of hours at $T = 300\,\mathrm{K}$ ($10^3\,\mathrm{s}$ [76] to $10^4\,\mathrm{s}$ [78]) and in the order of days at $T = 12\,\mathrm{K}$ ($10^6\,\mathrm{s}$ [79]). Thus, this effect is termed persistent photocurrent.

Besides exhibiting large sheet carrier concentrations and high electron mobili-

ties $GaN/Al_xGa_{1-x}N/GaN$ heterostructures show a pH-sensitivity of $(53\text{-}56)\,mV\,pH^{-1}$ [2, 80], close to the Nernstian limit of $59.16$ $mV\,pH^{-1}$. The pH-sensitivity of $GaN/Al_xGa_{1-x}N/GaN$ heterostructures is due to hydroxyl groups which are introduced at the GaN surface by oxidation [2, 80, 81] and can be described by the site-binding model by Yates *et al.* [82].

The hydroxyl groups OH are amphoteric and can protonate ($OH_2^+$) or deprotonate ($O^-$) in dependence of the proton concentration at the surface of the $GaN/Al_xGa_{1-x}N/GaN$ heterostructure [H] according to the dissociation-association processes in Eq. 2.4 and Eq. 2.5.

$$OH_2^+ \rightleftharpoons OH + H^+ \tag{2.4}$$

$$OH \rightleftharpoons O^- + H^+ \tag{2.5}$$

The dissociation constants $K_+$, resulting from Eq. 2.4, and $K_-$, resulting from Eq. 2.5, are given in Eq. 2.6 and Eq. 2.7.

$$K_+ = \frac{[OH]\,[H^+]}{[OH_2^+]} \tag{2.6}$$

$$K_+ = \frac{[O^-]\,[H^+]}{[OH]} \tag{2.7}$$

Thereby, $[OH_2^+]$, $[O^-]$ and $[OH]$ represent the density of protonated, deprotonated and neutral hydroxyl groups at the surface of the heterostructure in equilibrium .

Under the assumption that only protons binding to the surface via hydroxyl groups contribute to the pH-sensitivity, the pH-dependent surface charge $\sigma_{OH}$ as well as the total density of available surface sites $n_{total}$ can be defined by Eq. 2.8 and Eq. 2.9, respectively.

$$\sigma_{OH} = e([OH_2^+] - [O^-]) \tag{2.8}$$

$$n_{total} = [OH_2^+] + [O^-] + [OH] \tag{2.9}$$

For correlation of [H] with the concentration of protons in the bulk electrolyte, $[H]^E$, the Boltzmann statistics is applied:

$$[H] = [H]^E \exp\left(-\frac{e\phi_S}{kT}\right) \tag{2.10}$$

Taking into account Eq. 2.6 to Eq. 2.10, it is possible to relate the mean electrostatic potential at the surface plane of charged sites relative to the bulk electrolyte, $\phi_S$, to the pH of the bulk electrolyte, $pH^E = -lg([H]^E)$, as well as the ratios of $[OH_2^+]/n_{total}$ and $[O^-]/n_{total}$.

$$
\begin{aligned}
\ln\left([H]^E\right) &= -2.303 pH^E \\
&= \frac{e\phi_S}{kT} + \ln(\sqrt{K_+K_-}) + \ln\left(\frac{[O^-]}{n_{total}}\right) - \ln\left(\frac{[OH_2^+]}{n_{total}}\right)
\end{aligned} \tag{2.11}
$$

At the point of zero charge $[OH_2^+] = [O^-]$ and $\phi_S = 0$. Hence, the pH at the point of zero charge, $pH_{pzc}$, is defined by Eq. 2.12

$$
pH_{pzc} = -lg(\sqrt{K_+K_-}) \tag{2.12}
$$

Under the assumption that $[OH_2^+]/n_{total} \approx [O^-]/n_{total} \ll 1$, *id est* the density of charged surface sites is considerably smaller than the total density of surface sites, Eq. 2.13 reduces to

$$
\ln\left([H]^E\right) = \frac{e\phi_S}{kT} + \ln(\sqrt{K_+K_-}) \tag{2.13}
$$

which is synonymous to Eq. 2.14 at $T = 298\,K$ yielding a Nernstian pH-sensitivity of $59.16\ mV\,pH^{-1}$.

$$
\begin{aligned}
\Delta pH &= pH^E - pH_{pzc} \\
&= -\frac{e\phi_S}{2.303kT} \\
&= -\frac{1}{59.16mV} \cdot \phi_S
\end{aligned} \tag{2.14}
$$

Considering Eq. 2.8 the site-binding model allows as well the calculation of $\sigma_{OH}$ in dependence of pH. To illustrate the effect of $\sigma_{OH}$ on the band profile of a $GaN/Al_xGa_{1-x}N/GaN$ heterostructure with layer thicknesses of $1\,nm$, $18\,nm$ and $800\,nm$, respectively, and an aluminum content of 27%, as used in this work, calculations in next**nano**[3] (next**nano**, Garching, Germany) were carried out. The results of this calculations were used to produce Figure 2.6 which reflects the trends obtain by the calculation in next**nano**[3] but not the absolute values. This alteration of the calculation results is necessary to display the effect of $\sigma_{OH}$ and thus pH on the conduction band in the region of

the 2DEG properly.

At a pH of 6.8 the point of zero charge at the GaN surface is reached [83]. Hence, the band profile depicted in Figure 2.6b) is solely governed by the polarization of the heterostructure as discussed above.
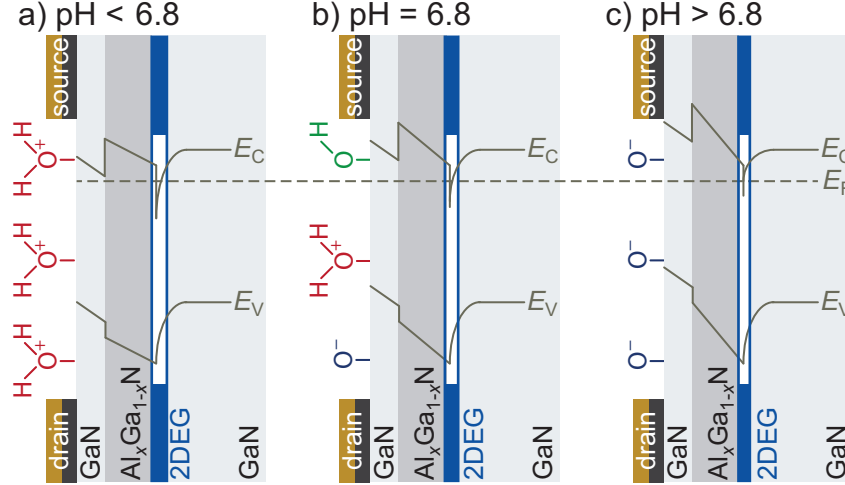


Figure 2.6 *Schematic representation of the band profile in a Ga-face GaN/AlGaN/GaN FET in dependence of pH as calculated by* next**nano**$^3$.
*a) pH < 6.8: $\sigma_{OH} > 0$, mainly protonated hydroxyl groups present on the gate surface result in an increase of the 2DEG sheet carrier concentration.*
*b) pH = 6.8: point of zero charge [83], $\sigma_{OH} = 0$, deprotonated and protonated hydroxyl groups on the gate surface cancel each other, id est the 2DEG sheet carrier density is solely due to the polarization of the heterostructure.*
*c) pH > 6.8: $\sigma_{OH} < 0$, mainly deprotonated hydroxyl groups present on the gate surface result in a decrease of the 2DEG sheet carrier concentration.*

At acidic pH < 6.8, $\sigma_{\mathrm{OH}}$ is positive diminishing the negative, polarization induced sheet charge density located towards the surface of Ga-face GaN/Al$_x$Ga$_{1-x}$N/GaN heterostructures (cf. Figure 2.6a)). Hence, the electric field within the Al$_x$Ga$_{1-x}$N layer is decreased. As a result the inclination of the band profile is less pronounced and a further dip of the triangular quantum well at the Al$_x$Ga$_{1-x}$N/GaN interface beneath $E_{\mathrm{F}}$ is observed as shown in Figure 2.6a). Thus, the 2DEG sheet carrier concentration $n_{\mathrm{S}}$ is increased yielding a higher conductivity between the ohmic drain and source contacts. For basic pH > 6.8, $\sigma_{\mathrm{OH}}$ is negative having the opposite effect as shown in

Figure 2.6c): The electric field in the $Al_xGa_{1-x}N$ layer is increased and the quantum well dips less below $E_F$, decreasing $n_S$.

Besides being responsible for the pH-sensitivity of $GaN/Al_xGa_{1-x}N/GaN$ heterostructures, the hydroxyl groups on the GaN surface of the $GaN/Al_xGa_{1-x}N/GaN$ heterostructure are the basis for the long-term stable covalent immobilization of receptors such as enzymes [2, 84, 85] and peptides [86] which define the specificity of the respective biosensor fabricated from the heterostructure.

In summary, $GaN/Al_xGa_{1-x}N/GaN$ heterostructures exhibit outstanding electric properties and an almost Nernstian pH-sensitivity. In combination with available functionalization techniques, as well as their biocompatibility [43, 44, 45, 46] and high chemical stability [47, 48], these properties make SGFETs fabricated from $GaN/Al_xGa_{1-x}N/GaN$ heterostructures highly suitable for the application as transducers in biosensors [43].

## 2.2 Kinetic Model for pH-Sensitive Enzyme-Modified Field-Effect Transistors

The possibility to model the response curves of EnFETs is essential for quantitative analysis of the EnFET response characteristics and of the covalently immobilized enzyme layer, which opens the route for understanding and optimization of such devices. One model suitable for the analysis of pH-sensitive SGFETs with a (sub-)monolayer of covalently immobilized pH-affecting enzymes is the kinetic model introduced by Glab *et al.* in 1991 [49]. This model is based on a model for enzyme electrodes by Morf [87]. The main assumption of Morf's model is that the transport rates are proportional to the concentration of a species inside and outside of the enzyme layer which is in contrast to diffusion models suitable for sensors with thick enzyme layers where the transport rate is proportional to the concentration gradient over the enzyme layer. This assumption does not only make the model by Glab *et al.* applicable to SGFETs with thin enzyme layers but also allows to disregard the geometry of the enzyme layer, *id est* the density of enzymes within. Thus, the calculation of the concentration profiles of, *exempli gratia*, substrate and product of the

enzymatic reaction within the enzyme layer, which involves difficult solving of hyperbolic functions in case of diffusion models [56, 57, 58, 59], can be omitted. Furthermore, the kinetic model by Glab *et al.* allows differences between the transport rate constants of all involved species and can account for stirring effects by modifying those constants.

The foundation of the kinetic model by Glab *et al.* is the Michaelis-Menten kinetics [88, 89] which is used to describe the reaction rate $v$ of a pH-affecting enzyme. This enzymatic reaction is schematically expressed in Eq. 2.15 for an enzyme (E) which converts a substrate (S) into acid (HA), base (B) and a non-protolytic product (N) with rate constant $k_2$ after the reversible formation of the enzyme-substrate complex (ES) with the rate constants $k_1$ and $k_{-1}$. The stoichiometric coefficients are denoted $n_A$, $n_B$ and $n_N$, respectively.

$$E + S \underset{k_{-1}}{\overset{k_1}{\rightleftharpoons}} ES \xrightarrow{k_2} E + n_A HA + n_B B + n_N N \qquad (2.15)$$
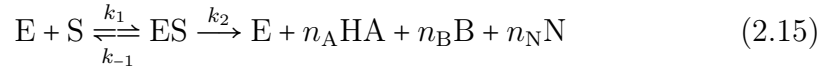
In case of the two enzymes discussed in the context of this work, penicillinase and AChE, the stoichiometric coefficients are $n_A = 1$, $n_B = n_N = 0$ and $n_A = n_N = 1, n_B = 0$, respectively, as can be seen from Figure 2.7. Hence, both
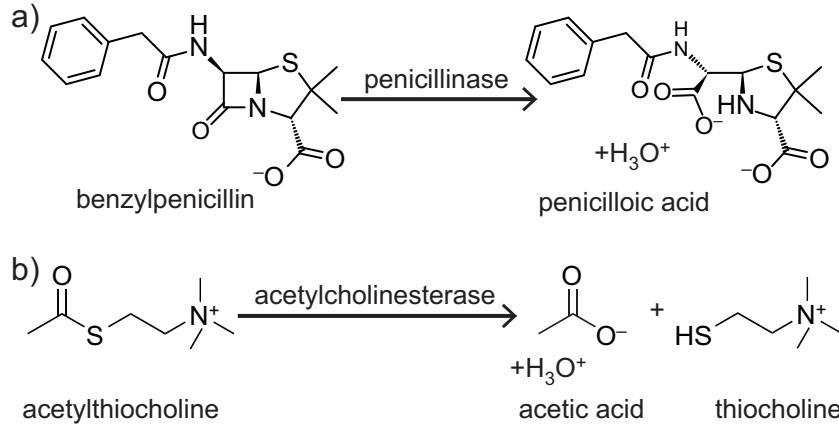


*Figure* 2.7 *Enzymatic reaction of a) penicillinase and b) acetylcholinesterase.*

enzymatic reactions lead to a decrease of pH due to the dissociation of the acidic product which can be monitored by a change in the gate-source potential $\Delta U_{GS}$ of a pH-sensitive SGFET.

Besides the enzymatic conversion of substrate into products, the transport into and out of the enzyme layer of all species that contribute to the EnFET signal and the acid dissociation constants $K_{ai}$ of all pH-affecting species have to be considered. As it is depicted in Figure 2.8 for the case of an acid-producing

enzyme covalently immobilized on the gate area of an EnFET, this means that the transport of substrate (S), product (HP), deprotonated product (P), buffer (HBF), deprotonated buffer (BF) and protons (H) with the respective transport rate constant $k_i$ has to be taken into account.
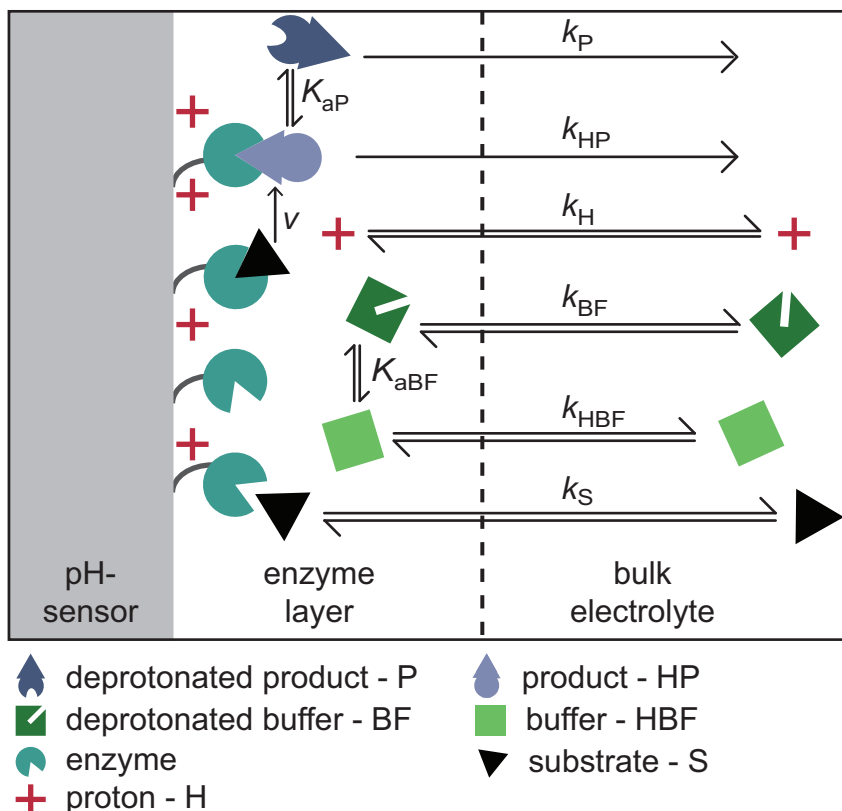


*Figure* 2.8 *Schematic representation of a pH-sensitive EnFET with the covalently immobilized enzyme producing an acid. The variables $k_i$ and $K_{ai}$, with corresponding subscripts, are transport rate constants and acid dissociation constants, respectively, for species indicated by the subscripts; $v$ is the reaction rate of the enzymatic reaction.*

Furthermore, the enzymatic reaction rate $v$ in dependence of the substrate concentration at the EnFET gate surface [S] as given by the Michaelis-Menten kinetics in the following equation has to be considered.

$$
\begin{aligned}
v &= v_{\max} \frac{[S]}{\frac{k_{-1}+k_2}{k_1} + [S]} \\
&= v_{\max} \frac{[S]}{K_M + [S]}
\end{aligned}
\tag{2.16}
$$

Here, the Michaelis constant $K_M$ is the substrate concentration at which $v$ is half of the maximum rate of the enzymatic reaction $v_{max}$. With those conditions, one can establish the following set of rate equations that couple the change in total concentration of each species in the enzyme layer:

$$\frac{d[S]}{dt} = k_S \cdot [S]^E - k_S \cdot [S] - v_{max} \frac{[S]}{K_M + [S]}$$

$$\frac{d([BF] + [HBF])}{dt} = k_{BF} \cdot [BF]^E + k_{HBF} \cdot [HBF]^E$$

$$- k_{BF} \cdot [BF] - k_{HBF} \cdot [HBF]$$

$$\frac{d([P] + [HP])}{dt} = v_{max} \frac{[S]}{K_M + [S]} - k_P \cdot [P] - k_{HP} \cdot [HP]$$

$$\frac{d([H] + [HP] + [HBF])}{dt} = v_{max} \frac{[S]}{K_M + [S]} + k_H \cdot [H]^E + k_{HBF} \cdot [HBF]^E$$

$$- k_{HP} \cdot [HP] - k_H \cdot [H] - k_{HBF} \cdot [HBF].$$

(2.17)

Here, $[i]$ represents the concentration of a species in the enzyme layer while $[i]^E$ indicates the concentration in the bulk electrolyte.

Under steady state conditions the concentration of all species inside the enzyme layer is constant. Hence, all the derivatives in Eq. 2.17 are equal to zero. With the thus obtained equations and the assumption that the transport rate constant of a species is independent of the protonation, *id est* $k_i = k_{Hi}$, the following rate equation can be derived.

$$\frac{k_H}{k_S} \left([H]^E - [H]\right) + \frac{k_{BF}}{k_S} [BF]^E \left(\frac{1}{1 + \frac{K_{aBF}}{[H]^E}} - \frac{1}{1 + \frac{K_{aBF}}{[H]}}\right)$$

$$+ \frac{1}{2} \left([S]^E + \frac{v_{max}}{k_S} + K_M - \sqrt{\left([S]^E - \frac{v_{max}}{k_S} - K_M\right)^2 + 4K_M [S]^E}\right) \frac{1}{1 + \frac{[H]}{K_{aP}}} = 0$$

(2.18)

Eq. 2.18 can be solved for the proton concentration on the surface of the EnFET gate area, $[H]$, as a function of the substrate concentration in the bulk electrolyte $[S]^E$. As changes in $[H]$ on the gate area are measured by the pH-sensitive SGFET in terms of $\Delta U_{GS}$, Eq. 2.18 allows a mathematical description of the EnFET response $\Delta U_{GS}$ as a function of $[S]^E$ depending on the model parameters $K_M$, $v_{max}$, $k_H$, $k_{BF}$ and $k_S$. To reduce the model parameters from five to four, normalized rate constants, $k_V = v_{max}/k_S$ in M (mol l$^{-1}$),

$\bar{k}_{\mathrm{H}} = k_{\mathrm{H}}/k_{\mathrm{S}}$ and $\bar{k}_{\mathrm{BF}} = k_{\mathrm{BF}}/k_{\mathrm{S}}$, both dimensionless quantities, are introduced. Those four model parameters, $K_{\mathrm{M}}$, $k_{\mathrm{V}}$, $\bar{k}_{\mathrm{H}}$ and $\bar{k}_{\mathrm{BF}}$, can be extracted when the EnFET response characteristics $\Delta U_{\mathrm{GS}}([\mathrm{S}]^{\mathrm{E}})$ are fitted using the kinetic model [90]. Except for $K_{\mathrm{M}}$, which is purely determined by the interaction of enzyme and substrate, all parameters depend on at least one transport rate constant and thus are sensitive to variations in the respective permeability of the enzyme layer. Hence, $k_{\mathrm{V}}$, $\bar{k}_{\mathrm{H}}$ and $\bar{k}_{\mathrm{BF}}$ represent the SGFET/enzyme/electrolyte system. The parameter $k_{\mathrm{V}}$ is as well proportional to $v_{\max} = k_2 \cdot [\mathrm{E}]_0$ [88, 89] and thus a measure for the density of enzymes on the gate area, $[\mathrm{E}]_0$.

To illustrate the dependence of the EnFET response curves on each of the four model parameters, different sets of simulations are shown in Figure 2.9. In those simulation, one of the model parameters is varied while the others are set to $k_{\mathrm{V}} = 0.5\,\mathrm{mM}$, $K_{\mathrm{M}} = 100\,\mu\mathrm{M}$, $\bar{k}_{\mathrm{H}} = 100$ and $\bar{k}_{\mathrm{BF}} = 2$, respectively.

In all simulations shown in Figure 2.9 one can distinguish three different regions depending on the substrate concentration $[\mathrm{S}]^{\mathrm{E}}$:

## $[\mathrm{S}]^{\mathrm{E}} \lesssim 1000\,\mu\mathrm{M}$

- $\Delta U_{\mathrm{GS}}$ changes almost linearly with $[\mathrm{S}]^{\mathrm{E}}$, *id est* $v$ increases with each addition of substrate. This region is called the *sensitive region* in which the quantitative determination of administered substrate concentration is possible.

## $[\mathrm{S}]^{\mathrm{E}} \gtrsim 1000\,\mu\mathrm{M}$

- $\Delta U_{\mathrm{GS}}$ is almost independent of $[\mathrm{S}]^{\mathrm{E}}$ and $v_{\max}$ is reached, *id est* all enzymes are permanently occupied. This region is called the *saturation region*.

## $[\mathrm{S}]^{\mathrm{E}} \approx 1000\,\mu\mathrm{M}$

- Transition region between the sensitive region and the saturation region.

Figure 2.9a) shows the variation of the model parameter $k_{\mathrm{V}}$ over two orders of magnitude from $1\,\mathrm{mM}$ to $0.01\,\mathrm{mM}$. First, the decrease in $k_{\mathrm{V}}$ mainly affects the saturation region of the EnFET response curve while the signal vanishes completely when $k_{\mathrm{V}}$ is reduced to $0.01\,\mathrm{mM}$. As $k_{\mathrm{V}} = k_2 \cdot [\mathrm{E}]_0/k_{\mathrm{S}}$ this means that with constant enzyme activity ($k_2 \approx \mathrm{const}$) a decrease in $k_{\mathrm{V}}$ reflects an increase in $k_{\mathrm{S}}$, *id est* higher permeability of the enzyme layer for substrate molecules, and/or a decrease in $[\mathrm{E}]_0$, *id est* a loss of active enzyme from the SGFET

surface. Hence, if $[E]_0$ is too low and/or the permeability for the substrate is too high, no signal can be recorded with an EnFET.
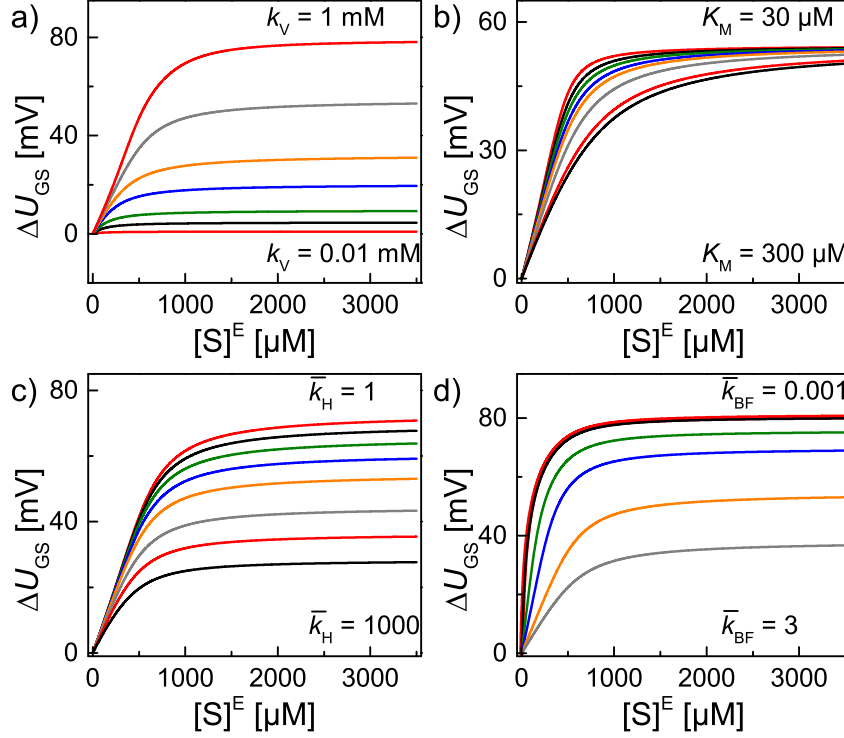


*Figure* 2.9 *Simulated EnFET response curves after the model of Glab et al. [49, 90]. Varied parameters: a) $k_V$, b) $K_M$, c) $\bar{k}_H$, d) $\bar{k}_{BF}$, while all other parameters have been fixed to $k_V = 0.5$ mM, $K_M = 100\,\mu$M, $\bar{k}_H = 100$ and $\bar{k}_{BF} = 2$. Variation of the individual parameters: a) $k_V[mM] = 1, 0.5, 0.3, 0.2, 0.1, 0.05, 0.01$; b) $K_M[\mu M] = 300, 200, 150, 100, 80, 60, 45, 30$; c) $\bar{k}_H = 1000, 500, 250, 100, 50, 25, 10, 1$; d) $\bar{k}_{BF} = 3, 2, 1, 0.5, 0.05, 0.001$.*

From Figure 2.9b) it is evident that the effect of the variation of the Michaelis constant $K_M$ on the response curves is most pronounced in the transition region. The increase in $K_M$ from $30\,\mu$M to $300\,\mu$M leads to a flattening of the EnFET response curve in the transition region. As $K_M$ is defined by the ratio of the reaction constants of the dissociation and formation of the enzyme-substrate complex (cf. Eq. 2.16), $K_M$ is an inverse measure for the substrate's affinity to the enzyme [88, 89]. Hence, an increase in $K_M$, representing a decreased substrate affinity, can indicate a denaturation process of the covalently immobilized enzyme layer.

An increase in $\bar{k}_H$ by three orders of magnitude from 1 to 1000 mainly affects

the saturation region as displayed in Figure 2.9c). With $\bar{k}_\mathrm{H}$ being defined by the ratio of $k_\mathrm{H}$ to $k_\mathrm{S}$ this increase in $\bar{k}_\mathrm{H}$ reflects an increasing permeability of the enzyme layer for protons in comparison to substrate molecules. As a consequence, the height of the saturation signal, which is correlated to the highest proton concentration measurable in terms of $\Delta U_\mathrm{GS}$ at the gate, is diminished when $\bar{k}_\mathrm{H}$ is increased.

Finally, the influence of the variation of $\bar{k}_\mathrm{BF}$ on the EnFET response curves was evaluated. As shown in Figure 2.9d) the increase in $\bar{k}_\mathrm{BF}$ affects the EnFET response curves as a whole: the slope in the sensitive region as well as the height of the saturation region are reduced. However, it should be noted that $\bar{k}_\mathrm{BF}$ has to increase from 0.01 to 0.05 before any change in the EnFET response curve is clearly evident. The amount of buffer present in the enzyme layer directly influences the proton concentration achievable by the enzymatic reaction in the enzyme layer, as a buffer is used to attenuate changes in the proton concentration. Hence, as long as buffer molecules are transported into and out of the enzyme layer at a smaller rate than the substrate molecules ($\bar{k}_\mathrm{BF} \ll 1$) the buffer's effect on the EnFET response is negligible. But as $\bar{k}_\mathrm{BF}$ reaches or exceeds unity the influence of the buffer on the EnFET response curves becomes more pronounced. Thereby, the whole response is diminished. Nevertheless, it should be noted that the change of only one model parameter is an unlikely event when analyzing EnFET response curves under varying experimental conditions. In those cases, the development of the model parameters in dependence of each other and their consistent interpretation is important to allow understanding of the EnFET system.

## 2.3 Concept of a Neuron/AcFET Hybrid

The *in situ* detection of the neurotransmitter ACh on a (sub-)second timescale [34] is one advantage of AChE-based potentiometric biosensors compared to current standard methods such as liquid chromatography combined with the electrochemical detection of hydrogen peroxide [31], matrix-assisted laser desorption ionization time-of-flight mass spectrometry [32] and liquid chromatography in combination with electrospray ionization mass spectrometry [33]. Although those methods exhibit a high sensitivity in the (sub-)nM-range which is superior to the ACh detection limit of $1\,\mu\mathrm{M}$ of AChE-based potentiometric

biosensors [34, 39, 85], their *modus operandi* makes *in situ* application impossible. A further disadvantage of the aforementioned methods is the unavoidable destruction of the biological sample under investigation as part of the required sample preparation. In contrast, a biological sample, *exempli gratia* a tissue sample, placed on the gate area of an AChE-based potentiometric biosensor can be easily removed from the biosensor after the experiment, monitoring the release of ACh in response to a stimulus. This makes further investigations of the biological sample, such as testing for the sample's vitality, feasible.

One possible proof-of-principle experiment to show that AChE-based potentiometric biosensors can be used for *in situ* detection of ACh is the measurement of ACh released by stimulated neurons cultured on the gate area of those devices. Here, one can argue that the ACh detection limit of an AChE-based potentiometric biosensor of $1\,\mu M$ could be reached [34] as ACh concentrations in the sub-mM-range have been reported in the synaptic cleft [91] and the space between neurons and the gate is limited [42]. The function principle of such a so-called neuron/AcFET hybrid will be outlined in this section and analogies to a chemical synapse between two cholinergic neurons are drawn.

In general, a synapse is a contact point between two excitable cells at which information is transferred either chemically by a transmitter or electronically from the presynaptic cell to the postsynaptic cell [92]. In the case of two cholinergic neurons the classical transmitter is ACh. In the axon terminal of the presynaptic neuron ACh molecules are packed in vesicles which are either located in the reserve pool or the readily releasable pool. Vesicles belonging to the readily releasable pool are already docked to the presynaptic membrane at so-called active zones and have been primed. "Priming" in this context refers to the formation of the synaptosomal-associated protein receptor (SNARE) complex consisting of two proteins of the presynaptic membrane, syntaxin and synaptosomal-associated protein 25 (SNAP-25), and one protein of the vesicle membrane, synaptobrevin, which holds the vesicle in a "pre-fusion" state [92]. The arrival of an action potential and the associated depolarization of the presynaptic membrane opens voltage-gated calcium channels ($Ca_V$ channels). As a result $Ca^{2+}$-ions advect into the presynaptic neuron where they bind to the protein synaptotagmin located at the vesicle membrane. The interaction of $Ca^{2+}$ with synaptotagmin results in an immediate fusion of the presynaptic membrane with the vesicle and exocytosis of the neurotransmitter ACh [93].

In case of a synapse as depicted in Figure 2.10a) the transmitter diffuses

through the synaptic cleft and binds to nicotinic acetylcholine receptors (nAChR) which are ionotrop, *id est* ligand-gated, ion channels. When two ACh molecules have bound to the nAChR a confirmation change occurs, leading to the opening of the channel, allowing $Na^+$-ions and $Ca^{2+}$-ions to advect into the postsynaptic neuron following their electrochemical gradient [93]. This
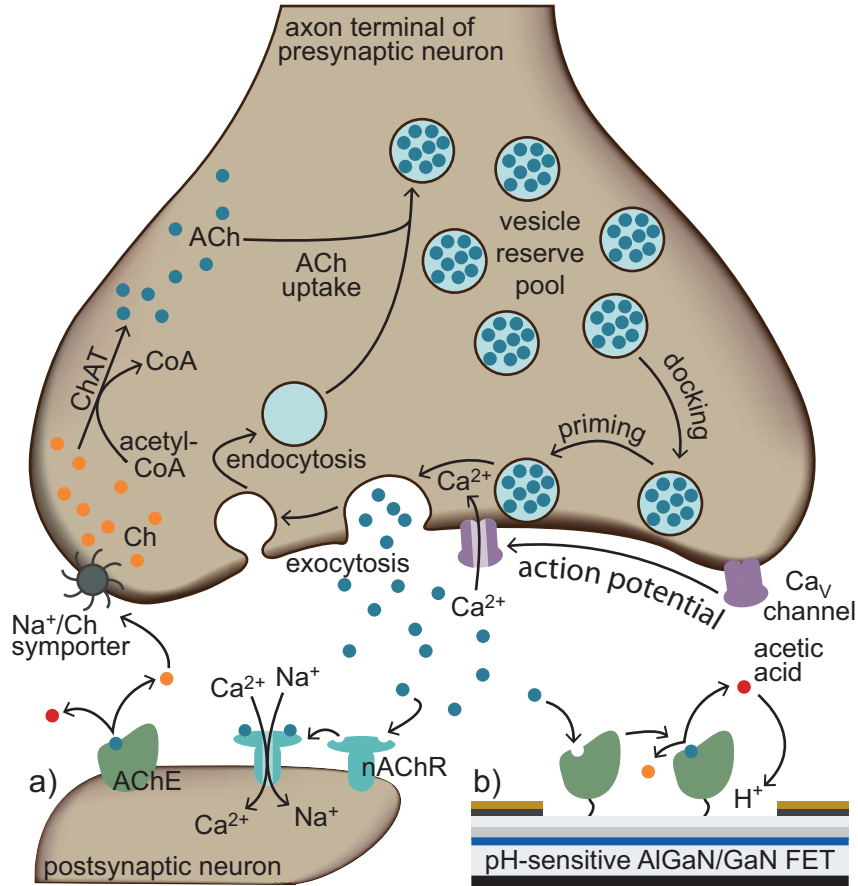


*Figure* 2.10 *Schematic representation of a) a synapse and b) an neuron/AcFET hybrid. ACh-packed vesicles are either located in the vesicle reserve pool or at active sites close to the presynaptic membrane. The arrival of an action potential opens $Ca_V$ channels and leads to an influx of $Ca^{2+}$-ions which trigger the release of ACh into the synaptic cleft. At the postsynaptic membrane ACh binds to ionotrop receptors resulting in a depolarization of the postsynaptic neuron (a)), while the enzymatic degradation of ACh by AChE bound to the gate area of a pH-sensitive AlGaN/GaN FET results in a lowered pH which can be measured by the FET (b)). The degradation product of the enzymatic reaction of AChE with ACh, Ch, is transported back into the presynaptic neuron for synthesis of ACh via the enzyme ChAT.*

influx of cations results in an excitatory postsynaptic potential, meaning a depolarization of the postsynaptic membrane which can evoke a new action potential, if a threshold value of the transmembrane potential of about $-50\,\text{mV}$ is exceeded [92]. To avoid desensitization of the nAChRs and prepare the synapse for a new incoming action potential, ACh is enzymatically split by AChE into acetic acid and choline (Ch) within the synaptic cleft.

In case of a neuron/AcFET hybrid depicted in Figure 2.10b) the postsynaptic neuron is replaced by an AChE-based potentiometric biosensor, here a pH-sensitive AlGaN/GaN FET with the enzyme AChE covalently immobilized on its gate surface. When the transmitter ACh, released by the presynaptic neuron, reaches the gate area and thus the AChEs bound to the gate surface, ACh is enzymatically degraded into acetic acid and Ch. The dissociation of acetic acid leads to a decrease of pH in the vicinity of the gate which can be measured by the AlGaN/GaN FET in terms of an increase in the drain-source current (cf. section 2.1) as soon as the detection limit is surpassed.

The degradation product of the enzymatic reaction of AChE with ACh, Ch, which is accumulated in case of a synapse as well as in case of a neuron/transistor hybrid, is transported back into the presynaptic neuron by Na$^+$/Ch symporters [94] for a *de novo*-synthesis of ACh, accomplished by the enzyme ChAT using Ch and acetyl coenzyme A (acetyl-CoA) [95]. Then, ACh is transferred into vesicles obtained by endocytosis from the presynaptic membrane via secondary active transport, *id est* the ACh transport is driven by a proton concentration gradient generated by an adenosine triphosphate consuming proton pump which acidifies the vesicles' interior [96]. Thus, the vesicle cycle is completed.

# 3 Methods

In this chapter the fundamental techniques utilized to obtain the results are illustrated. Additionally, it discusses properties of the AlGaN/GaN SGFETs as prepared by the procedure described in section 3.1 and the success of the silanization with (3-aminopropyl)triethoxysilane (APTES) (cf. subsection A) by means of X-ray photoelectron spectroscopy (XPS). Further, section 3.2 covers the immobilization routine for the enzymes penicillinase and AChE. In the third section, the preparation of myenteric neurons from the myenteric plexus still embedded in the *muscularis propria* and coeliac ganglia from adult Wistar rats, as well as isolated myenteric neurons from (4 - 12) days old Wistar rats, for experiments monitoring neuronal activity with an AcFET, is explained. The subsequent section describes the experimental procedure and the evaluation of the resulting data.

The chapter is completed by a description of immunocytochemistry and fluorometric calcium imaging, utilized to assess the vitality of isolated myenteric neurons and tissue samples of the *muscularis propria*, respectively.

## 3.1 Preparation of AlGaN/GaN Solution-Gated Field-Effect Transistors

In the course of this work pH-sensitive SGFETs prepared from a $GaN/Al_{0.27}Ga_{0.73}N/GaN$ (800 nm/18 nm/1 nm) high electron mobility transistor structure, schematically shown in Figure 3.1, were used. The $GaN/Al_{0.27}Ga_{0.73}N/GaN$ heterostructure was grown by metal organic chemical vapor deposition on silicon (111) substrates and a 1800 nm GaN buffer (DOWA, Tokyo, Japan).

For the preparation of 15 transistors a (12 mm × 14 mm) piece of the heterostructure was used which is represented by a single transistor in Figure 3.2.

First, the sample was washed for 1 min each in acetone (≥99.5%; Carl Roth, Karlsruhe, Germany) and isopropyl alcohol (≥99.5%; Carl Roth, Karlsruhe, Germany) in the ultrasonic bath DK152 (Bandelin, Berlin, Germany) at 820 W. Subsequently, the clean sample (cf. Figure 3.2A) was dried at 180 °C on a hotplate for at least 5 min before deposition of a 100 µl drop of positive photoresist ma-P1215 (micro resist technology, Berlin, Germany) at 3000 rpm for 60 s with spin coater Delta 6RC (SÜSS MicroTec, Garching, Germany). Afterwards, the
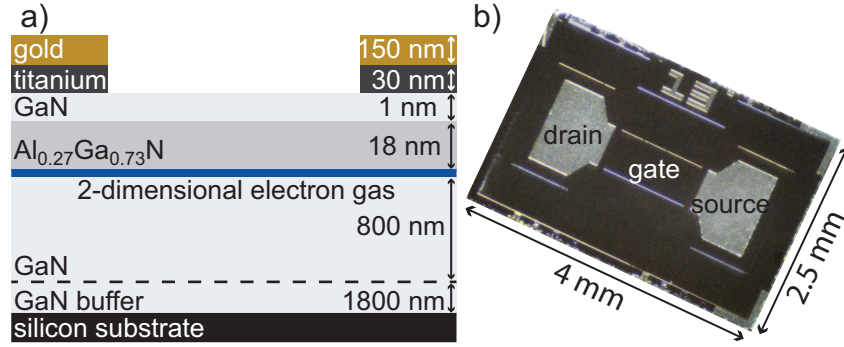


*Figure* 3.1 *a) Schematic side view and b) realistic top view of a processed AlGaN/GaN FET with dimensions.*

photoresist was baked out at 90 °C on a hotplate for 90 s. Then, 15 transistors with fixed gate length were patterned on the photoresist coated heterostructure using the customized photomask MS_20100921_020 set in a Karl Süss MA56 Mask Aligner Exposure System (SÜSS MicroTec, Garching, Germany) and an illumination time of 12 s. The photoresist was developed in ma-D331 (micro resist technology, Berlin, Germany) for 40 s followed by a bidestilled water stop bath for 30 s. The obtained structure in the photoresist defined the layout of the source and drain contacts of the FET and is schematically shown in Figure 3.2B.

Next, Ti/Au ohmic contacts for source and drain were deposited by thermal evaporation (E12E4; Edwards, Munich, Germany). Following this, the photoresist was removed in acetone and isopropyl alcohol and the heterostructure blow-dried with nitrogen. The structure (cf. Figure 3.2C) was then annealed for 30 s at 820 °C in vacuum ($p \leq 1 \cdot 10^{-5}$ mbar).

For patterning of the FET mesa-structure a second photolithography was carried out according to the procedure described above. Here, the etch mask defined the gate dimensions of (1.2 mm × 0.5 mm) and covered the Ti/Au contacts as shown in Figure 3.2D. The photoresist was cured in an oven (T5042E;

Heraeus, Hanau, Germany) for 3 h at 100 °C. Patterning of the FET mesa-structure was achieved by argon ion-beam etching using a ME 601 system (Veeco Instruments, Plainview, USA). After removing the photoresist in acetone and isopropyl alcohol, the samples was separated into 15 individual transistors with dimensions of (4 mm × 2.5 mm) by sawing, yielding a finished FET as schematically shown in Figure 3.2E.
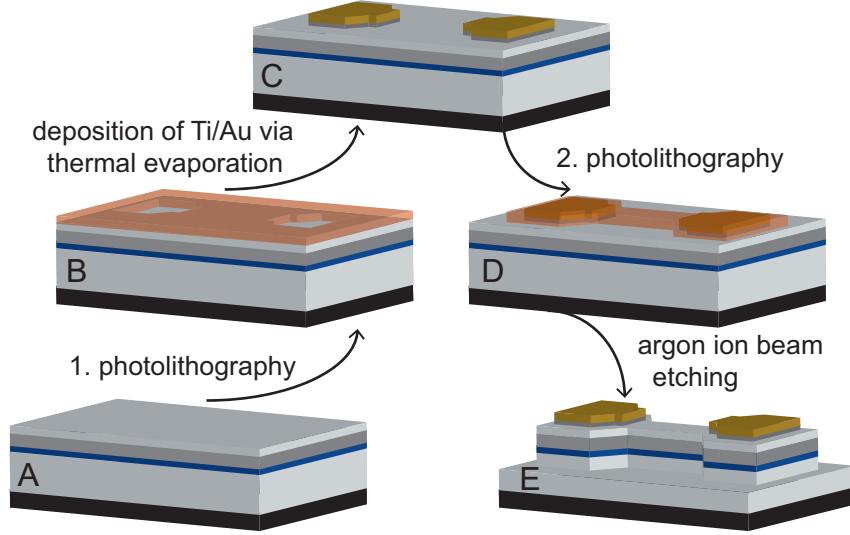


*Figure* 3.2 *Schematic representation of the manufacturing process of an Al-GaN/GaN FET. (A) Clean piece of heterostructure; (B) heterostructure covered with developed photoresist defining the layout of the source and drain contacts; (C) heterostructure with Ti/Au ohmic contacts for source and drain; (D) heterostructure covered with developed photoresist defining the FET mesa-structure; (E) finished FET.*

## Properties of Prepared AlGaN/GaN SGFETs

The sheet carrier density and the carrier mobility at room temperature were determined to $(2.0 \pm 0.2) \cdot 10^{13}\,\mathrm{cm^{-2}}$ and $(744 \pm 62)\,\mathrm{cm^2\,V^{-1}\,s^{-1}}$ from Hall-effect measurements.

The transistor characteristics and the pH-sensitivity of the prepared AlGaN/GaN SGFETs were determined using the measurement set-up discussed in section 3.4 in 0.5 mM phosphate buffered saline (PBS) solution (for preparation see appendix C.1).

The representative transfer characteristics and transconductance shown in Figure 3.3a) and b), respectively, illustrate the functionality of the AlGaN/GaN SGFETs. The AlGaN/GaN SGFETs are normally-on transistors with a threshold voltage of 2.8 V and the maximum of the transconductance at a gate-source potential $U_{GS}$ of $-1.65$ V as it is indicated by the dashed line in Figure 3.3.
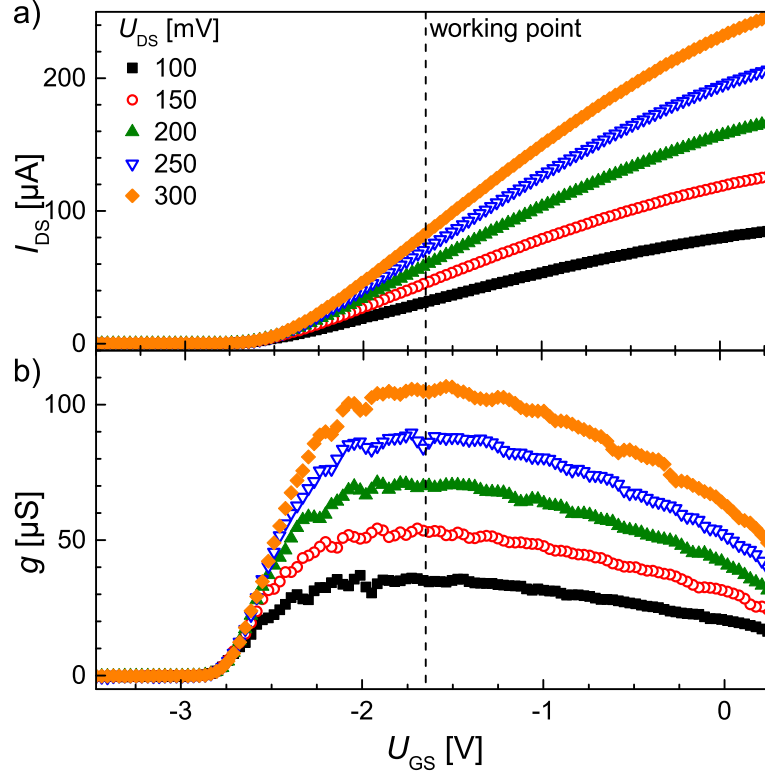


*Figure* 3.3 *a) Transfer characteristics and b) transconductance of a solution-gated AlGaN/GaN FET.*

The pH-sensitivity of AlGaN/GaN SGFETs correlates the change in the gate source potential $\Delta U_{GS}$, measured in current-clamping mode (cf. section 3.4), with the change in pH. In the representative case depicted in Figure 3.4, the pH-sensitivity was determined between pH 5 and pH 8 - the relevant pH-range for the here discussed experiments - after different steps of the functionalization process described in section 3.2. During those measurements, pH was adjusted by pipetting with a 10 mM hydrochloric acid solution (from 37% hydrochloric acid; Carl Roth, Karlsruhe, Germany) starting from pH 8. Linear fits of those measurements revealed an average pH-sensitivity of $(53.6 \pm 1.5)$ mV $\text{pH}^{-1}$ for all stages of the immobilization process. This is in reasonable agreement with earlier reports [43, 80].
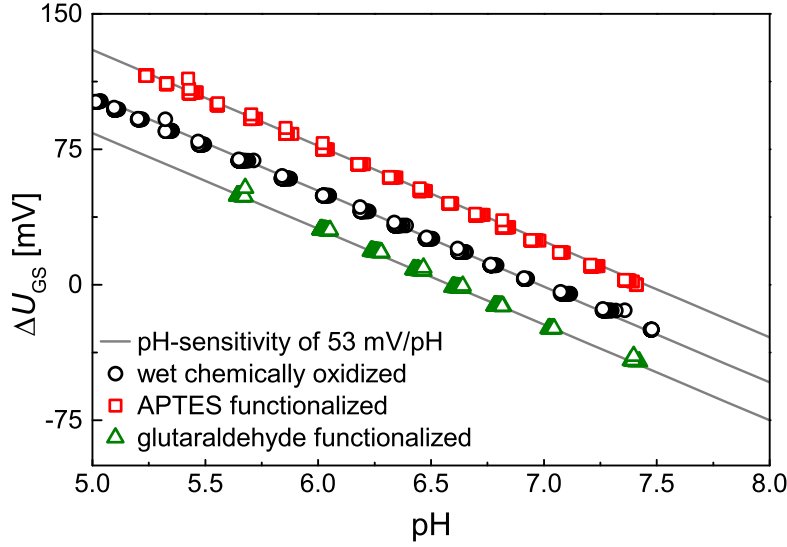
*Figure* 3.4 *Calibration curves for the pH-sensitivity of AlGaN/GaN FETs after different steps of the functionalization process. The slope of the solid lines represents a pH-sensitivity of $53\,mV\,pH^{-1}$.*

## 3.2 Functionalization

The functionalization of AlGaN/GaN SGFETs with APTES is the basis for the covalent immobilization of enzymes. Hence, the quality of the silanization with APTES is essential for the successful EnFET preparation. Due to this reason the success of the silanization routine is confirmed by XPS.

Furthermore, this section discusses the routine for covalent immobilization of the enzymes penicillinase and AChE on APTES-functionalized AlGaN/GaN SGFETs.

### 3.2.1 Silanization with APTES

The silanization routine of AlGaN/GaN SGFETs with APTES was developed following the procedure in reference [81] and is schematically depicted in Figure 3.5. First, the samples were cleaned with acetone and isopropyl in an ultrasonic bath (DK102; Bandelin, Berlin, Germany) at 384 W for 2 min each. Subsequently, the samples were oxidized for 20 min in a mixture of sulfuric acid (98%; Carl Roth, Karlsruhe, Germany) and hydrogen peroxide (≥30%; Fluka, Taufkirchen, Germany) in a ratio of 3:1. The oxidation was stopped

by rinsing the samples with bidestilled water (18 MΩ; Merck Millipore, Darmstadt, Germany). After blow-drying with nitrogen the samples were stored in a desiccator for a minimum of 2.5 h followed by silanization with APTES on the same day directly after the samples' removal from the desiccator.

For silanization the samples were put in a Teflon sieve and submerged in 20 mM APTES solution prepared in a reactor with 120 ml anhydrous toluene and 562 µl APTES ($C_9H_{23}NO_3Si$; ≥98%; Sigma-Aldrich, Taufkirchen, Germany). After the reactor had been sealed with a glass lid and Parafilm, it was placed in the ultrasonic bath DK102 for 90 min at 432 W at a temperature of 50 °C stabilized by a continuous-flow water heater/chiller. The reactor was then cooled down to approximately 20 °C over a time period of 60 min to stop the reaction.
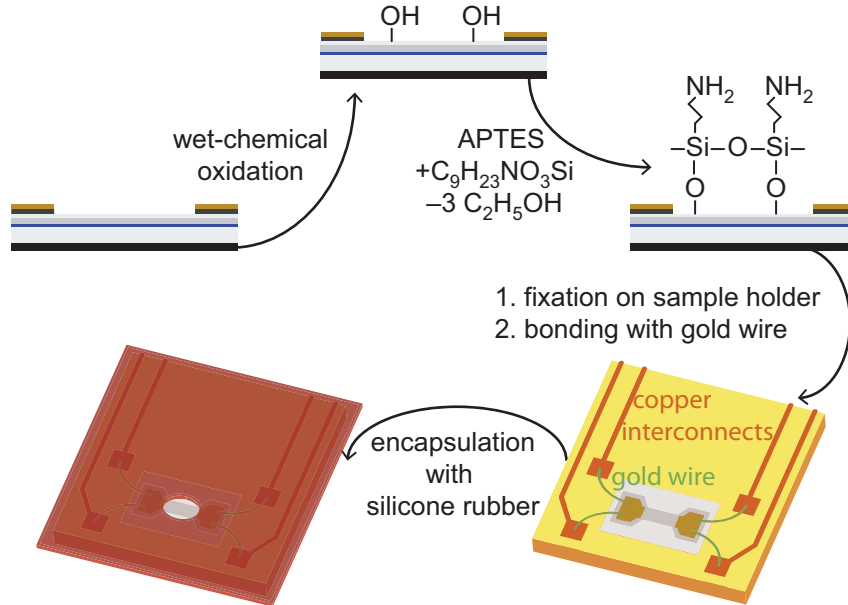


*Figure* 3.5 *Schematic representation of the functionalization with APTES and the encapsulation of an AlGaN/GaN SGFET.*

Next, the samples were cleaned in anhydrous toluene and isopropyl alcohol for 15 min each in the ultrasonic bath DK102 at 288 W and 384 W, respectively. A third cleaning step in diluted acetic acid (from 4% (v/v); Alfa Aesar, Karlsruhe, Germany) at pH 4 was conducted for 30 min in the ultrasonic bath DK102 at 48 W to ensure a (sub-)monolayer coverage with APTES of the AlGaN/GaN SGFETs. Finally, the samples were rinsed with bidestilled water, blow-dried with nitrogen and stored light-protected in a desiccator for at least 12 h.

After a maximum of 18 h each silanized AlGaN/GaN SGFET was mounted on a sample holder and electrically connected to the copper interconnects via bonding with gold wire (wire bonder 4124; Kullicke and Soffa, Horsham, Israel) as schematically shown in Figure 3.5. Subsequently, the contacts were checked by measuring the *UI* characteristics. Next, the samples were encapsulated with silicone rubber (Scrintec 901; Carl Roth, Karlsruhe, Germany) to passivate the electric contacts for measurements in aqueous electrolytes. The gate area remained uncovered as also shown in Figure 3.5. Afterwards, the samples were put in the refrigerator overnight at 5 °C to cure the silicone rubber.

## XPS Analysis

For analysis of the silanization by XPS Si-doped GaN layers grown on sapphire substrate were silanized with APTES according to the procedure described in this subsection. As the AlGaN/GaN heterostructure used for the production of SGFETs is capped with a GaN layer (cf. Figure 3.1) the APTES layer on GaN samples and AlGaN/GaN SGFETs should be comparable.

XPS analysis was carried out on a system from OMICRON electronics (Klaus, Austria) at the *Zentrum für Mikro- und Nanotechnologie* of the *Technische Universität Ilmenau*. The measurements were performed using Mg $K_\alpha$ radiation (h$\nu$ = 1253.6 eV) produced by a DAR 400 X-ray source from OMICRON and monochromated Al $K_\alpha$ radiation (h$\nu$ = 1486.7 eV) produced by a PHI 10-610 X-ray source in combination with an OMICRON XM1000 monochromator. All spectra were recorded in grazing emission ($\Theta$ = 53°) with an OMICRON 7 channel EA 125 hemispherical electron analyzer operating in constant pass energy mode with pass energies of 15 eV and 10 eV for the monochromated Al $K_\alpha$ radiation and the Mg $K_\alpha$ radiation, respectively. Calibration of the system was achieved by measuring the signal of the Ag3d$_{5/2}$ core level of clean polycrystalline silver. The energy resolution of the XPS measurements conducted with the monochromated Al $K_\alpha$ radiation and the Mg $K_\alpha$ radiation were 0.6 eV and 0.85 eV, respectively.

For analysis of the silanization with APTES, XPS spectra of Ga3s, Si2s, C1s, N1s, O1s and Ga2p$_{3/2}$ core levels from an oxidized GaN reference sample and an APTES-silanized GaN sample, which were freshly prepared for XPS measurements following the functionalization method outlined in subsection 3.2.1, were recorded. XPS spectra of the Ga3s, Si2s, C1s, O1s and Ga2p$_{3/2}$ core levels

were recorded with Al K$_\alpha$ radiation while the XPS spectrum of the N1s core level was recorded with Mg K$_\alpha$ radiation to avoid its superposition with the Ga L$_2$M$_{4.5}$M$_{4.5}$ Auger line [97]. All spectra were fitted using Voigt functions after background subtraction following the method by Shirley [98] and after accounting for charging effects by referencing all spectra to the peak position of the C–C bond in the C1s spectrum at 285.0 eV [99].

In Figure 3.6a) the XPS spectra of the Ga3s, Si2s, C1s, N1s, O1s and Ga2p$_{3/2}$ core levels of the oxidized sample shown in black and of the APTES-silanized sample shown in red are compared. The observed signals of the Ga3s, N1s and Ga2p$_{3/2}$ core levels are smaller for the silanized sample if compared to the oxidized sample while the signals of the C1s and O1s core levels are larger. The signal of the Si2s core level is only observable after silanization with APTES. These changes in the XPS spectra can be explained by the introduction of Si–O, C–Si, C–C, C–N and N–H bonds on the GaN surface due to the silanization with APTES (cf. Figure 3.5). Accordingly, the deconvoluted XPS spectra of the oxidized sample and of the silanized sample are shown in Figure 3.6b) and in Figure 3.6c), respectively.

The occurrence of the XPS spectrum of the Si2s core level due to silanization is a strong indication for the successful silanization with silicon-containing APTES. The peak position at 153.9 eV is attributed to the Si–O bond [100] in agreement with the introduction of Si–O bonds by silanization with APTES. The C1s spectrum of the oxidized sample was deconvoluted using two components at 285.0 eV (gray line) and 289.4 eV (green line) which are attributed to C–C and C=O bonds, respectively, and arise from surface contamination [101]. During silanization with APTES, C–N and C–Si bonds are introduced resulting in an asymmetry in the C1s spectrum. Thus, a third component at 286.3 eV (orange line) had to be used for the deconvolution which accounts for the APTES-related C–N and C–Si bonds [99]. Additional C–C bonds were also introduced by silanization, increasing the contribution of the C–C component to the C1s spectrum. Hence, the increase in the C1s signal is the sum of the signals arising from the introduction of C–Si, C–C and C–N bonds.

The O1s spectra of the oxidized and the silanized sample were deconvoluted using two components at 531.0 eV and 532.6 eV. The component at 531.0 eV (gray line) remains unchanged during silanization and is attributed to the O–Ga bond [102]. In case of the oxidized sample the component at 532.6 eV (green line) is attributed to hydroxyl groups introduced by the wet-chemical
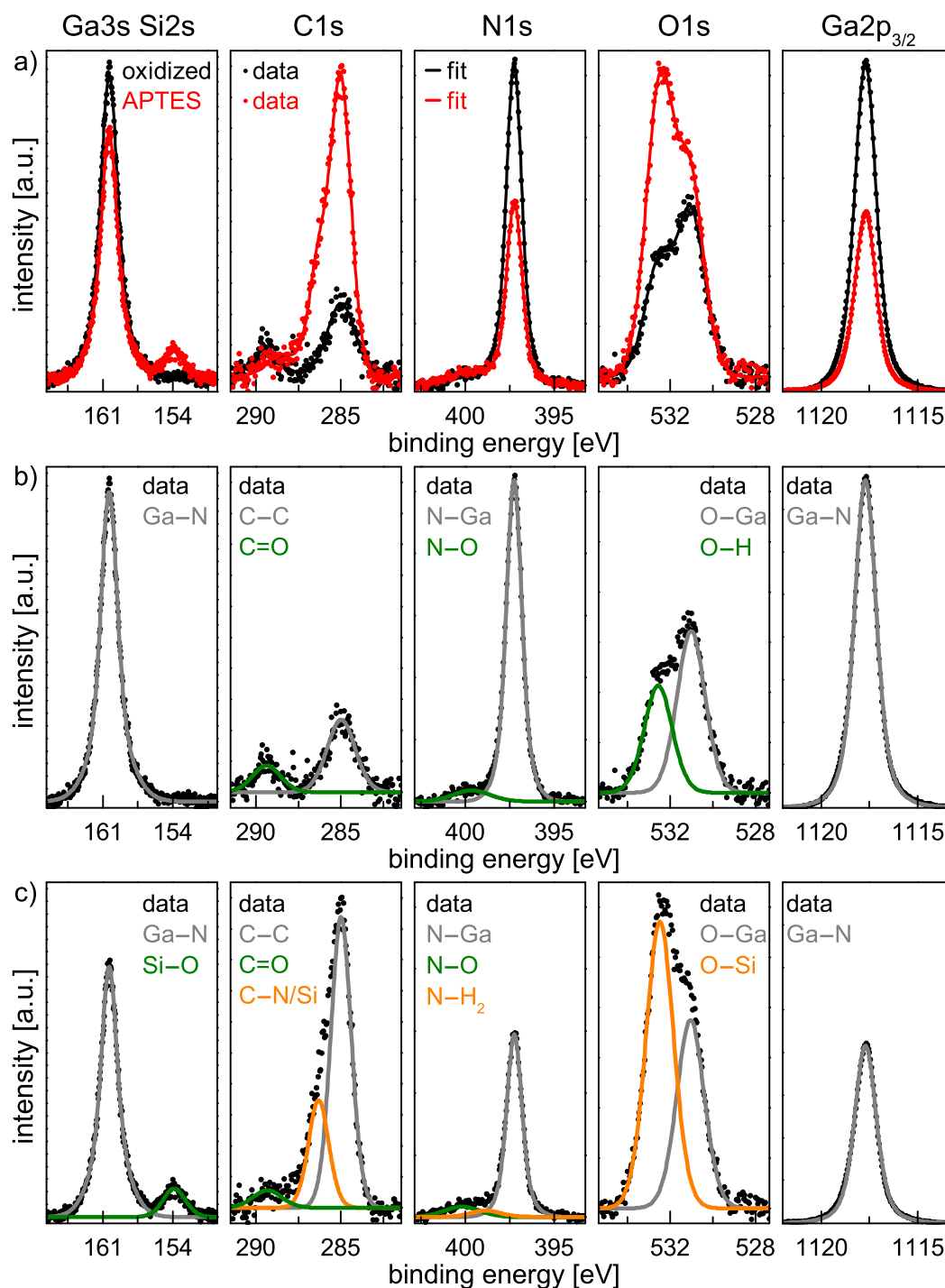
*Figure* 3.6 *XPS spectra of the Ga3s, Si2s, C1s, N1s, O1s and Ga2p$_{3/2}$ core levels. a) Comparison of the XPS spectra of an oxidized reference sample (black) and an APTES-silanized sample (red) showing the data as dots and the respective fits as lines. b) XPS spectra of the oxidized reference sample. c) XPS spectra of the APTES-silanized sample. In b) and c) dots represent the respective data as shown in a) while lines represent deconvolutions.*

oxidation [103]. As the silanization with APTES consumes hydroxyl groups (cf. Figure 3.5) the increase of this component with silanization cannot be explained by an increasing amount of hydroxyl groups but rather by the introduction of O–Si bonds which have the same binding energy [99]. Due to this concurrence a possible contribution of the hydroxyl groups to the O–Si component cannot be resolved.

The N1s spectrum of the oxidized sample was deconvoluted using two components at $397.3\,\mathrm{eV}$ (gray line) and $399.7\,\mathrm{eV}$ (green line) which are attributed to N–Ga bonds [97] and N–O bonds [99], respectively. Both components are also present in the silanized sample although the peak position of the N–O component is shifted to $400.2\,\mathrm{eV}$. This shift might be due to the introduction of protonated amino groups situated at $401.1\,\mathrm{eV}$ [104] which superimposes the N–O component. The attempts to resolve those two components contributing to the peak at $400.2\,\mathrm{eV}$ were not successful as fitting with two components always resulted in the area of one fit component approaching zero. A third component at $398.9\,\mathrm{eV}$ (orange line) used for deconvolution of the N1s spectrum of the silanized sample is attributed to neutral amino groups [104]. The attenuation of the N–Ga component with silanization is due to shielding of the GaN substrate by the covalently immobilized APTES layer. This effect is as well seen in case of the Ga3s spectrum and the Ga2p$_{3/2}$ spectrum. The decrease is less pronounced in case of the Ga3s signal as it has lower surface sensitivity than the Ga2p$_{3/2}$ signal due to a difference in the electron inelastic mean free path $\lambda$. According to the model by Tanuma *et al.* $\lambda$ of the Ga3s signal is $2.374\,\mathrm{nm}$ and $\lambda$ of the Ga2p$_{3/2}$ signal is $0.945\,\mathrm{nm}$ [105].

The Ga3s and the Ga2p$_{3/2}$ spectra were not deconvoluted with regard to the respective contributions of the Ga–O bond and the Ga–N bond as they represent the oxidized GaN substrate before and after silanization.

The XPS measurements allow an estimation of the surface coverage $\vartheta_{\mathrm{SC}}$ of the APTES layer by calculating the surface density of Si atoms with regard to the surface density of Ga atoms. The model used for this purpose was developed by Dr. Marcel Himmerlich *et al.* from the *Technische Universität Ilmenau* who also carried out the calculations.

The model describes the attenuation of the Ga signal from the GaN substrate as a result of its traversing through the oxide layer and the APTES layer taking into account the layer thicknesses $d_{\mathrm{oxide}}$ and $d_{\mathrm{APTES}}$ as well as $\lambda_{\mathrm{Ga}}$ of the GaN bulk material. The result of this calculation is a surface coverage $\vartheta_{\mathrm{SC}}$ of 0.5 to

0.6 Si atoms per Ga atom (Dr. Marcel Himmerlich, personal communication, March 3, 2016).

To estimate the surface coverage that corresponds to one monolayer, the area occupied by one APTES molecule and thus by one Si atom has to be assessed. Taking into account the length of the APTES molecule (8.5 Å [104]) and the Si–O bond length (1.623 Å [106]) while assuming that all O–Si–O bonds and the O–Si–C bond have bond angles of 109.5 ° - *id est* tetrahedral coordination of the Si atom - the occupied area per Si atom is $\approx 13.0$ Å$^2$. For a Ga atom this area is calculated to 8.807 Å$^2$ by utilizing the lattice parameter $a_0$ in Table 2.1. Hence, $\vartheta_{SC}$ is expected to be $\approx 0.68$ for a complete APTES monolayer. As the determined values for $\vartheta_{SC}$ have been 0.5 to 0.6, it follows that 73.5% to 88.2% of the GaN surface are covered with APTES.

In summary, the conducted XPS measurements show that the silanization with APTES was successful yielding a sub-monolayer with the silane layer covering up to 88.2% of the GaN surface.

## 3.2.2 Immobilization of Enzymes

For the preparation of enzyme-modified AlGaN/GaN SGFETs penicillinase (*bacillus cereus*, EC 3.5.2.6, P0389; Sigma-Aldrich, Taufkirchen, Germany) and AChE (*electrophorus electricus*, EC 3.1.1.7, C3389; Sigma-Aldrich, Taufkirchen, Germany) were covalently immobilized on the APTES-silanized gate area of the pH-sensitive AlGaN/GaN SGFETs adapting the procedures reported in references [2, 84] and [2, 85, 107], respectively.

As depicted in Figure 3.7 the silanized and encapsulated samples were initially treated in 20 mM aqueous glutaraldehyde solution prepared with 20 ml bidestilled water and 72.7 µl glutaraldehyde (50% in H$_2$O; Sigma-Aldrich, Taufkirchen, Germany) for 1 h at room temperature. Afterwards, the samples were rinsed with bidestilled water to remove unattached glutaraldehyde, which would agglomerate the enzymes, and gently dried under nitrogen flow.

Then, the glutaraldehyde-treated APTES layer was crosslinked with the respective enzyme by formation of a secondary amine via a Schiff base in the presence of cyanoborohydride. Simultaneously, the imine formed by the amino group of APTES and one of the aldehyde groups of glutaraldehyde in the first step of the enzyme immobilization was reduced to an amine. Thus, the "anchor" attaching the enzyme to the gate surface is carbon-nitrogen double bond

free (cf. Figure 3.7) which ensures its stability against hydrolytic degradation in aqueous environments [84].

In case of crosslinking penicillinase to the gate surface, a $100\,\mu l$ droplet of $800\,nM$ penicillinase solution was placed on the FET gate area and incubated for $1\,h$ at room temperature. In case of AChE the enzyme concentration was $400\,nM$ and the samples were incubated in a humid controlled environment at $5\,°C$ for $20\,h$.
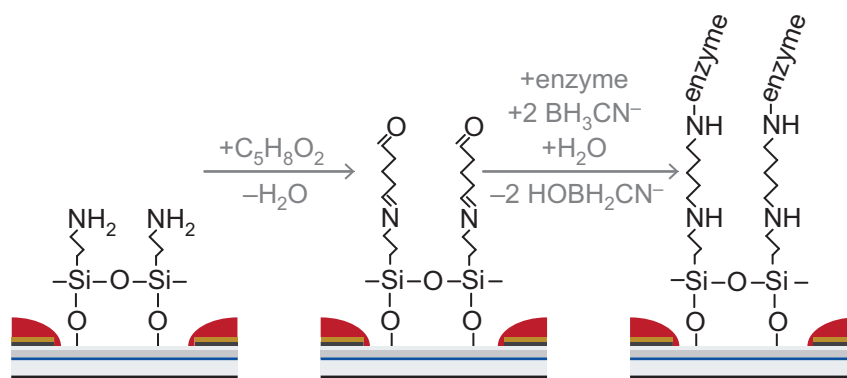


*Figure* 3.7 *Schematic representation of the procedure to covalently immobilize enzymes on encapsulated AlGaN/GaN FETs. The silicone encapsulation is depicted in red.*

The resulting EnFETs (schematically shown in the right illustration in Figure 3.7) were cleaned with $10\,mM$ PBS solution (for preparation see appendix C.1) in the ultrasonic bath DK102 at $192\,W$ for $10\,min$ with the continuous-flow water heater/chiller set to $5\,°C$. The pH of the $10\,mM$ PBS solution was adjusted to 7 for PenFETs and to 7.5 for AcFETs. The EnFETs were stored light-protected at $5\,°C$ in the respective $10\,mM$ PBS solution until they were used for experiments.

## 3.3 Preparation of Biological Samples

For experiments monitoring neuronal activity the myenteric plexus and coeliac ganglia from female and male Wistar rats with a body mass of $(140\text{-}160)\,g$ and $(160\text{-}200)\,g$, respectively, and isolated myenteric neurons from $(4\text{-}12)\,days$ old Wistar rats were used in the present work. The animals were bred and housed at the *Institut für Veterinär-Physiologie und -Biochemie* of the *Justus-Liebig-Universität Gießen* at an ambient temperature of $22.5\,°C$ and air humidity of

(50 - 55)% on a 12 h:12 h light:dark cycle with free access to water and food until the time of the experiment. Then, animals were killed by stunning followed by exsanguination. The abdominal cavity was opened following the *linea alba*. The experiments were approved by *Regierungspräsidium Gießen*, Gießen, Germany and performed according to the German and European animal welfare law.

The myenteric plexus embedded in the *muscularis propria*, *id est* the longitudinal muscle in Figure 3.8, was obtained from adult rats. For this purpose, the colon was removed and placed on a small plastic rod with a diameter of
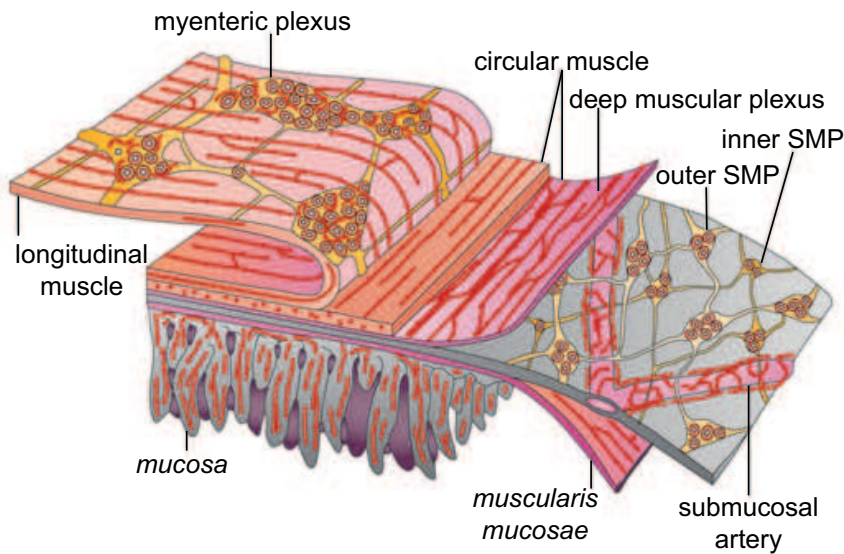


*Figure* 3.8 *Diagram showing the arrangement of the enteric plexuses on a segment of intestine which has been partly separated into layers. Abbreviations: ENS, enteric nervous system; SMP, submucosal plexus. Adapted by permission from Macmillan Publishers Ltd: Nature Reviews Gastroenterology and Hepatology [108], copyright 2012.*

5 mm. A circular incision was made near the anal end with a blunt scalpel. Then, the *serosa*, *id est* the outmost layer of the intestinal wall (not shown in Figure 3.8), and *muscularis propria* embedding the myenteric plexus, were gently removed in the proximal direction and transferred to an ice-cooled glass plate. The distal end of this tissue was then dissected into small pieces of about (1 mm × 2 mm) ready for use. One piece was placed on each gate of an AcFET as shown in Figure 3.9A using fine forceps, covered by polyester gauze (pore size 70 µm) and fixed with a plastic clip. The thus prepared samples were then placed into 37 °C warm Tyrode's solution (for preparation see ap-

pendix C.2) and immediately transported to the *I. Physikalisches Institut* for measurement.

Myenteric neuron isolation and culture was carried out according to the procedure described in [109]: The small intestine of $(4\text{-}12)$ days old rats was collected under a binocular microscope and placed into $Ca^{2+}$- and $Mg^{2+}$-free Hanks' balanced salt solution (HBSS) supplemented with 1% (v/v) PenStrep (Life Technologies, Darmstadt, Germany). The *muscularis propria* was stripped off using two fine forceps and then incubated in a collagenase type II solution ($0.5\,\text{mg}\,\text{ml}^{-1}$; Biochrom, Berlin, Germany) at $37\,^{\circ}\text{C}$ for $80\,\text{min}$. Under
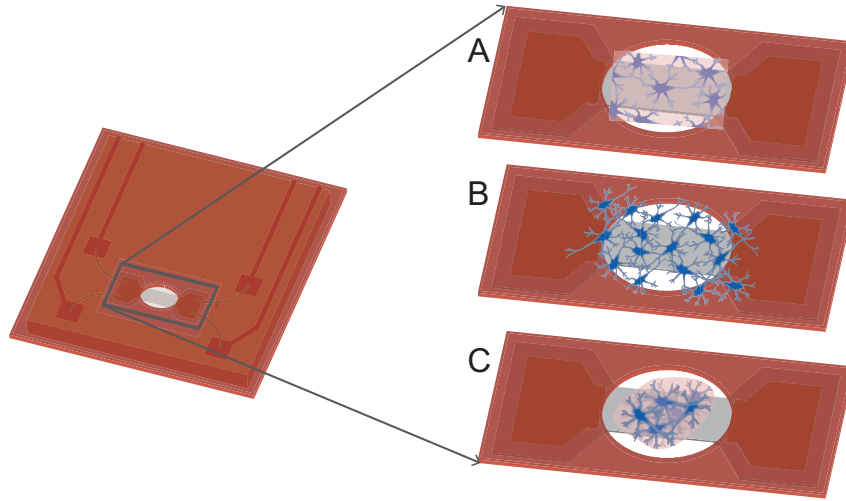


*Figure* 3.9 *Illustration of the placement of (A) myenteric neurons from the myenteric plexus still embedded in the muscularis propria, (B) isolated myenteric neurons and (C) coeliac ganglion on the gate area of an AcFET.*

optical control the myenteric ganglia forming net-like structures were collected using a micropipette and placed into warm Neurobasal medium (Life Technologies, Darmstadt, Germany) supplemented with 0.25% (v/v) L-glutamine (Sigma-Aldrich, Taufkirchen, Germany), 1% (v/v) PenStrep and 10% (v/v) foetal calf serum (FCS, Biochrom, Berlin, Germany). A cell suspension was obtained by mechanical trituration, passing the ganglia through a 23G hypodermic needle ($0.60\,\text{mm} \times 60\,\text{mm}$) three to five times. Afterwards, $20\,\mu\text{l}$ of the cell suspension were transferred to the gate of the AcFET which was incuba-
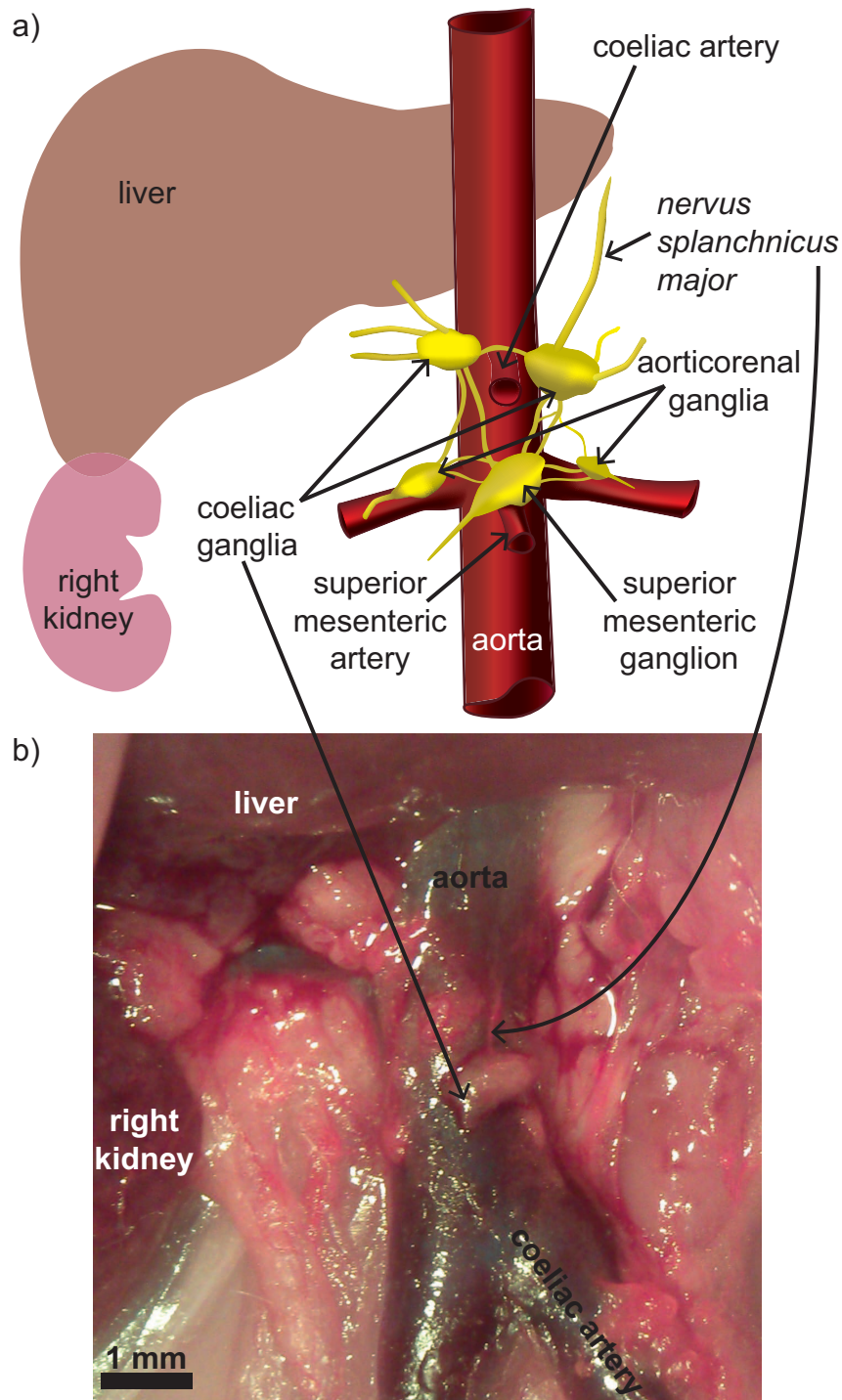
*Figure* 3.10 *a) Diagram showing the position of the coeliac ganglia within the coeliac plexus. Adapted by permission from Radiological Society of North America: RadioGraphics [110], copyright 2011. b) Photograph of a section of the abdomen of a Wistar rat revealing a coeliac ganglion. Courtesy of Ervice Pouokam, Ph.D..*

ted overnight at 37 °C in an atmosphere of 5% (v/v) $CO_2$ in 95% (v/v) air. The result is a self-adhering layer of isolated neurons that does not cover the gate area completely as it is schematically illustrated in Figure 3.9B. For transport to the *I. Physikalisches Institut* the samples were placed in 37 °C warm Tyrode's solution.

The coeliac ganglia were collected from adult Wistar rats. They are situated at the branching point of the coeliac artery and the aorta as depicted in Figure 3.10. To get access to the ganglia, colon, stomach, kidneys, liver and spleen were moved cranialwards after the abdominal cavity was opened. After freeing the aorta from fatty tissue with fine forceps, the coeliac ganglion was cut off using a scalpel and cleaned in isotonic 10 mM PBS solution (P4417; Sigma, Taufkirchen, Germany). Then, the coeliac ganglion was placed on the gate of an AcFET as schematically shown in Figure 3.9C. To hold the ganglion in place it was covered with polyester gauze which was fixed with a plastic clip. For transport the sample was placed in 37 °C warm Tyrode's solution. The measurement monitoring neuronal activity took place immediately after samples arrival at the *I. Physikalisches Institut*.

## 3.4 Potentiometric Measurements

### 3.4.1 Measurement Set-Up

All measurements were conducted in the measurement set-up depicted in Figure 3.11. The three-electrode measurement set-up consisted of a Ag/AgCl reference electrode (6.0726.117; Metrohm, Essen, Germany), a platinum counter electrode (6.0343.000; Metrohm, Essen, Germany) and the AlGaN/GaN FET as working electrode. The position of the electrodes relative to each other was given by the layout of the chamber lid resulting in a distance of 27 mm between reference electrode and the gate of the AlGaN/GaN FET.

The measurement chamber contained a fluid volume of 100 ml with the temperature of the electrolyte being controlled with a continuous-flow water heater/chiller that pumped heated or cooled water through the double-walled measurement chamber. Additionally, the electrolyte was stirred with a DC motor (114886; Maxon Motor, Munich, Germany) controlled by a potentiometer.

The three-electrode measurement set-up was placed in a Faraday cage through-out the experiments which itself was placed into a walk-in Faraday cage which contained the measurement electronics, *id est* the potenstionstat (LPG03; Bank Elektronik, Garbenteich, Germany), the source-meter (2636A; Keithley, Germering, Germany) and the pH-electrode containing a temperature sensor (51343054; Mettler-Toledo, Gießen, Germany). The computer for data acquisition, excluding the monitor, mouse and keyboard, as well as the continuous-flow water heater/chiller were placed outside the walk-in Faraday cage.
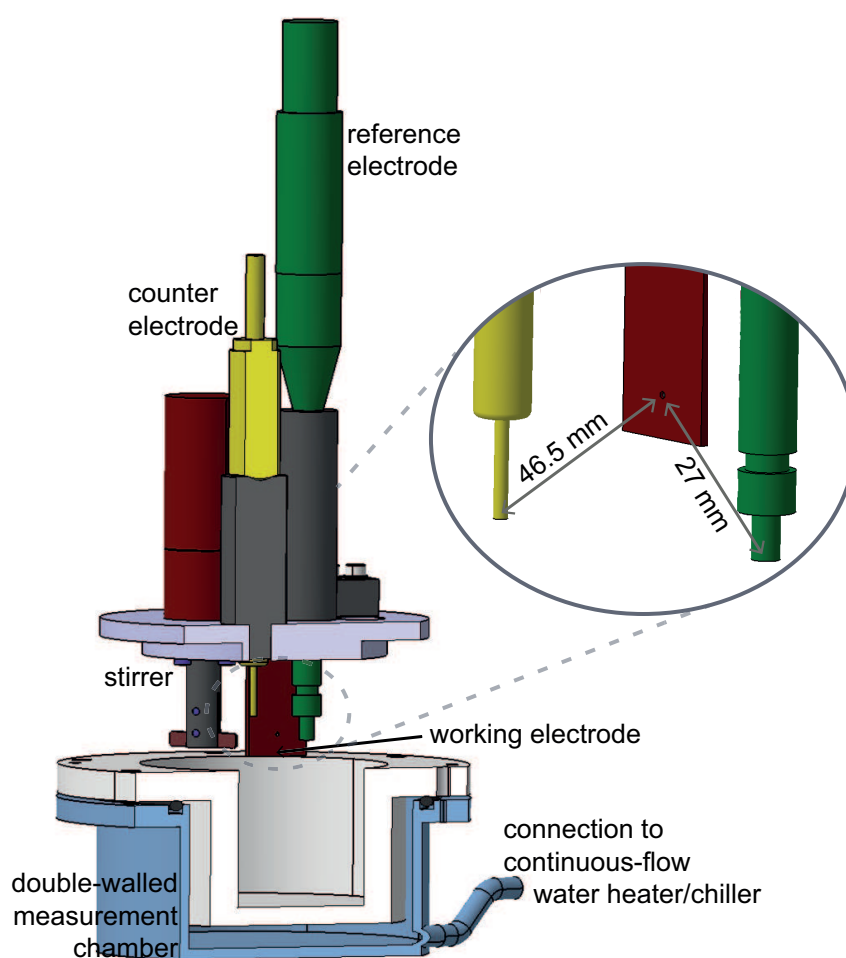


*Figure* 3.11 *Detailed drawing of the three-electrode measurement set-up with the distances between the electrodes given in the detail view. Courtesy of Dipl.-Ing. Thomas Wasem.*

## 3.4.2 Measurement Routines

All measurements were carried out in darkness and the samples were handled under darkroom conditions from at least 12 h before the respective experiments to exclude artifacts caused by persistent photocurrent (cf. section 2.1). For experiments the EnFETs were operated at a constant drain-source voltage ($U_{DS}$) of 200 mV applied by the source-meter. The constant anodic gate-source potential ($U_{GS}$) of −1.65 V was applied via the Ag/AgCl reference electrode by a potenstionstat resulting in a transconductance of about 60 µS during operation (indicated by the dashed line in Figure 3.3).

Before data acquisition, the EnFETs had to equilibrate with the surrounding electrolyte. The $I_{DS}$ transient was recorded prior to each measurement until a linear drift was obtained which indicates an equilibrated EnFET.

Calibration measurements and stability tests were performed in current-clamping mode where $U_{GS}$ was adjusted with a computer-controlled potentiostat in order to compensate the changes in $I_{DS}$ caused by a change in pH due to the formation of acid in the enzymatic reaction of the enzymes AChE and penicillinase (cf. Figure 2.7). The recorded data is the transient of the needed change in $U_{GS}$ ($\Delta U_{GS}$) to keep $I_{DS}$ constant. This measurement mode is schematically depicted in Figure 3.12. If not stated otherwise, the used electrolyte for those measurements was a stirred PBS solution with a buffer concentration $[BF]^E$ of 0.5 mM.

For analysis of the PenFET response, the pH was set to 7 while the temperature of the electrolyte was set to 25 °C, controlled with the pH-electrode containing a temperature sensor. The concentration of the substrate benzylpenicillin (1658 units/mg solid; Sigma, Taufkirchen, Germany) was varied by pipetting from a 100 mM stock solution at intervals of 100 s. The stock solution was freshly prepared with the same PBS solution ([BF] = 0.5 mM) used in the measurement chamber.

In case of AChE, the temperature of the electrolyte throughout the calibration measurements and the stability tests was 35 °C. The electrolyte's pH was 7.7 for the calibration measurements while the stability tests were performed at pH 7.5, mimicking physiological conditions for measuring vital tissue and cells. The substrate used to obtain the AcFET response curves was acetylthiocholine (ATCh; ≥99%; Sigma, Taufkirchen, Germany), an analog of the neurotransmitter ACh which is equally processed by AChE as ACh [111]. The ATCh

concentration ([ATCh]) was changed by pipetting from a 100 mM stock solution at intervals of 150 s. The stock solution was freshly prepared prior to each experiment with the same PBS solution ([BF] = 0.5 mM) used in the measurement chamber during the experiment.
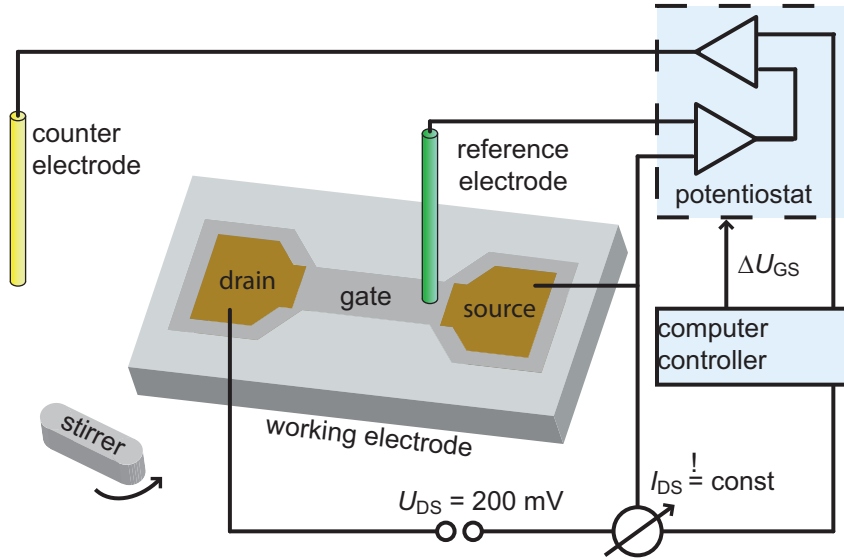


*Figure* 3.12 *Schematic representation of the measurement set-up in current-clamping mode.*

For neuronal activity measurements of myenteric neurons from the myenteric plexus embedded in the *muscularis propria*, isolated myenteric neurons, and coeliac ganglia, as well as the corresponding reference measurements only AcFETs were used. Here, $U_{GS}$ was clamped and the $I_{DS}$ transients were recorded to avoid interference of the PID controller used in current clamping mode. All measurements concerning monitoring of neuronal activity have been carried out in a stirred modified Tyrode's solution with a phosphate buffer concentration of 1 mM (for preparation see appendix C.3). Temperature and pH of the modified Tyrode's solution were set to 35 °C and 7.5, respectively. To stimulate the neurons, the membrane was depolarized by rising the extracellular $K^+$-concentration by 30 mM, using a 3 M KCl stock solution (Carl Roth, Karlsruhe, Germany). The reversible AChE blocker donepezil (≥98%; Sigma-Aldrich, Taufkirchen, Germany) as well as ATCh were pipetted from stock solutions with a concentration of 100 mM each, which were prepared with the same modified Tyrode's solution used for the experiment. Each addition of KCl, donepezil and ATCh was recorded with regard to its volume and the time at which it was added.

### 3.4.3 Evaluation Routines

Even after euqilibrating with the surrounding electrolyte, the EnFETs exhibit a linear drift in the transients recorded either in current-clamping or in voltage-clamping mode. This behavior is attributed to the slow chemical modification of the oxide on the gate area in reference [112]. Out of this reason, the drift of the transients was individually determined over a period of 300 s, via a linear fit, before any chemical was added, and then subtracted from the recorded transients. The values obtained from those fits were within the range of $0.1\,\mu V\,s^{-1}$ to $50\,\mu V\,s^{-1}$ and $10\,pA\,s^{-1}$ to $3000\,pA\,s^{-1}$ for the measured $\Delta U_{GS}$ transients and the measured $I_{DS}$ transients, respectively.

For the analysis with the kinetic model discussed in section 2.2, the drift corrected $\Delta U_{GS}$ transients were transformed into response curves which correlate $\Delta U_{GS}$ to the administered substrate concentration.

Thereby the administered substrate concentration was calculated from the concentration of the substrate stock solution (100 mM), the volume of the measurement electrolyte (100 ml) and the total volume of the stock solution added so far, taking into account the increase in total measurement volume. The obtained values are exemplary given in red script in Figure 3.13. The corresponding value of $\Delta U_{GS}$ (orange annotations in Figure 3.13) was calculated by averaging over the 50 s period directly before the next addition of substrate (orange-highlighted section of the $\Delta U_{GS}$ transient in Figure 3.13). The relative standard deviation of this average was taken as the error of the obtained $\Delta U_{GS}$ value. As it is evident from the right hand side of Figure 3.13 the error of each $\Delta U_{GS}$ value was small. This is a representative finding for all EnFET response curves discussed here. Thus, the error bars are only shown exemplary in Figure 3.13 in this subsection and are omitted in the following for better legibility of the presented data.

The obtained EnFET response curves were then fitted according to the kinetic model of Glab *et al.* [49] which is referred to as the *kinetic model* in the following. Fitting facilitates the determination of the model parameters $K_M$, $k_V$, $\bar{k}_H$ and $\bar{k}_{BF}$ (cf. section 2.2) directly related to the covalently immobilized enzyme layer.

The method employed in the fitting routine was developed with Mathematica 9.0 (Wolfram, Long Hanborough, United Kingdom) according to reference [90] which minimizes Eq. 3.1 for $n$ pH values ($pH_i$) measured by $\Delta U_{GS}$ at a given
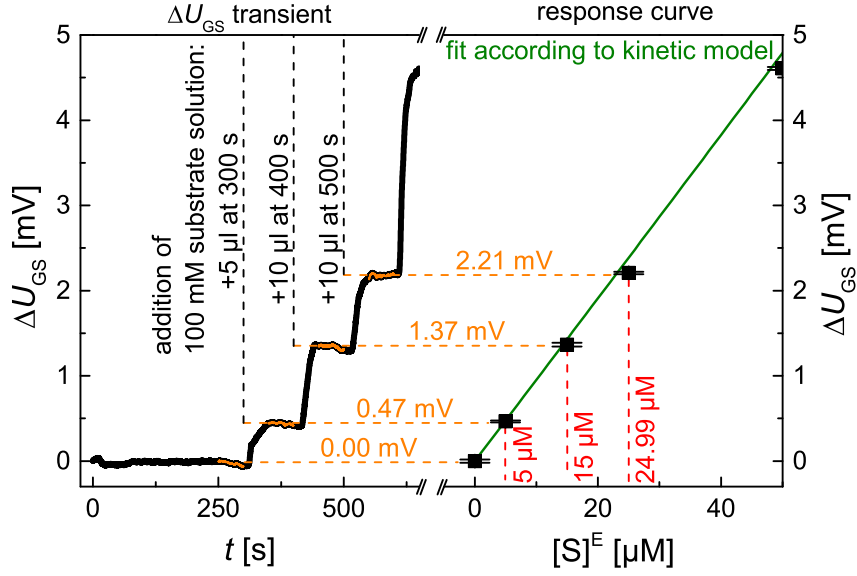
*Figure* 3.13 *Exemplary illustration of the generation of an EnFET response curve on the right hand side by means of an excerpt of a $\Delta U_{GS}$ transient on the left hand side. On the left hand side the annotations in black indicate the volume and the time at which the 100 mM substrate solution was added as marked by the black dashed line. From the 50 s period highlighted in orange in the $\Delta U_{GS}$ transient the average signal evoked by the preceding addition of substrate was calculated. Those values are represented by the orange dashed lines and stated in orange script above. The obtained values for $\Delta U_{GS}$ with their relative standard deviation taken as error bars are then plotted in black against the corresponding total substrate concentration given by the dashed red lines and the corresponding annotation in red yielding the EnFET response curve. The green line represents the fit according to the kinetic model outlined in section 2.2.*

substrate concentration $[S]^E$ while $pH_i([S]^E)$ denotes the $i^{th}$ corresponding pH value as calculated by the *kinetic model* by means of Eq. 2.18 with the variable parameters $K_M$, $k_V$, $\bar{k}_H$ and $\bar{k}_{BF}$.

The minimization of Eq. 3.1 was realized by utilizing the function "NMinimize" with the method option "NelderMead" and the model parameters being restricted to values greater zero. The result of Eq. 3.1, the parameter $\Phi$, is as well a measure for the fit quality. It was smaller than 0.01 for all fits presented in this work.

$$\Phi = \sum_{i=1}^{n} \left[ pH_i - pH_i\left( [S]^E \right) \right]^2 \tag{3.1}$$

## 3.5 Viability Assays

### 3.5.1 Fluorometric Calcium Imaging

The vitality of the myenteric neurons from the myenteric plexus embedded in the *muscularis propria* after experiments monitoring neuronal activity was tested pharmacologically. The investigation consisted in testing the ability of the tissue sample to respond to calcium mobilizing drugs such as nicotine (Sigma-Aldrich, Taufkirchen, Germany) or cyclopiazonic acid (CPA; Alexis, Grünberg, Germany) in concentrations of $100\,\mu M$ and $50\,\mu M$, respectively.

For this purpose, calcium imaging experiments were run using fura-2 acetoxymethylester (Life Technologies, Darmstadt, Germany), a $Ca^{2+}$-sensitive fluorescent dye [113]. The pieces of *muscularis propria* collected from the gate were attached to cover slips (diameter: $13\,mm$) coated with poly-L-lysine (molecular weight $> 300{,}000\,g\,mol^{-1}$; Biochrom, Berlin, Germany) and incubated in standard Tyrode's solution with $2.5\,\mu M$ fura-2 acetoxymethylester and $0.05\,g\,l^{-1}$ pluronic acid (Life Technologies, Darmstadt, Germany) at $37\,°C$ for $40\,min$. For experiments, the cover slip was put into an experimental chamber which held the cover slip in place and allowed covering of the sample with solution. The experimental chamber was then placed on an inverted microscope (Olympus IX-50; Olympus, Hamburg, Germany), equipped with an epifluorescence set-up as well as an image analysis system (Till Photonics, Martinsried, Germany), and covered with $1\,ml$ Tyrode's solution.

Several regions of interest containing neurons, each with the size of about one cell, were selected. The emission was measured from the regions of interest with a sample rate of $0.2\,Hz$ for wavelengths above $420\,nm$. The changes in cytosolic $Ca^{2+}$-concentration were expressed as changes in the fura-2 ratio, *id est* the emission value at an excitation wavelength of $340\,nm$ divided by the emission value at an excitation wavelength of $380\,nm$. Nicotine and CPA were pipetted from stock solutions with concentrations of $50\,mM$ and $10\,mM$, respectively (for preparation see appendix E.1).

## 3.5.2 Immunocytochemistry and Propidium Iodide Staining

The vitality of isolated myenteric neurons cultured on gates of capsule-free AcFETs was tested by means of immunocytochemistry and staining with propidium iodide.

Prior to the vitality test, the samples were submitted to the same conditions as during routinely performed potentiometric measurements monitoring neuronal activity (cf. section 3.4). Thereafter, they were exposed to aqueous propidium iodide solution ($300\,\mu$M; from $\geq 94.0\%$; Sigma, Taufkirchen, Germany) for $5\,$min at $37\,°$C. The free gates carrying the myenteric cells were rinsed with prewarmed isotonic $10\,$mM PBS solution. Then, the cells were fixed in a solution of $4\%$ (w/v) paraformaldehyde ($95\%$; Sigma-Aldrich, Taufkirchen, Germany) and $2\%$ (w/v) sucrose ($\geq 99.0\%$; Sigma-Aldrich, Taufkirchen, Germany) for $5\,$min at $37\,°$C. The fixation was stopped by rinsing the cells three times, $5\,$min each with warm isotonic $10\,$mM PBS solution. The cells were then incubated for $30\,$min in warm isotonic $10\,$mM PBS solution containing $0.05\%$ (w/v) Tween 20 (Sigma-Aldrich, Taufkirchen, Germany) for permeabilization and $4\%$ (w/v) bovine serum albumin (BSA; $\geq 98\%$; Sigma-Aldrich, Taufkirchen, Germany) in order to block unspecific bindings. The neurons were then incubated overnight at $4\,°$C with the primary antibody mouse monoclonal anti-microtubule-associated protein 2 (anti-MAP2; Sigma-Aldrich, Taufkirchen, Germany), used as neuronal marker [114] (final dilution 1:400). The latter was dissolved in isotonic $10\,$mM PBS solution containing $1\%$ (w/v) BSA, $0.05\%$ (v/v) Tween 20 and $1\%$ (v/v) donkey serum (Merck Millipore, Darmstadt, Germany).

After removing unbound primary antibody by rinsing three times for $5\,$min with isotonic $10\,$mM PBS solution, the cells were incubated at room temperature in the dark for $1\,$h with the fluorescent secondary antibody Alexa-488-donkey anti-mouse IgG (final dilution 1:400; Invitrogen, Karlsruhe, Germany) dissolved in isotonic $10\,$mM PBS solution containing $1\%$ (w/v) BSA and $0.05\%$ (v/v) Tween 20. The cells were examined with a fluorescence microscope (80i; Nikon, Düsseldorf, Germany). Digital images were taken with a black and white camera (DS-2M B/Wc) using NIS Elements 2.30 software (all from Nikon, Düsseldorf, Germany) to adjust the color.

# 4 Results and Discussion

## 4.1 Penicillinase-Modified Field-Effect Transistors

The basis for optimizing the EnFET performance is a profound understanding of its response characteristics and the properties of the immobilized enzyme layer. In case of EnFETs based on pH-sensitive potentiometric sensors such as AlGaN/GaN SGFETs investigated here, this understanding can be gained by quantitative analysis with the *kinetic model* as discussed in section 2.2. One requirement of this *kinetic model* is an enzyme layer which is not limited by diffusive processes, *id est* a fast exchange of substrate molecules and reaction products across the enzyme layer/electrolyte interface is warranted. Furthermore, the stability and reproducibility of the immobilization process has to be ensured. Both requirements can be met if the EnFET preparation method described in section 3.2 is used [2] as will be shown in the following.

The applicability and strength of their *kinetic model* was already investigated by Glab *et al.* for the example of the enzyme urease [115] immobilized on a pH-sensitive glass electrode. Throughout their studies they analyzed the effect of buffer concentration, pH and stirring rate on the response curves of this device for the detection of urea. However, the only two model parameters systematically investigated were $K_M$ and $k_V$, which are directly related to the enzymatic activity. The other two model parameters, $\bar{k}_H$ and $\bar{k}_{BF}$, were kept at a constant value of 1.

In the work presented in this section the enzyme penicillinase from *bacillus cereus* covalently immobilized on a pH-sensitive AlGaN/GaN FET according to the procedure described in subsection 3.2.2 is quantitatively investigated by application of the *kinetic model*. Furthermore, in contrast to the work by Glab *et al.*, all four model parameters $K_M$, $k_V$, $\bar{k}_H$ and $\bar{k}_{BF}$ are determined by a fit of the experimental data.

The applicability of the *kinetic model* for analyzing response curves of Pen-FETs is generally shown for the case of varying buffer concentrations $[BF]^E$. In view of the results obtained through this analysis, the stability and reproducibility of PenFETs as well as the influence of pH on the PenFET response curves have been quantitatively investigated.

## 4.1.1 Variation of Phosphate Buffer Concentration

In a first experiment response curves of one PenFET measured in test solutions with $[BF]^E$ equal to $0.5\,\text{mM}$, $1\,\text{mM}$, $2\,\text{mM}$ and $5\,\text{mM}$ were analyzed with the *kinetic model*. In all response curves shown in Figure 4.1 a sensitive region defining the sensitivity of the PenFET, and a saturation region can be distinguished. The onset of the saturation signal defines the highest $[S]^E$ and thus the highest $[H]$ measurable by a change of $\Delta U_{\text{GS}}$ at the gate area. The position of this onset is not influenced by $[BF]^E$. With increasing $[BF]^E$ the experimental results depicted by symbols in Figure 4.1 show a decrease of sensitivity
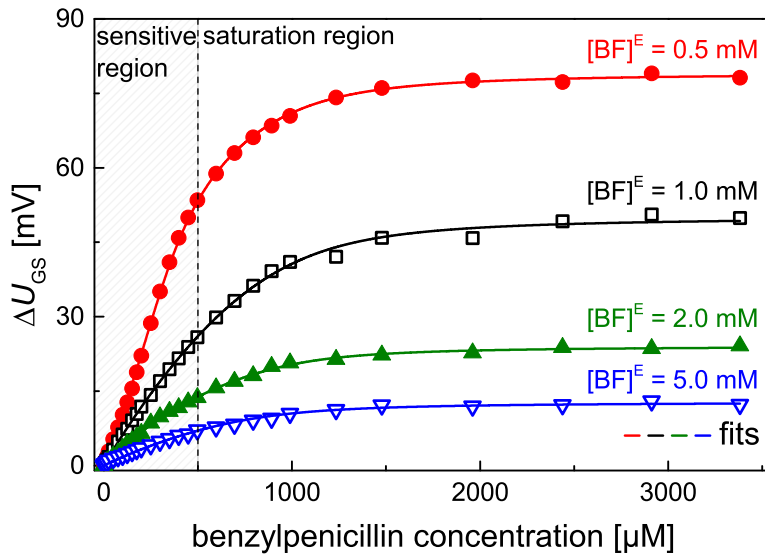


*Figure* 4.1 *Influence of* $[BF]^E$ *on the response curves of PenFETs. Response curves (symbols) obtained in test solutions with different* $[BF]^E$ *as indicated. Solid lines represent fits according to kinetic model.*

in the sensitive region as well as a decrease of the saturation signal in the saturation region. Furthermore, for all four response curves the fits according to the *kinetic model* (solid lines) show excellent agreement with the experimental

results. The quality of the fits is also evident from the fit quality parameter $\Phi$ (cf. Eq. 3.1) listed in Table 4.1 being always smaller than 0.01 (cf. subsection 3.4.3).

From the fitting results summarized in Table 4.1 one can deduce that $K_M$ ((85 ± 6) µM) and $k_V$ ((1.03 ± 0.08) mM) are constant within the measurement accuracy and not systematically affected by the change in $[BF]^E$. On the contrary, $\bar{k}_H$ increases by two orders of magnitude while $\bar{k}_{BF}$ decreases by three orders of magnitude with increasing $[BF]^E$. Hence, only the two parameters directly related to the buffer system react to changes in $[BF]^E$, while those that characterize the immobilized enzyme layer remain almost constant.

Table 4.1 *Extracted model parameters for the variation of $[BF]^E$.*

| $[BF]^E$ [mM] | $K_M$ [µM] | $k_V$ [mM] | $\bar{k}_H$ | $\bar{k}_{BF}$ | $\Phi$ |
|---|---|---|---|---|---|
| 0.5 | 86 | 1.11 | 97 | 1.79 | 0.002 |
| 1.0 | 87 | 1.11 | 1531 | 1.02 | 0.004 |
| 2.0 | 73 | 1.01 | 5112 | 0.02 | 0.001 |
| 5.0 | 95 | 0.90 | 10744 | 0.001 | 0.001 |

As $K_M$ is almost constant it is a reasonable assumption that $v_{max} = k_2 \cdot [E]_0$ is also constant for varying $[BF]^E$ (cf. Eq. 2.15). As $k_V$ does not vary with $[BF]^E$ and equals $v_{max}/k_S$ it follows that $k_S$ is constant as well. Consequently, the increase in $\bar{k}_H$ is equivalent to an increase in $k_H$ and the decrease in $\bar{k}_{BF}$ is equivalent to a decrease in $k_{BF}$.

The increase in $\bar{k}_H$ is tantamount to a faster proton transport from the enzyme layer to the electrolyte. As a result the proton concentration at the pH-sensitive gate surface is smaller, leading to a decreasing saturation signal. In contrast, the observed decrease in $\bar{k}_{BF}$ with increasing [BF] should lead to an increase of the saturation signal (cf. Figure 2.9d)). However, the effect $\bar{k}_{BF}$ has on the response curves by decreasing from 1.79 to 0.001 (cf. Table 4.1) is considerably smaller than the increase of $\bar{k}_H$ from 97 to 10744 (cf. Figure 2.9) explaining the decrease of the saturation signal with increasing [BF].

## 4.1.2 Reproducibility and Stability

The results in the proceeding paragraph demonstrate that the *kinetic model* is applicable for the quantitative analysis of PenFET response curves. Based

on these results, the reproducibility and stability of AlGaN/GaN PenFETs are quantitatively investigated in this subsection.

The reproducibility of the PenFET preparation was analyzed by comparing PenFET response curves after different numbers of measurement cycles from different production dates. In Figure 4.2 four different PenFETs from four different production dates are analyzed, demonstrating a high level of reproducibility. The inset in Figure 4.2 illustrates separately that the sensitivity of
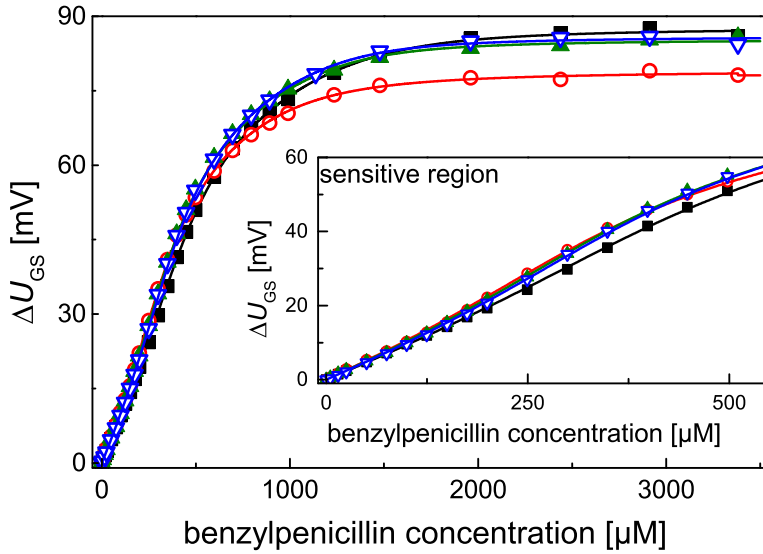


*Figure* 4.2 *Comparison of the response curves of four different PenFETs at pH 7.0. The inset shows the sensitive regions for benzylpenicillin concentrations below 500 μM. Solid lines represent fits.*

PenFETs in the sensitive region is reproducible as well. The small deviation of the saturation signal by about 8% can be attributed to a differing amount of enzyme present on the gate surface. This effect will be discussed in greater detail in subsection 4.2.2.

The comparison of the parameters $K_\mathrm{M}$, $k_\mathrm{V}$, $\bar{k}_\mathrm{H}$ and $\bar{k}_\mathrm{BF}$ obtained from the *kinetic model* (cf. Table 4.2) indicates as well a high reproducibility as all four parameters can be regarded as constant within a small range of deviation. Thereby, the Michaelis constant with its average value of $(70 \pm 11)\,\mu\mathrm{M}$ is in good agreement with the reported value of $60\,\mu\mathrm{M}$ for free penicillinase [116].

Based on the proven reproducibility of the PenFET preparation, the stability of PenFETs is now exemplary discussed for a single PenFET. For this purpose, a PenFET was repeatedly measured and quantitatively analyzed over the course of 252 days counting from the production date. Between measure-

ments the PenFET was stored in $10\,\text{mM}$ PBS solution at a temperature of $5\,°\text{C}$.

*Table* 4.2 *Extracted model parameters for the PenFETs shown in Figure 4.2.*

| PenFET | $K_\text{M}$ [µM] | $k_\text{V}$ [mM] | $\bar{k}_\text{H}$ | $\bar{k}_\text{BF}$ |
|:---:|:---:|:---:|:---:|:---:|
| ■ | 72 | 1.57 | 143 | 1.84 |
| ○ | 86 | 1.11 | 97 | 1.79 |
| ▲ | 74 | 1.12 | 134 | 1.82 |
| ▽ | 49 | 1.37 | 98 | 1.89 |

During the first four measurements on day 0, 2, 5 and 9 the results, displayed in Figure 4.3 a), show a decrease in the saturation signal by about 25% while the slope in the sensitive region remains almost unchanged. From day 9 (4th measurement) on no further changes in the response curves are observed until day 56 (9th measurement). As depicted in Figure 4.3b), starting from the 9th measurement the saturation signal as well as the slope of the sensitive region decrease until stable response curves are obtained from day 182 (13th measurement) on. This development of the PenFET characteristics can also be comprehended in terms of the extracted model parameters $K_\text{M}$, $k_\text{V}$, $\bar{k}_\text{H}$ and $\bar{k}_\text{BF}$ shown in Figure 4.4.

Throughout the first period from day 0 (1st measurement) to day 42 (8th measurement) highlighted in Figure 4.3a) the values obtained for $K_\text{M}$ are fairly constant, resulting in a mean value of $(67 \pm 10)\,\text{µM}$ when averaging from the 1st to the 8th measurement; in good agreement with the value obtained for the analysis of the reproducibility $((70 \pm 11)\,\text{µM})$. Hence, $K_\text{M}$ is also in good agreement with the published value of $K_\text{M} = 60\,\text{µM}$ for free penicillinase [116]. This finding indicates that the covalent immobilization process applied here does not lead to a sizable deterioration of the enzymatic activity.

Taking Eq. 2.16 into account, it follows that $k_2$ can be assumed as constant, *id est* the catalytic activity of penicillinase is not changed over time. As $k_\text{V} = k_2 \cdot [\text{E}]_0/k_\text{S}$ in the saturation region, the decrease in $k_\text{V}$ from the 1st measurement on can be attributed to a decrease in the density of enzymes on the gate area $[\text{E}]_0$ or/and an increase of the substrate transport rate constant $k_\text{S}$. As $\bar{k}_\text{BF}$ with an average value of $(1.8 \pm 0.1)$ is almost constant throughout the first period $k_\text{S}$ can only increase similar to $k_\text{BF}$. Furthermore, $\bar{k}_\text{H}$ increases from 85 (day 0) to an average value of $125 \pm 19$ (day 9 to day 42) suggesting an increasing permeability of the penicillinase layer. Hence, the decrease

in $k_V$ is attributed to a decrease in $[E]_0$, *id est* a detachment of physisorbed penicillinase, during the first nine days of storage.
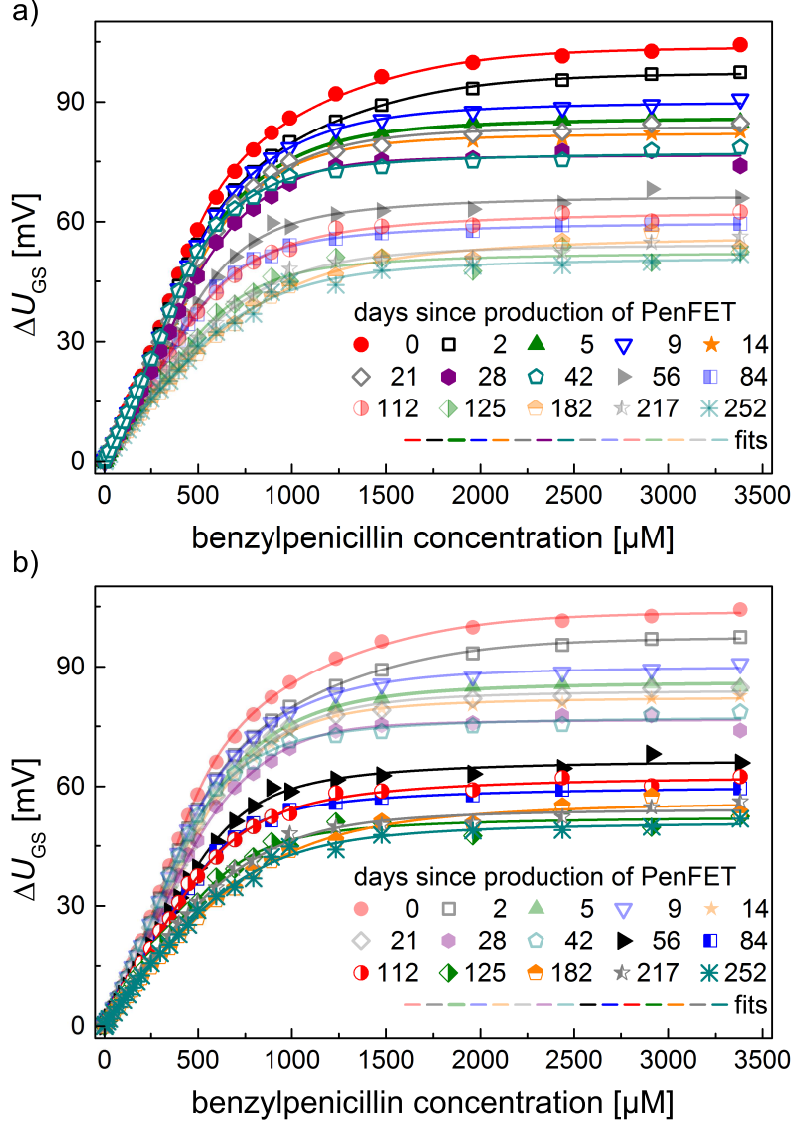


*Figure* 4.3 *Chronological development of PenFET response curves over the course of 252 days (symbols) and fits according to the kinetic model (solid lines). In a) day 0 to day 42 (first period), in b) day 56 to day 252 (second period) are highlighted.*

In the course of the second period from day 56 to day 252 highlighted in Figure 4.3b) $K_M$ increases from $(67 \pm 10)\,\mu M$ to $(107 \pm 29)\,\mu M$ (average of the values from days 182, 217 and 252). As $K_M$ equals $(k_{-1} + k_2)/k_1$, the ratio of the reaction constants of the dissociation $(k_{-1} + k_2)$ and formation $(k_1)$ of the enzyme-substrate complex, this increase could be due to an increased dissoci-

ation rate or a decreased formation rate of the enzyme-substrate complex. As an increase of $k_2$, *id est* a faster enzymatic conversion of benzylpenicillin, due to storage is unlikely, a decrease in $k_1$ or an increase in $k_{-1}$, occurring when storage exceeds 42 days, is more plausible.
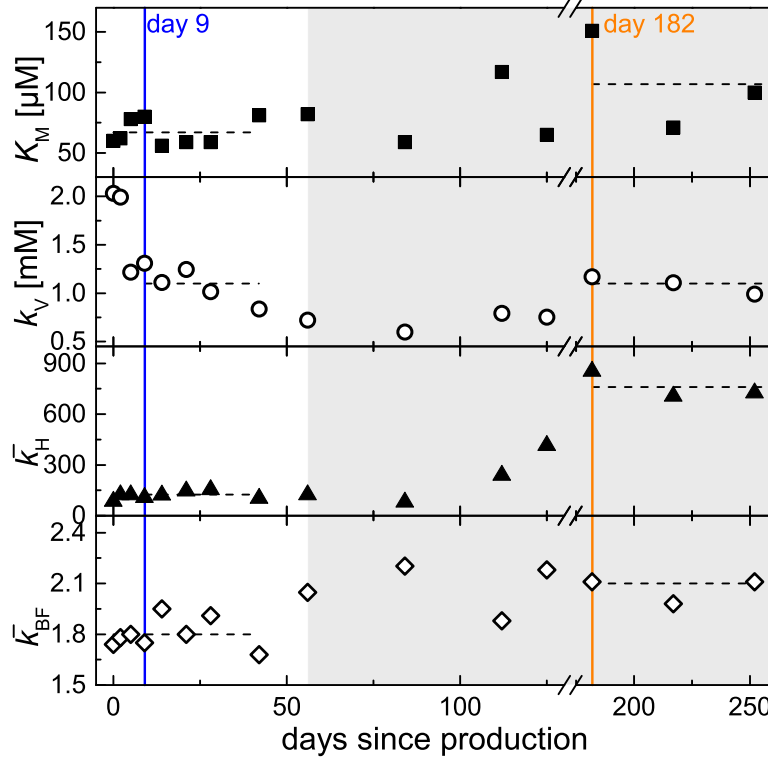


*Figure 4.4 Evolution of the extracted model parameters of the PenFET response curves shown in Figure 4.3. The first period from day 0 to day 42 corresponds to the highlighted response curves in Figure 4.3a) while the second period from day 56 to day 252 (highlighted in gray) corresponds to the highlighted response curves in Figure 4.3b). The dashed lines indicate the mean value of the respective model parameter as discussed in the text.*

As it is evident from Figure 4.4, $k_V$, $\bar{k}_H$ and $\bar{k}_{BF}$ increase as well throughout the second period highlighted in gray until they reach constant values of $(1.1 \pm 0.1)$ mM, $(761 \pm 61)$ and $(2.1 \pm 0.1)$ from day 182 (13$^{\text{th}}$ measurement) on. This increase can be explained by a decrease in the transport rate constant $k_S$ which equally affects all three parameters. As $k_S$ depends on the difference in concentration of the substrate between the bulk electrolyte and the enzyme layer, a decrease in $k_S$ is related to a smaller concentration differnce which can be either explained by a lower amount of active penicillinase on the gate

surface and/or a partial denaturation of penicillinase as discussed above. Because the decrease in $k_V$ throughout the first period was attributed to a detachment of physisorbed penicillinase a renewed occurrence of enzyme detachment from day 56 on can be ruled out. Hence, a detachment of physisorbed penicillinase cannot be responsible for the decrease in $k_S$. If instead the cleavage of the covalent bond anchoring penicillinase to the gate surface should be the reason for a detachment of penicillinase one would expect a continuous deterioration of the PenFET characteristics. However, this behavior could not be observed as stable response curves are received from day 182 on. Hence, only a partial denaturation of penicillinase can explain the decrease in $k_S$ and thus the increase of $k_V$, $\bar{k}_H$ and $\bar{k}_{BF}$ over the course of the second period.

In summary, the results in this subsection show that the employed PenFET preparation method is reproducible and that the changes observed in PenFET response curves over the course of 252 days can be attributed to a detachment of physisorbed penicillinase throughout the first nine days of storage as well as the denaturation of the penicillinase occurring between day 56 to day 182.

## 4.1.3 Variation of pH

In this subsection the influence of the pH of the bulk electrolyte, $-\lg([H]^E)$, on the PenFET response curves is investigated for pH-values of 6, 7, and 8. As shown in Figure 4.5 a change from pH 8 to pH 7 reduces the magnitude of the saturation signal by about 20%, while the sensitive region is only slightly affected. According to reference [117] the enzymatic activity of penicillinase is not pH-dependent in the investigated pH-range and thus $K_M$ and $v_{max}$ can be regarded as constant between pH 7 and pH 8. The transport rate constants $k_S$ and $k_{BF}$ should neither be influenced by a change in $[H]^E$. Hence, the only model parameter that might be affected by changing pH is $\bar{k}_H$ which depends on the proton transport rate constant $k_H$.

The values determined for $K_M$ at pH 8 and pH 7 listed in Table 4.3 are in the range of the $K_M$ values obtained for PenFETs in the first period of their chronological development $((67 \pm 10)\,\mu M)$. The model parameter $\bar{k}_{BF}$ can be regarded as constant, while the model parameters $k_V$ and $\bar{k}_H$ differ by about a factor of 2. This deviation might be explained by the fact that benyzlpenicillin can be degraded by nucleophilic attack, *exempli gratia* hydroxide ions [118]. As this degradation path plays a minor role at a weak basic pH of 8, the

*kinetic model* is still considered applicable at pH 8. However, the deviation of the values $k_V$ and $\bar{k}_H$ is neglected.

On this account, the decrease in saturation signal from pH 8 to pH 7 is not explainable by the extracted model parameters. Rather, the decrease in saturation signal can be attributed to the attenuated dissociation of penicilloic acid, reflected by the dissociation constant $K_{aP}$. As the decadic logarithm
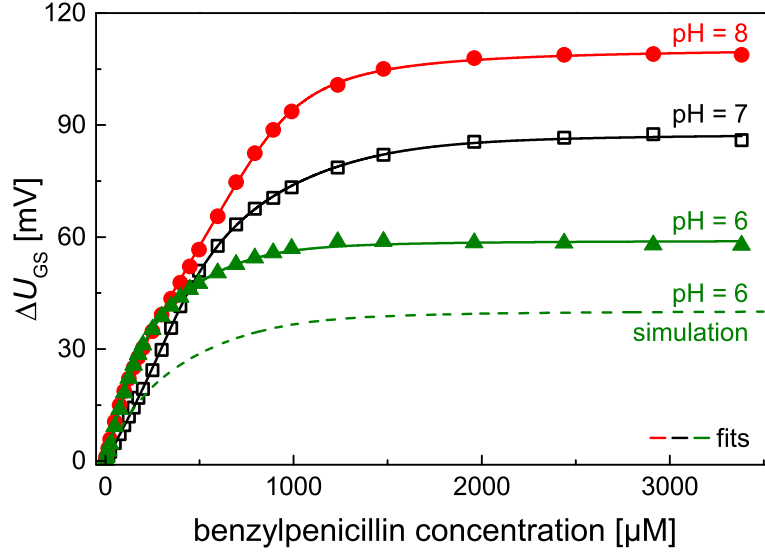


*Figure* 4.5 *Influence of bulk electrolyte pH on the response curves of PenFETs.*
*The measured response curves obtained in test solutions with dif-*
*ferent pH values are shown as symbols. Solid lines represent fits,*
*dashed lines represent simulations with kinetic model.*

of $K_{aP}$ equals 5.2 [119] the PenFET signal describable by the *kinetic model* should decrease with decreasing pH until it vanishes for pH $<$ 5.2.

If comparing the response curves at pH 6 (green triangles) and pH 7 (black open squares) as well as their respective fits (solid lines) to the simulation at pH 6 (dashed line, model parameters: $K_M$ = 70 $\mu$M, $k_V$ = 1 mM, $\bar{k}_H$ = 100, $\bar{k}_{BF}$ = 1.8), a discrepancy to the *kinetic model* is evident. Compared to the simulation at pH 6 the measured response curve displays a steeper slope in the sensitive region and an elevated saturation signal. Those findings suggest that penicillinase is a faster working enzyme with a higher reaction rate at pH 6. However, according to reference [117] the enzymatic activity of penicillinase is not enhanced at pH 6 when compared to pH 7 and pH 8. The reason for the higher substrate turnover measured is rather the protolytic degradation of benzylpenicillin in acidic solutions. As this acid-induced degradation

of benzylpenicillin yields the same products as the enzymatic reaction [118], the resulting response curve at pH 6 cannot be explained by the *kinetic model* alone. Out of this reason, the extracted model parameters for the variation of pH are only shown for pH 8 and pH 7 in Table 4.3.

*Table 4.3 Extracted model parameters for the variation of pH.*

| pH | $K_M$ [μM] | $k_V$ [mM] | $\bar{k}_H$ | $\bar{k}_{BF}$ |
|---|---|---|---|---|
| 8 | 52 | 0.92 | 73 | 1.72 |
| 7 | 72 | 1.57 | 143 | 1.84 |
| 6 | - | - | - | - |

Hence, the applicability of the *kinetic model* is limited if the substrate can be also degraded by an alternative reaction introduced by the measurement conditions that leads to the same products as the enzymatic reaction.

## 4.2 Acetylcholinesterase-Modified Field-Effect Transistors

The previous section 4.1 has shown that the *kinetic model* is an adequate tool to quantitatively analyze EnFET response curves with penicillinase covalently immobilized on an AlGaN/GaN EnFET as the pH-affecting enzyme. Those results are used in this section to assess the reproducibility and stability of the employed immobilization procedure for AChE from *electrophorus electricus* as described in subsection 3.2.2.

Further, the results obtained from the quantitative analysis of the AcFET characteristics are used for a direct and quantitative comparison of the response curves of PenFETs and AcFETs.

### 4.2.1 Reproducibility and Stability

The reproducibility of the routine utilized to prepare AcFETs is shown by the comparison of four response curves of freshly prepared AcFETs from differing production dates in Figure 4.6. The large overlap of the response curves especially in the sensitive region displayed in the inset of Figure 4.6, demonstrates

the high reproducibility of the AcFET preparation. Thereby, the AcFETs exhibit an ATCh detection limit of $1\,\mu M$ equivalent to $\Delta U_{GS} = (0.81 \pm 0.27)\,mV$. As the volume of the sensing layer can be estimated from the thickness of the AChE layer ($15\,nm$ [104, 120]) and the transistor's gate area ($1.2\,mm \times 0.5\,mm$) to be about $10^{-11}\,l$, a ATCh detection limit of $1\,\mu M$ corresponds to a total number of approximately $10^{7}$ substrate molecules ($\approx 10\,amol$) in the sensing layer.
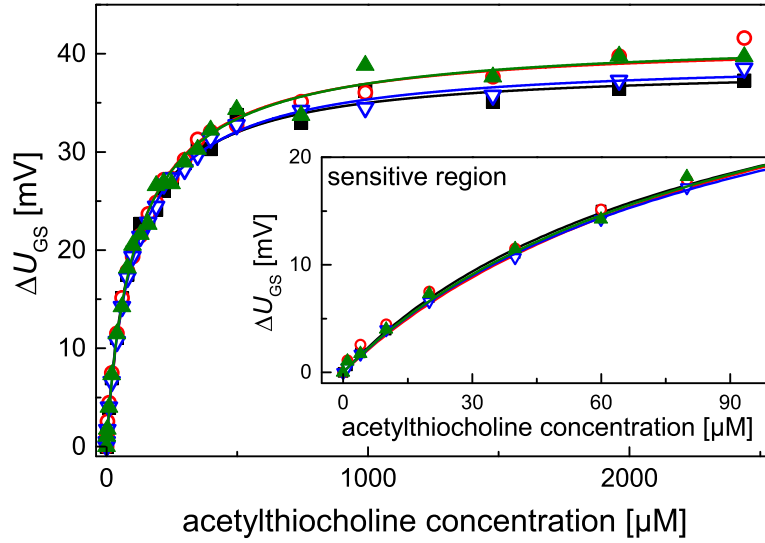


*Figure* 4.6 *Comparison of the response curves of four different AcFETs at pH 7.7. The inset shows the sensitive regions for substrate concentrations below $100\,\mu M$. Solid lines represent fits according to the kinetic model discussed in section 2.2.*

Further analysis of the response curves in Figure 4.6 with the *kinetic model* yielded an average Michealis constant $K_M$ of $(122 \pm 4)\,\mu M$ which lies within the range of $67\,\mu M$ [20] to $900\,\mu M$ [107] reported for AChE from *electrophorus electricus*. The other three extracted model parameters $k_V$, $\bar{k}_H$ and $\bar{k}_{BF}$ are given in Table 4.4. It should be noted that all these parameters are considerably smaller than 1, *id est* $v_{max}$, $k_H$, $k_{BF}$ are much smaller than $k_S$. This is in contrast to the findings for penicillinase in section 4.1. There, $k_H$ as well as $k_{BF}$ were larger than $k_S$ while the model parameter $k_V$ was about three orders of magnitude larger than in the case of AChE presented here.

It is known that AChE is a highly efficient enzyme [121] and each substrate molecule reaching the covalently immobilized AChE at the gate surface is immediately converted resulting in [ATCh] being close to zero at the gate surface.

Consequently, the large concentration difference between the gate surface and the surrounding electrolyte with a constant [ATCh] causes a higher transport rate constant $k_S$ than in case of penicillinase (cf. 2.2).

*Table* 4.4 *Extracted model parameters for the AcFETs shown in Figure 4.6.*

| AcFET | $K_M$ [µM] | $k_V$ [µM] | $\bar{k}_H$ | $\bar{k}_{BF}[10^{-2}]$ |
|:---:|:---:|:---:|:---:|:---:|
| ■ | 113 | 3.5 | 0.001 | 2.0 |
| ○ | 128 | 1.0 | 0.003 | 0.5 |
| ▲ | 123 | 0.4 | 0.021 | 0.2 |
| ▽ | 123 | 2.2 | 0.003 | 1.1 |

The AcFET stability was evaluated over the course of 77 days on the example of one single AcFET whereby storage was only interrupted for measurements. Throughout this period a total of ten measurements was taken on day 0, 2, 4, 7, 14, 21, 35, 49, 67 and 77 after preparation. However, in Figure 4.7 only eight measurements are displayed as the measurements taken on the 7th and 67th day after production underwent a drastic baseline alternation during the measurement which made it impossible to evaluate them. The reason for this was probably a change of the electrolyte temperature throughout the experiment caused by a malfunction of the continuous-flow water heater/chiller.

The results in Figure 4.7 show that the response curves change in the sensitive region as well as in the saturation region within the first two weeks of storage while from day 14 (4th measurement) on stable response curves were obtained. In this period the device sensitivity $s$ as deduced from a linear fit of the sensitive region up to [ATCh] = 100 µM decreases by about a factor of 2.9 from $(186 \pm 21)\,\mu V\,\mu M^{-1}$ on day 0 to an average value of $(65 \pm 9)\,\mu V\,\mu M^{-1}$ from day 14 on. In the same period the saturation signal is continuously lowered to approximately 50% of its original value on day 0.

The Michealis constant deduced by analysis with the *kinetic model* shows a continuous increase from 134 µM to a constant value of $(316 \pm 20)\,\mu M$ obtained by averaging all values from day 14 (4th measurement) on (cf. Figure 4.8). As $K_M$ is defined as the ratio of the reaction constants of the dissociation $(k_{-1} + k_2)$ and formation $(k_1)$ of the enzyme-substrate complex (cf. Eq. 2.16), the increase in $K_M$ can be either associated with an increased dissociation rate or a decreased formation rate of the enzyme-substrate complex. However, in case of AChE a faster conversion of its substrate ATCh into the products acetic acid and thiocholine, *exempli gratia* an increase in $k_2$, due to storage is

improbable as AChE is already one of the most efficient enzymes known [121]. Consequently, a partial denaturation of AChE during storage, which results in a slower formation of the enzyme-substrate complex - a decrease in $k_1$ - and/or its faster dissociation into substrate and enzyme - an increase in $k_{-1}$ - is a more persuasive explanation.
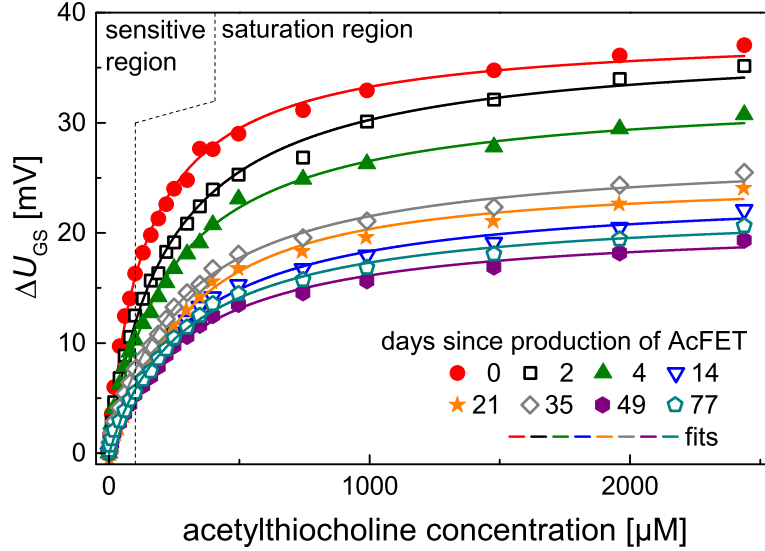


*Figure* 4.7 *Chronological development of the AlGaN/GaN AcFET response curves over the course of 77 days and their respective fits, according to the kinetic model.*

The increase in $K_M$ by a factor of 2.4 can as well explain the decrease in sensitivity by a factor of about 2.9 as the observed sensitivity depends on the velocity of the enzymatic reaction which is inversely proportional to $K_M$ for $[S] \to 0$ [88, 89].

Besides the evolution of $K_M$ and the sensitivity $s$, Figure 4.8 also depicts the evolution of the other three model parameters $k_V$, $\bar{k}_H$ and $\bar{k}_{BF}$. All three parameters, $k_V$, $\bar{k}_H$ and $\bar{k}_{BF}$, show an increase during the first four measurements until they saturate at values of $(1.8 \pm 0.7)\,\mu M$, $(0.584 \pm 0.257)$ and $(1.4 \pm 0.6) \cdot 10^{-2}$, respectively. This can be attributed to a decrease in $k_S$. As discussed above, $k_S$ depends on the differences in [ATCh] between the bulk electrolyte and the enzyme layer. Hence, a decrease in $k_S$ indicates a smaller concentration difference which can be either explained by partial denaturation of AChE and/or a lower amount of AChE on the gate surface which could be due to a detachment of AChE.

Considering the conclusions drawn above, the denaturation of AChE is the

only mutual explanation that accounts for the increase of all four model parameters within the first two weeks after preparation.
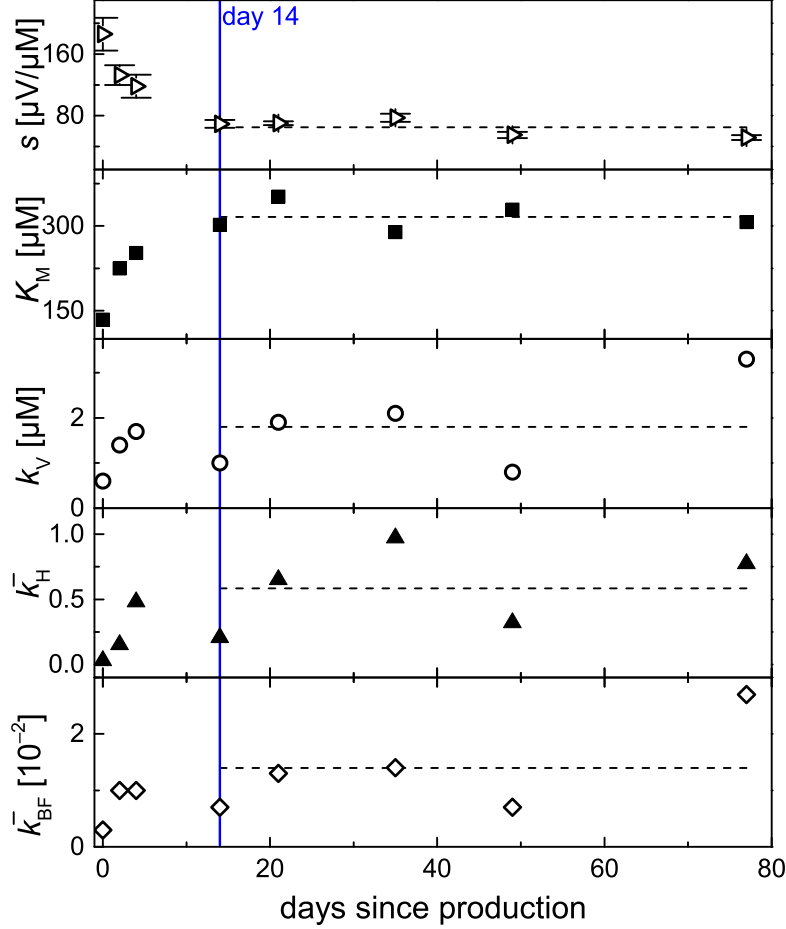


*Figure* 4.8 *Evolution of the sensitivity s with its standard deviation derived by the linear fit of the sensitive region and the extracted model parameters for the AcFET response curves shown in Figure 4.7. The dashed lines indicate the mean value of the respective model parameter as discussed in the text.*

On the basis of the results in this subsection one can draw the conclusion that the employed AcFET preparation is reproducible. Further, the analysis of the AcFET stability revealed that AcFETs partially denaturate within the first two weeks after preparation while from day 14 on stable response curves are obtained over the course of 63 days.

### 4.2.2 Comparison to the Case of Penicillinase

The utilization of the *kinetic model* allows a direct comparison of PenFETs and AcFETs on a quantitative basis. For that purpose the response curve of a freshly prepared AcFET and an aged AcFET (response curves after day 0 and day 14 in Figure 4.7) are exemplarily compared to the response curve of a PenFET (response curve at a pH of 7 in Figure 4.5). As it is evident from Figure 4.9 all three response curves can be clearly distinguished.
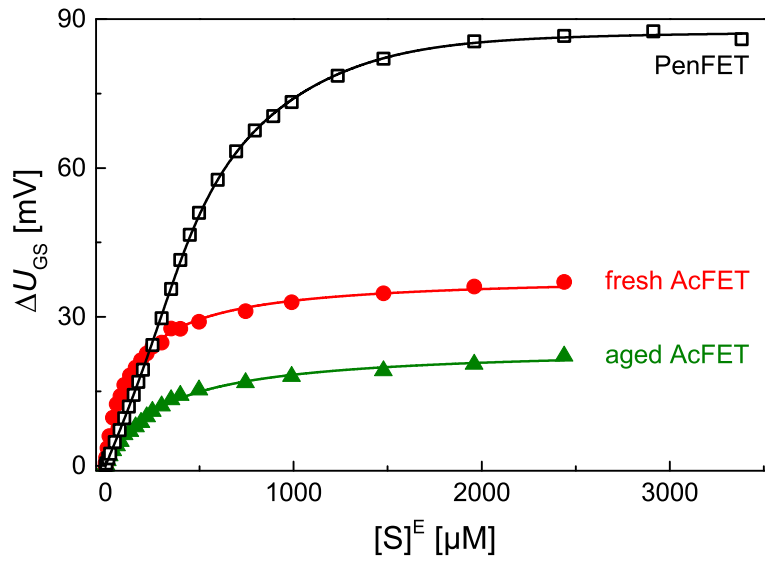


*Figure* 4.9 *Comparison of PenFET from Figure 4.5 with a freshly prepared AcFET and an aged AcFET (14 days old) from Figure 4.7. Solid lines represent fits.*

The sensitivities of the AcFETs and the PenFET were determined up to $[S]^E = 100\,\mu M$ and $[S]^E = 500\,\mu M$, respectively. With a value of $s = (186 \pm 21)\,\mu V\,\mu M^{-1}$, the freshly prepared AcFET has the highest sensitivity of all three response curves, followed by the sensitivity of the PenFET $((104 \pm 1)\,\mu V\,\mu M^{-1})$. The aged AcFET exhibits the lowest sensitivity of $(69 \pm 5)\,\mu V\,\mu M^{-1}$. As the sensitivity of the device is directly related to the velocity of the enzymatic reaction $v \sim k_2/K_M$ (for $[S] \to 0$) [88, 89], the ratio of $k_2$ to $K_M$ is a good measure for estimating the relative sensitivities. With a value of $2.00 \cdot 10^8\,M^{-1}\,s^{-1}$ [121] $k_2/K_M$ is an order of magnitude higher for AChE than for penicillinase $(0.28 \cdot 10^8\,M^{-1}\,s^{-1}$ [122]). Thus, it is expected that the sensitivity of an AcFET should be higher than that of a PenFET. For the aged AcFET this statement does not hold indicating that partial denaturation

of AChE could be responsible for the decrease in sensitivity, confirming the conclusion in subsection 4.2.1.

The difference between the AcFET and the PenFET response curves is even more pronounced when the height of the saturation signal is evaluated: With a value of about $85\,\mathrm{mV}$ the saturation signal of the PenFET is approximately 2.5 times and 4 times higher than the saturation signal of the freshly prepared AcFET and the aged AcFET, respectively.

Out of the four model parameters, only $k_V$, $\bar{k}_H$ and $\bar{k}_{BF}$ are affecting the saturation signal. An increase in $\bar{k}_H$ and $\bar{k}_{BF}$ as well as a decrease in $k_V$ results in a decrease of the saturation signal (cf. Figure 2.9). Since $k_V$, $\bar{k}_H$ and $\bar{k}_{BF}$ are all smaller for an AcFET than for a PenFET (cf. Table 4.5), $\bar{k}_H$ and $\bar{k}_{BF}$ cannot be responsible for the observed difference in the saturation signal. Hence, the difference in the saturation signals is mainly caused by the parameter $k_V$. As $k_V = k_2 \cdot [\mathrm{E}]_0 / k_S$, the smaller $k_V$ of an AcFET in comparison to a PenFET can be attributed to a lower density of enzymes on the gate area $[\mathrm{E}]_0$ or/and in $k_2$ as well as to an increase of the substrate molecule transport rate constant $k_S$. The value $k_2$ for penicillinase and fresh AChE can be estimated using the ratio $k_2 / K_M$ for AChE and penicillinase as stated above and the values for $K_M$ as deduced with the *kinetic model* (cf. Table 4.5). Consequently, $k_2$ can be

*Table* 4.5 *Extracted model parameters for the comparison of a PenFET, a freshly prepared AcFET and an aged AcFET shown in Figure 4.9.*

|  | $K_M$ [μM] | $k_V$ [μM] | $\bar{k}_H$ | $\bar{k}_{BF}$ |
|---|---|---|---|---|
| PenFET | 72 | 1565 | 143 | 1.84 |
| fresh AcFET | 134 | 0.6 | 0.029 | 0.003 |
| aged AcFET | 302 | 1.0 | 0.205 | 0.007 |

estimated to be $2.0 \cdot 10^3\,\mathrm{s}^{-1}$ for the discussed PenFET and $26.8 \cdot 10^3\,\mathrm{s}^{-1}$ for the freshly prepared AcFET. Accordingly, the value $k_2$ cannot be responsible for the small $k_V$ of an AcFET in comparison to a PenFET.

With the geometrical dimensions of the AChE tetramer being ($42\,\mathrm{nm}$ × $26\,\mathrm{nm}$ × $39\,\mathrm{nm}$) [120] and of the penicillinase dimer being ($8\,\mathrm{nm}$ × $9\,\mathrm{nm}$ × $8\,\mathrm{nm}$) [123], a single AChE molecule occupies approximately 37 times more space than a penicillinase molecule. Hence, on a transistor with a constant gate area, as it is the case here, it is expected that a (sub-)monolayer of enzyme contains significantly less enzymes in case of AChE. Hence, the enzyme density $[\mathrm{E}]_0$ for an AcFET is smaller than for a PenFET if the same

transistor geometry is used.

The substrate transport rate constant $k_S$ is affected by the difference in the substrate concentrations between the gate surface and the surrounding electrolyte. Due to the high conversion efficiency of AChE the difference in substrate concentration for an AcFET is greater than for a PenFET, leading also to a higher $k_S$. Hence, the comparatively small $k_V$ value of an AcFET is due to the lower density of the enzyme layer as well as a larger difference in the substrate concentrations.

Overall the comparison of the AcFET and PenFET response curves showed that the decreased sensitivity of aged AcFETs compared to freshly prepared AcFETs is due to partial denaturation of AChE and that the lower saturation signal of AcFETs is a result of the lower AChE density on the gate area.

## 4.3 Monitoring of Neuronal Activity

In this chapter experiments which monitor neuronal activity *in situ* by means of detecting the release of the neurotransmitter ACh are discussed. For those experiments a reliable and thoroughly characterized ACh sensing devices, whose detection limit can be exceeded by the amount of ACh released by stimulated neurons, is needed.

As ATCh is equivalently processed by AChE as the neurotransmitter ACh [111], the quantitative analysis conducted on AcFETs in the previous section 4.2 with regard to their reproducibility and stability indicates that AcFETs based on GaN-capped AlGaN/GaN SGFETs are suitable for this application. Furthermore, these measurements have shown that AlGaN/GaN-based AcFETs have a detection limit of $1\,\mu M$ which is sufficient to detect ACh released by stimulated neurons (cf. section 2.3).

In addition to the analysis in section 4.2, reference measurements have to be carried out to exclude that the AcFETs show any interfering response with the chemicals used for the experiments discussed in this section. Following the reference measurements in subsection 4.3.1, experiments monitoring neuronal activity are discussed on three different biological samples: myenteric neurons still embedded in the *muscularis propria*, isolated myenteric neurons and coeliac ganglia.

## 4.3.1 Reference Measurements

The reference measurements covered in this subsection are conducted to determine whether the used chemicals fulfill their expected function without compromising the AcFET response to ACh released by the stimulated neurons. The used chemicals are KCl (stimulant used for neuronal membrane depolarization), donepezil (reversible AChE blocker) and ATCh (analog of the neurotransmitter ACh).

The first reference measurement shown in Figure 4.10 is a concentration re-
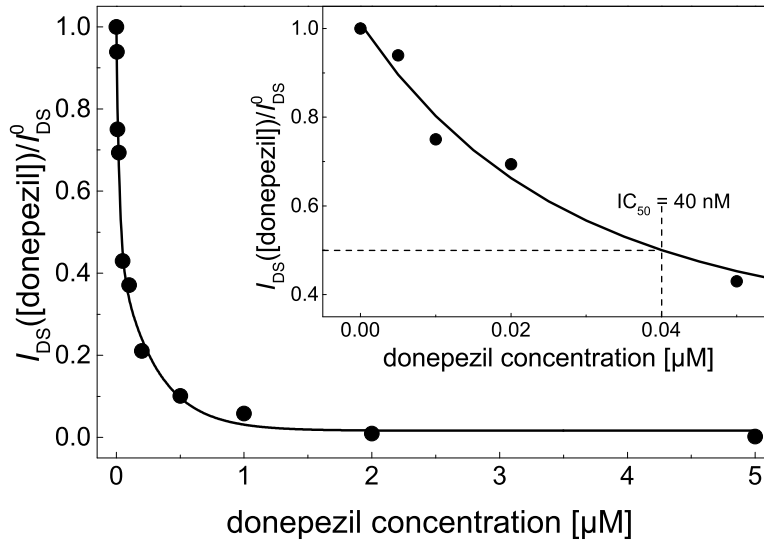


*Figure* 4.10 *Concentration response curve of donepezil. The inset shows an enlargement of the region up to a donepezil concentration of* 55 *nM.*

sponse curve of an AcFET to the reversible AChE blocker donepezil. By means of this measurement one can determine whether the covalently immobilized AChE can be blocked by donepezil in an equal fashion as *in vitro*. The concentration response curve was obtained by plotting $I_{DS}([\text{donepezil}]/I_{DS}^0$ against the administered donepezil concentration. Thereby, $I_{DS}^0$ represents the increase in $I_{DS}$ due to the addition of $200\,\mu$M ATCh while $I_{DS}([\text{donepezil}]$ represents the $I_{DS}$ value obtained after the addition of a given donepezil concentration. To deduce the half maximal inhibitory concentration ($IC_{50}$) the data points were fitted by a double exponential decay fit with the formula $f(x) = 0.55 \cdot \exp(-x/0.02) + 0.44 \cdot \exp(-x/0.29) + 0.02$ to obtain a guide to the eye. Thus, an $IC_{50}$ value of $40\,$nM could be determined as shown in the inset in Figure 4.10. This value is comparable to $IC_{50} = 45\,$nM determined *in vitro* for

donepezil on the example of AChE from *electrophorus electricus* in reference
[124]. Hence, donepezil is an appropriate reversible AChE blocker for AChE
covalently immobilized on AlGaN/GaN SGFETs.

In the following, the effect of the addition of KCl, ATCh and donepezil on
the $I_{DS}$ transient of an AcFET was investigated (cf. Figure 4.11). The addition of the stimulant KCl causes an immediate spike in $I_{DS}$ attributed to an
inhomogeneity in the ionic concentrations. However, this inhomogeneity does
not influence $I_{DS}$ permanently as is evident from the solid line in Figure 4.11.
Subsequently, ATCh, the analog of the neurotransmitter ACh, was added in a
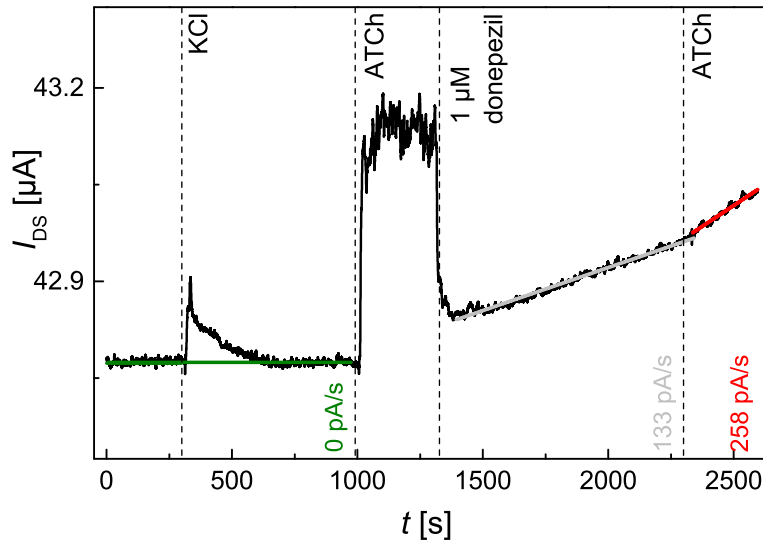


*Figure* 4.11 *Response of an AcFET to the addition of KCl, ATCh and donepezil.*

concentration of 200 µM. The enzymatic conversion of ATCh into acetic acid
and thiocholine lowers the pH and thus increases $I_{DS}$ until a steady state is
reached which corresponds here to an increase of about 400 nA. The following
addition of donepezil in a concentration of 1 µM results in a decrease of $I_{DS}$
as the acid production is immediately reduced. Nevertheless, donepezil is a
reversible AChE blocker, *id est*, acetic acid is still produced in small quantities. This leads to a continuous increase in $I_{DS}$ illustrated by the gray line in
Figure 4.11 which represents a slope of the $I_{DS}$ transient of 133 pA s$^{-1}$.

Finally, ATCh is added a second time resulting in an evident increase in the
slope of the $I_{DS}$ transient by about a factor of two indicated by the red line
in Figure 4.11. The reason for this behavior is a re-enhanced production of

acetic acid which is due to the increased concentration of ATCh, simultaneously demonstrating that the AcFET is still functional.

A third reference measurement was performed to investigate the device selectivity. Therefore, isolated myenteric neurons from (4 - 12) days old Wistar rats were cultivated on oxidized GaN-capped AlGaN/GaN FETs without AChE attached. As the solid line in Figure 4.12 demonstrates the stimulation of the neurons with KCl does not affect the $I_{DS}$ transient apart from the initial spike in $I_{DS}$ due to a temporary inhomogeneity in the ionic concentrations. The
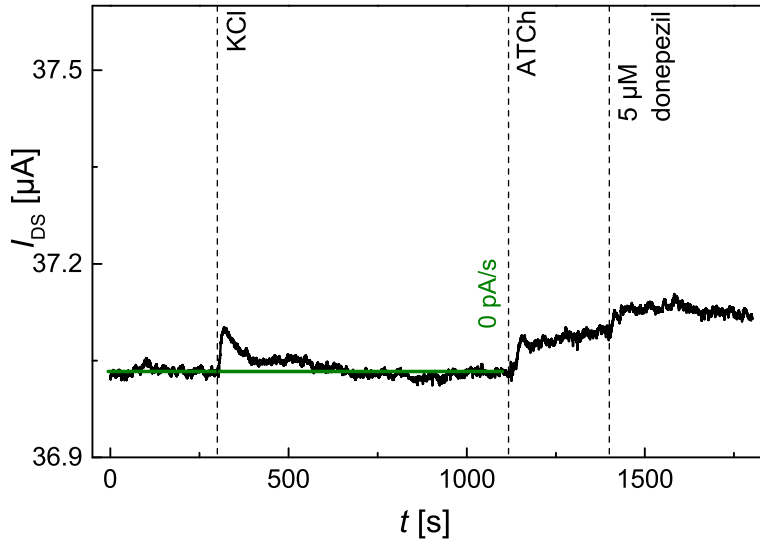


*Figure 4.12 Response of an oxidized FET without AChE covered with isolated myenteric neurons from (4 - 12) days old Wistar rats to the addition of KCl, ATCh and donepezil plotted on the same $I_{DS}$ scale as Figure 4.11 for better comparison.*

following addition of ATCh ([ATCh]= 200 μM) resulted in a steplike increase in $I_{DS}$ by 40 nA which is attributed to AChEs expressed by the neurons covering the AcFET's gate. As this step height is an order of magnitude smaller than the step height of 400 nA in Figure 4.11, one can conclude that covalently immobilized AChE is essential to obtain a significant response of the AcFET proving the selectivity of the device.

Subsequent addition of donepezil in a concentration of 5 μM leads to no obvious change in the $I_{DS}$ transient although one would have expected a blockade of the increase in $I_{DS}$ due to the addition of ATCh as occurring in Figure 4.11. A possible explanation might be the expression of butyrylcholinesterase which is not affected by donepezil as AChE. Thus, ACh would be further enzymati-

cally processed.

In summary, the reference measurements have shown that donepezil blocks covalently immobilized AChE in an equal fashion as *in vitro* while neither donepezil and KCl nor the stimulated myenteric neurons cultivated on the gate area lead to a permanent AcFET response.

### 4.3.2 Myenteric Plexus

The first measurement of neuronal activity was conducted on a piece of *muscularis propria* embedding myenteric neurons from the myenteric plexus which covered an AcFET gate area as it is shown in the inset of Figure 4.13. For this purpose, the tissue sample was obtained from adult Wistar rats according to the procedure described in section 3.3.

As it is possible to deduce from the orange line in Figure 4.13, the AcFET response to the addition of the stimulant KCl differs from the reference measurements displayed in Figures 4.11 and 4.12. In Figure 4.13, stimulation of



*Figure* 4.13 *Monitoring of neuronal activity of myenteric neurons from the myenteric plexus still embedded in the muscularis propria from adult Wistar rats covering the gate area of an AcFET. The inset illustrates the placement of the muscularis propria on the gate area.*

neurons leads to an increase in $I_{DS}$ over time that ensues approximately 300 s

after the addition of KCl and exhibits a slope of $124\,\mathrm{pA\,s^{-1}}$. The delayed onset of the increase in $I_{\mathrm{DS}}$ is due to the fact that 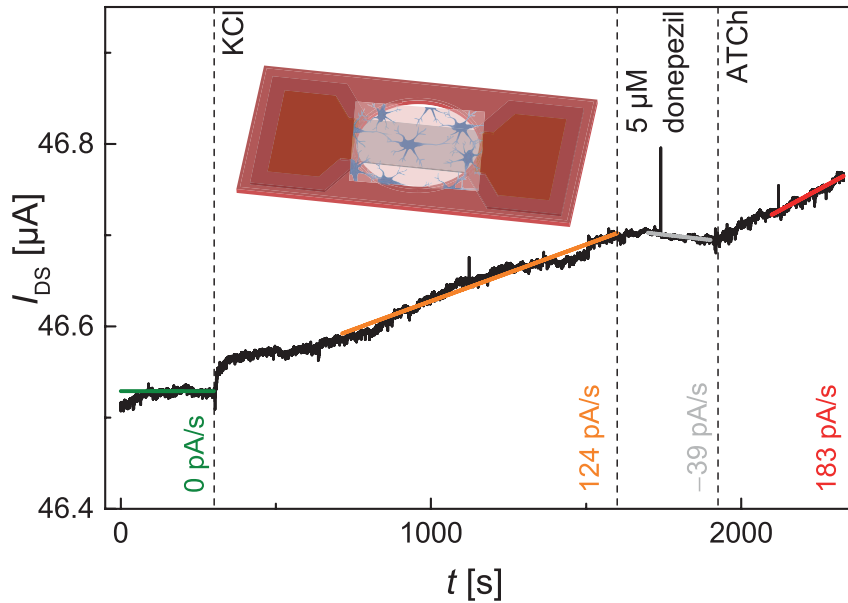ACh has to reach the covalently immobilized AChE on the gate surface and then has to exceed the AcFET's detection limit to evoke a signal. The increase in $I_{\mathrm{DS}}$ itself results from a continuous decrease in pH that is attributed to acetic acid produced by the enzymatic conversion of ACh.

Furthermore, it should be noted that the initial spike in $I_{\mathrm{DS}}$ after the addition of KCl which could be observed in both reference measurements in Figures 4.11 and 4.12 is not visible here. This observation can be explained by the fact that the tissue sample of the *muscularis propria* covers the entire gate area, thus building a diffusion barrier. Hence, the transient inhomogeneity in the ionic concentrations, being responsible for the temporary spike in $I_{\mathrm{DS}}$, has dissipated before it can be registered on the gate surface.

In response to the addition of donepezil in a concentration of $5\,\mathrm{\mu M}$ the slope of the $I_{\mathrm{DS}}$ transient decreases to $-39\,\mathrm{pA\,s^{-1}}$ (cf. gray line in Figure 4.13), similar to the value before stimulation. This observation is comparable to the behavior observed in the reference measurement in Figure 4.11 after addition of donepezil. *Id est*, the decrease of the slope of the $I_{\mathrm{DS}}$ transient is due to the fact that ACh released by the stimulated neurons is no longer enzymatically split and thus the pH not lowered further due to the lack of acetic acid being produced. Hence, the increase in $I_{\mathrm{DS}}$ observed after KCl addition has to be due to the AcFET sensing ACh.

The subsequent addition of ATCh and its correlated increase in the slope of the $I_{\mathrm{DS}}$ transient represented by the red line in Figure 4.13 ($183\,\mathrm{pA\,s^{-1}}$) confirm the AcFET functionality throughout the experiment.

After the experiment the vitality of the tissue sample was tested pharmacologically. To achieve this goal, the piece of *muscularis propria* was removed from the AcFET and prepared for fluorometric calcium imaging utilizing fura-2 acetoxymethylester as described in subsection 3.5.1. Then, the tissue sample was placed in the experimental chamber on an inverted microscope and covered with Tyrode's solution. The fura-2 ratio of several regions of interest with an area comparable to the size of one cell was measured continuously while nicotine and CPA were added in concentrations of $100\,\mathrm{\mu M}$ and $50\,\mathrm{\mu M}$, respectively (for details see subsection 3.5.1). As it is evident from the result shown in Figure 4.14a) the addition of nicotine and CPA both lead to an increase in the fura-2 ratio, *id est* an increase in the cytosolic $Ca^{2+}$-concentration.

Nicotine activates nAChRs and leads to a depolarization of the cell membrane that opens Ca$_V$ channels enabling a Ca$^{2+}$-influx [93]. As the longitudinal muscle layer of the intestine is made up of smooth muscle cells [125] which are deprived of nAChRs [126], the increase in the fura-2 ratio due to nicotine should be referring to a neuronal response.



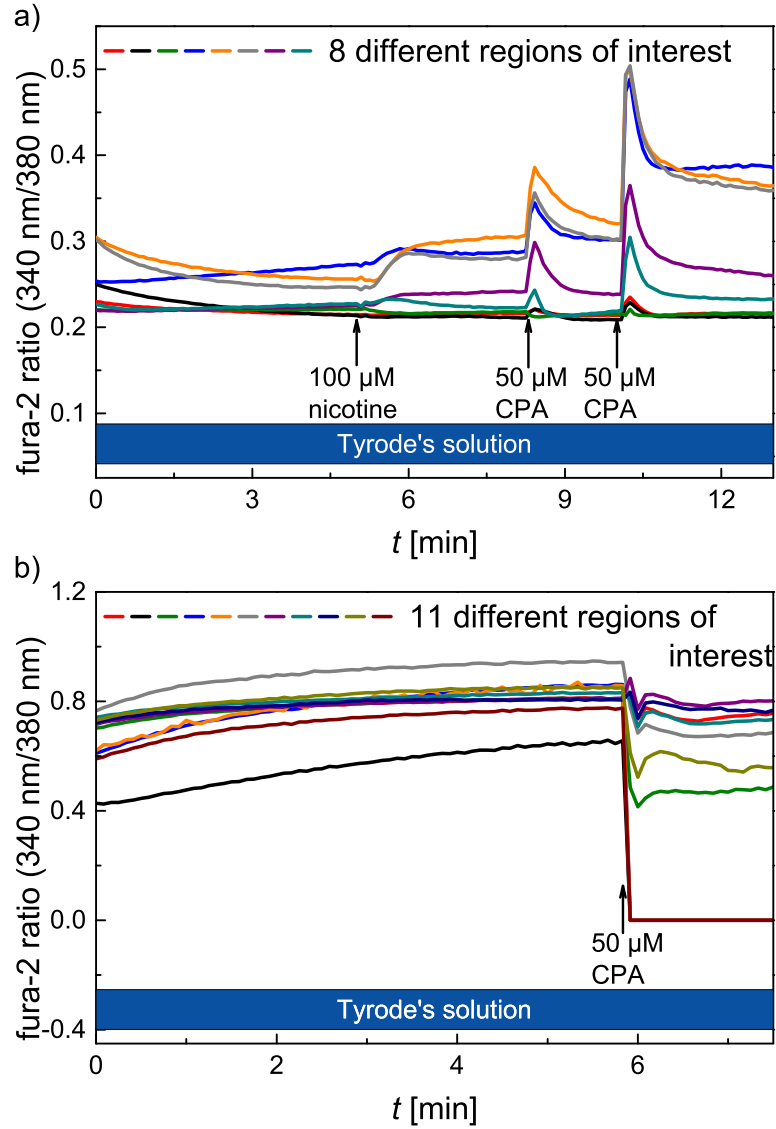*Figure* 4.14 *Transients of the fura-2 ratio signal with a) additions of nicotine in a concentration of 100 μM as well as CPA in a concentration of 50 μM and b) single addition of CPA in a concentration of 50 μM for assessing the vitality of the tissue sample. The tissue sample tested is in each case a piece of muscularis propria after it had been measured following the protocol utilized to obtain Figure 4.13.*

In contrast, the addition of CPA does not allow differentiation between neurons and myocytes as CPA blocks the enzyme $Ca^{2+}$ ATPase inhibiting $Ca^{2+}$-storage in the endoplasmatic reticulum. Thus the cytosolic $Ca^{2+}$-concentration rises in both cell types and so does the fura-2 ratio [127].

Both effects can only be observed in vital cells. Hence, the results shown in Figure 4.14a) prove that the myenteric neurons (by means of nicotine and CPA) as well as the myocytes (by means of CPA) embedded in the *muscularis propria* were vital while the myenteric neuronal activity was monitored with an AcFET.

The vitality of the tissue sample can as well be assessed if it is only treated with CPA as shown in Figure 4.14b). Here, the addition of CPA leads to a distinct decrease in the fura-2 ratio as a result of a shift of the region of interest, due to a sudden contraction of the cells as the contraction trigger $Ca^{2+}$ accumulates within the cytosol [125]. As the muscle contraction indicates vital myocytes it is reasonable to assume that the myenteric neurons embedded in this muscle layer have been vital as well throughout the experiment monitoring their activity with an AcFET. All those results lead to the conclusion that it was possible to realize a neuron/AcFET hybrid.

## 4.3.3 Isolated Myenteric Neurons

After the successful monitoring of myenteric neuronal activity of neurons embedded in the *muscularis propria*, the method was tested for isolated myenteric neurons, from (4 - 12) days old Wistar rats (cf. Figure 3.9B), cultured on the gate area according to the method described in section 3.3. The result is depicted in Figure 4.15.

Similarly to the case of myenteric neurons embedded in the *muscularis propria*, the $I_{DS}$ transient starts to increase over time after the addition of KCl. However, the responses differ with regard to the magnitude of the resulting slope ($618\,\mathrm{pA\,s^{-1}}$ compared to $124\,\mathrm{pA\,s^{-1}}$), its onset (about $100\,\mathrm{s}$ earlier) and the immediate response to the addition of KCl (spike observed).

As the isolated neurons do not completely cover the gate area, part of the gate is in direct contact with the electrolyte. Hence, the AcFET records the transient inhomogeneity in the ionic concentrations explaining the spike observed in $I_{DS}$ after the addition of KCl. Additionally, the isolated neurons are no longer embedded in the *muscularis propria*, which all analytes would have

to permeate before they can reach the gate surface. Thus, released ACh can reach the AcFET surface more easily as reflected by the higher slope of the $I_{DS}$ transient.

The difference of about $100\,\mathrm{s}$ in the onset of the slopes can be explained in terms of a detection limit that has to be reached before a signal is evoked. By comparing the sensitivities of a fresh AcFET and an aged AcFET as discussed in subsection 4.2.1 it is reasonable to assume that the detection limit of an aged AcFET with a sensitivity of $(69 \pm 5)\,\mathrm{\mu V\,\mu M^{-1}}$ is $5\,\mathrm{\mu M}$. Taking the device's transconductance of $60\,\mathrm{\mu S}$ into account, it follows that $I_{DS}$ has to increase by $20\,\mathrm{nA}$ over its baseline value before a slope becomes detectable. Thus, for a slope of $618\,\mathrm{pA\,s^{-1}}$ as in case of isolated myenteric neurons the onset is expected after $32\,\mathrm{s}$, while the onset of the slope should ensue after $161\,\mathrm{s}$ for neurons embedded in the *muscularis propria* (slope of $124\,\mathrm{pA\,s^{-1}}$). In
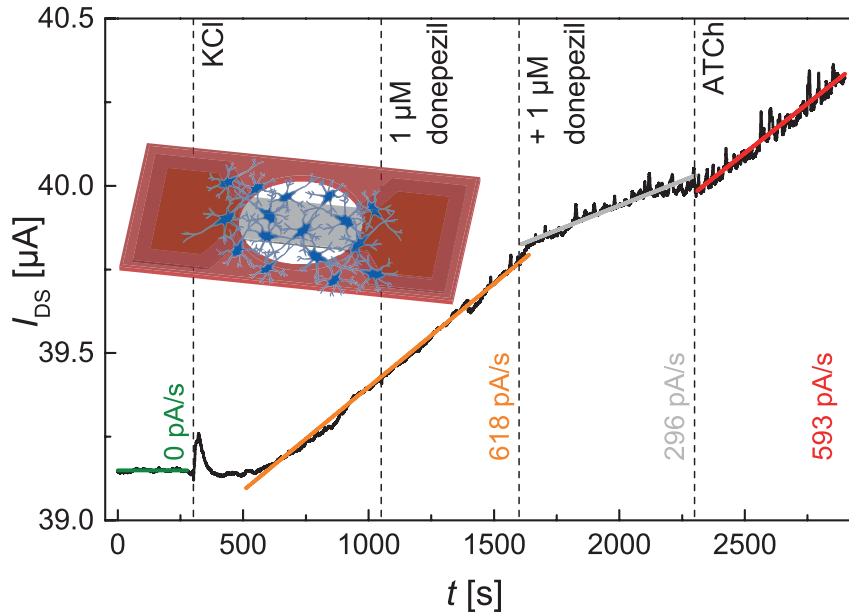


*Figure* 4.15 *Monitoring of neuronal activity of isolated myenteric neurons, from (4 - 12) days old Wistar rats, cultured on the gate area of an AcFET. The placement of the isolated myenteric neurons on the gate is shown in the inset.*

addition, the released ACh needs time to diffuse from the biological sample to the AcFET's gate surface. As this time span should be similar in both cases the expected time difference is in good agreement with the experimental result. The subsequent addition of donepezil in a concentration of $1\,\mathrm{\mu M}$ does not result in a decrease of the slope of the $I_{DS}$ transient. Only a second addition of

donepezil, resulting in a total concentration of $2\,\mu M$, yields a reduction of the slope by about a factor of 2, from $618\,\mathrm{pA\,s^{-1}}$ (cf. orange line in Figure 4.15) to $296\,\mathrm{pA\,s^{-1}}$ (cf. gray line in Figure 4.15), indicating that the enzymatic production of acetic acid is diminished. Hence, the blockade of AChE is not complete. Taking into account that the concentration response curve of an AcFET to donepezil in Figure 4.10 yielded $IC_{50} = 40\,\mathrm{nM}$, this finding illustrates that the donepezil concentration needed to bisect the AChE activity on an AcFET covered with myenteric neurons is about 44 times higher than that of a bare AcFET. This can be explained if AChE is expressed by the isolated neurons and has to be considered in addition to AChE covalently immobilized on the gate area, augmenting the total amount of AChE to be blocked by at least a factor of 44.

Similar to the results in subsections 4.3.1 and 4.3.2, the final addition of ATCh results in a re-increase of the slope of the $I_{\mathrm{DS}}$ transient (compare gray line and red line in Figure 4.15). Hence, the utilized AcFET has been functional throughout the experiment.

A pharmacological vitality test according to the procedure used in subsection 4.3.2 could not be performed on the isolated myenteric neurons cultured on the gate area as the AcFET packaging does not allow sharp focusing of the gate area under the fluorescent microscope. Neither was it possible to remove the isolated neurons non-invasively from the gate area.

For the above mentioned reasons, the vitality of isolated myenteric neurons was tested representatively on capsule-free AcFETs which have been otherwise prepared identically to the method outlined in section 3.2. Consequently, isolated myenteric neurons were cultured on nude AcFETs in the same fashion as on encapsulated AcFETs. However, the missing passivation with silicone rubber did not allow the recording of a measurement similar to the one shown in Figure 4.15. For this reason, the capsule-free AcFET with isolated neurons cultured on the gate area was only submerged in modified Tyrode's solution while KCl, donepezil and ATCh were added in a similar fashion used to obtain Figure 4.15. Afterwards, the sample was treated with propidium iodide and immunostained with the microtubule-associated protein 2 (MAP2) antibody - mouse monoclonal anti-MAP2 - according to the protocol described in subsection 3.5.2.

The primary antibody mouse monoclonal anti-MAP2 serves as a neuronal marker as it specifically labels MAP2 which is highly concentrated in dendrites

of neurons [114]. Subsequent treatment with the secondary antibody Alexa-488-donkey anti-mouse IgG, which binds to the primary antibody mouse monoclonal anti-MAP2, yields a green fluorescence marking neurons especially in the edge area as can be seen in Figure 4.16a). In contrast, red fluorescent propidium iodide stains the nucleus of dead cells [128]. As Figure 4.16b) does not show any distinct circular areas that are fluorescing red, especially within the areas immunostained with mouse monoclonal anti-MAP2 (cf. Figure 4.16c)), it follows that the myenteric neurons pictured have been vital.

As the isolated myenteric neurons used for the vitality test were treated similarly to the ones used for experiments monitoring neuronal activity, it is reasonable to assume that the isolated neurons used to obtain Figure 4.15 have been vital throughout the experiment. Another indication for the validity of this statement is the similarity of the measurement results in Figure 4.13 and Figure 4.15 as the vitality of the myenteric neurons embedded in *muscularis propria* was shown on the actual tissue sample measured.
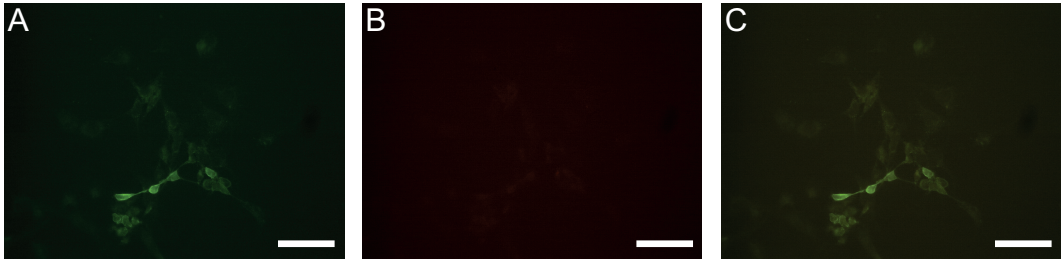


*Figure* 4.16 *Digital images of the fluorescence of isolated myenteric neurons immunostained with primary antibody mouse monoclonal anti-MAP2 in combination with green fluorescent secondary antibody Alexa-488-donkey anti-mouse IgG (green, a)) and stained with propidium iodide (red, b)). c) shows the superposition of both images. The scale bar is equivalent to 100 μm. The fluorescent (immuno-)staining of isolated myenteric neurons was carried out after they had been subjected to conditions mimicking the protocol used to obtain Figure 4.15 to assess their vitality.*

Compared to the case of myenteric neurons embedded in the *muscularis propria* (cf. subsection 4.3.2) the results in this subsection allow the conclusion that a neuron/transistor hybrid could be realized as well with isolated myenteric neurons. The observed steeper slope of the $I_{DS}$ as well as its earlier onset could be attributed to the fact, that the isolated myenteric neurons are no longer embedded *muscularis propria* which builds a diffusion barrier.

## 4.3.4 Coeliac Ganglia

A third experiment monitoring neuronal activity was conducted on coeliac ganglia from adult Wistar rats according to the procedure describe in section 3.3. One of the coeliac ganglia was then placed on the gate area of an AcFET as shown in Figure 3.9C.

The subsequent measurement depicted in Figure 4.17 qualitatively shows the same results as discussed in the two previous subsections: Addition of the stimulant KCl does not lead to a detectable spike in the $I_{DS}$ transient but induces an increase in $I_{DS}$ over time represented by a slope of $395\,\mathrm{pA\,s^{-1}}$ indicated by the orange line. A subsequent addition of donepezil leads to a decrease in the slope by about a factor of 2.3 while the addition of ATCh and the ensuing re-increase of the slope demonstrates the incessant functionality of the AcFET.
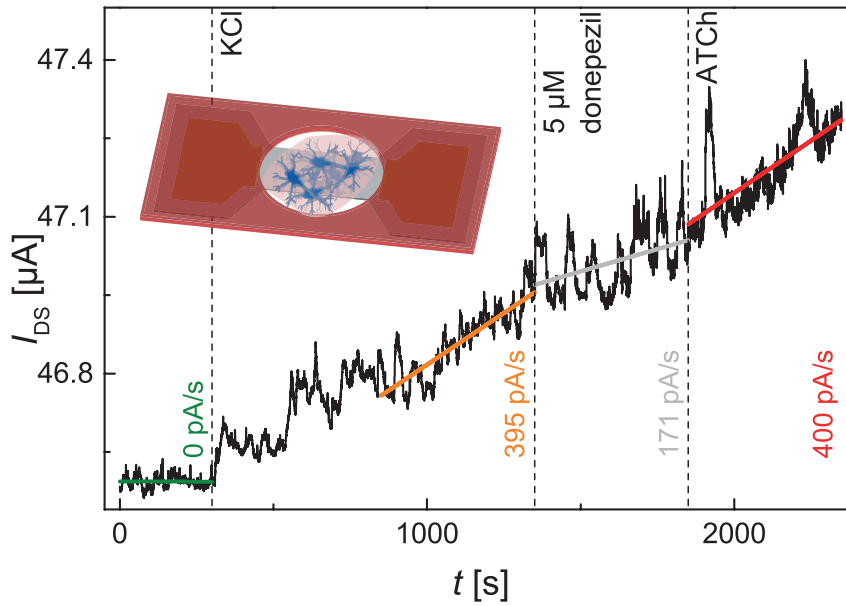


*Figure* 4.17 *Monitoring of neuronal activity of a coeliac ganglion from adult Wistar rats placed on the gate area of an AcFET. The inset shows the placement of the coeliac ganglion the gate area of the AcFET.*

As a coeliac ganglion is an irregularly shaped mass of nerve tissue with a diameter of about $1\,\mathrm{mm}$ they form a diffusion barrier in front of the gate similar to the case of neurons embedded in the *muscularis propria*. Hence, transient inhomogeneities in the ionic concentrations cannot be registered by the AcFET and no spike in $I_{DS}$ is observed in response to KCl addition. Another reason for the spike in $I_{DS}$ not being detectable might be the increased noise level of

the $I_{DS}$ transient after the addition of KCl. The cause for the increased noise level is unknown but might be related to disturbances in the electric field close to the gate surface due to the stimulated neurons. That an increased noise level was not observed in the experiments discussed in the previous subsections might be caused by the lower density of neurons on the gate area in case of isolated myenteric neurons and neurons still embedded in the *muscularis propria*.

The KCl induced increase in $I_{DS}$ over time which is diminished by the addition of donepezil proves that the measured increase in the $I_{DS}$ transient is correlated to AcFET's detection of ACh released by the KCl-stimulated coeliac ganglion. However, the addition of donepezil in a concentration of $5\,\mu M$ does not result in a complete blockade of AChE. The observed slope of the $I_{DS}$ transient (cf. gray line in Figure 4.17) resembles the feature of the $I_{DS}$ transient after the second addition of donepezil in Figure 4.15 attributed to the sum of AChE expressed by the neurons and AChE immobilized on the gate area. Based on the reasonable assumption that neurons within a coeliac ganglion express more AChE than myenteric neurons to control possible neurotransmitter spillover, this would explain the remaining slope of the $I_{DS}$ transient even if donepezil is added in a concentration of $5\,\mu M$.

The nature of the coeliac ganglia does not allow to perform any of the vitality test used in subsections 4.3.2 and 4.3.3. However, all measurements monitoring neuronal activity discussed in section 4.3 show qualitatively comparable results. Thus, the vitality of the coeliac ganglion during the measurement has been assumed without any vitality tests conducted.

In summary, the results presented in this subsection demonstrate the successful realization of a neuron/AcFET hybrid on a third a example - the coeliac ganglion.

# 5 Summary and Conclusion

In the present work, AlGaN/GaN PenFETs and AcFETs were successfully prepared by covalent immobilization of a (sub-)monolayer of the respective enzyme, penicillinase or acetylcholinesterase, via silanization with APTES and crosslinking with glutaraldehyde. The success of the silanization was investigated in detail on the basis of XPS measurements showing a sub-monolayer coverage of up to 88.2%.

The *kinetic model* by Glab *et al.* [49] was proven to be a suitable tool for the quantitative analysis of EnFET response curves, even allowing a quantification of the differences in the response curves of AcFETs and PenFETs. Further, the prepared AcFETs were successfully used to monitor neuronal activity via the detection of the neurotransmitter ACh on three different biological samples.

The applicability of the *kinetic model* was proven on the example of a PenFET measured in electrolytes with buffer concentrations varied over one order of magnitude from $0.5\,\text{mM}$ to $5\,\text{mM}$. Here, the PenFET response curves showed excellent agreement with the fits according to the *kinetic model* as it was evident from the fit quality parameter $\Phi < 0.01$. Further, the change in buffer concentration did only affect the model parameters $\bar{k}_\text{H}$ and $\bar{k}_\text{BF}$ related to the buffer system as one would expect when solely changing the buffer concentration.

In the following, the *kinetic model* was used to assess the reproducibility and stability of the PenFETs. The preparation method used for the covalent immobilization of penicillinase was demonstrated to be reproducible as it was evident from the comparable model parameters $K_\text{M}$, $k_\text{V}$, $\bar{k}_\text{H}$ and $\bar{k}_\text{BF}$.

Analysis of the PenFET stability at pH 7 revealed that PenFET response curves could be measured over the course of $252\,\text{days}$. Within the first $9\,\text{days}$ (first four measurements) the saturation signal decreased by approximately 25% while the sensitive region remained almost unchanged. The simultaneous decrease in $k_\text{V}$ and increase in $\bar{k}_\text{H}$ while $\bar{k}_\text{BF}$ and $K_\text{M}$ remained constant

leads to the conclusion that this behavior can be attributed to the detachment of physisorbed penicillinase. From day 9 (4th measurement) to day 42 (8th measurement) stable response curves were obtained with an average $K_M$ of $(67 \pm 10)\,\mu M$ while from day 56 (9th measurement) the slope of the sensitive region and the height of the saturation signal were diminished over the course of the next 126 days. Then, from day 182 (13th measurement) stable response curves were obtained. Associated with this change in the PenFET response curves from day 56 to day 182 was an increase of all four model parameters $K_M$, $k_V$, $\bar{k}_H$ and $\bar{k}_{BF}$ which could be attributed to the partial denaturation of the enzyme penicillinase.

Measuring the PenFET response curves in dependence of pH showed that the saturation signal decreased while the sensitive region remained unaffected when the pH was changed from 8 to 7. As the model parameters were not significantly affected by this pH-change, the observed decrease in the saturation signal could be attributed to an attenuated dissociation of penicilloic acid, the product of the enzymatic degradation of benzylpenicillin. However, the *kinetic model* could not be applied to response curves at pH 6 as the substrate benzylpenicillin is not only enzymatically but as well protolytically degraded at this pH.

In case of AcFETs, analysis with the *kinetic model* showed that the utilized preparation method yields reproducible response curves with a detection limit of $1\,\mu M$. Further, the evaluation of AcFET response curves at pH 7.5 could be conducted over the course of 77 days. Within the first two weeks (first four measurements), the height of the saturation signal and the slope of the sensitive region, *id est* the sensitivity $s$, were decreased by approximately 50% and 35%, respectively, while from day 14 (4th measurement) on stable response curves were obtained. This development was accompanied by an increase in all four model parameters; *exempli gratia* $K_M$ increased from $134\,\mu M$ on day 0 (1st measurement) to $(316 \pm 20)\,\mu M$ from day 14 (4th measurement) on. Those findings allowed the conclusion that the enzyme AChE is partially denaturated within the first two weeks of storage.

The subsequent comparison of the response curves of a PenFET, a freshly prepared AcFET and a 14 days old AcFET showed that the freshly prepared AcFET exhibited the highest sensitivity $s = (186 \pm 21)\,\mu V\,\mu M^{-1}$ compared to the PenFET $((104 \pm 1)\,\mu V\,\mu M^{-1})$ and the aged AcFET $((69 \pm 5)\,\mu V\,\mu M^{-1})$. Furthermore, the PenFET exhibited a saturation signal of about $85\,mV$ which

was approximately 2.5 times and 4 times higher than the saturation signal of the freshly prepared AcFET and the aged AcFET, respectively. The extracted model parameters $k_V$, $\bar{k}_H$ and $\bar{k}_{BF}$ were all smaller than 1 and generally three orders of magnitude smaller in case of the AcFETs. In contrast the values for $K_M$, $72\,\mu M$ for the PenFET, $134\,\mu M$ for the freshly prepared AcFET and $302\,\mu M$ for the aged AcFET, only differed by a maximum factor of 4.2. Contemplating as well the size of the enzymes and their respective $k_2/K_M$ ratio, one could conclude that the enzyme layer on AcFETs is thinner than on Pen-FETs and that the difference in the substrate concentrations between the gate surface and the surrounding electrolyte is larger for AcFETs. Further, the comparison of a freshly prepared AcFET and an aged AcFET with a PenFET could verify the conclusion that the change of the AcFET response curves within the first two weeks of storage is due to partial denaturation.

Despite the observed partial denaturation of AcFETs, they could be used successfully for monitoring neuronal activity *in situ*, thus realizing a neuron/AcFET hybrid. The three biological samples investigated were: myenteric neurons still embedded in the *muscularis propria* and a coeliac ganglion from adult Wistar rats as well as isolated myenteric neurons from (4 - 12) days old Wistar rats. Thereby, the measured increase in the slope of the $I_{DS}$ transient in response to a KCl stimulus could be attributed to the AcFET sensing ACh released by the stimulated neurons by using the reversible AChE blocker donepezil. However, the donepezil concentrations needed to block the signal evoked by the KCl stimulus were more than five times higher than the concentration of $1\,\mu M$ expected from its concentration response curve. As the concentration response curve of donepezil yielded an $IC_{50}$ value of $45\,nM$ for an AcFET which is comparable to values obtained for AChE from *electrophorus electricus in vitro*, this result is attributed to AChE expressed by the neurons which have to be blocked in addition to AChE covalently immobilized on the AcFET gate area.

Moreover, it was shown that the onset of the slope of the $I_{DS}$ transient in response to a KCl stimulus is correlated to the ACh detection limit of an aged AcFET ($5\,\mu M$). *Id est*, the more ACh reaches the gate surface per second, synonymous with a steeper slope of the $I_{DS}$ transient, the faster the detection limit is surpassed resulting in an earlier onset of the slope.

Vitality of the biological samples throughout the experiments was shown pharmacologically with fluorometric calcium imaging in case of the myenteric plexus

and by immunostaining with the neuronal marker anti-MAP2 in case of the isolated myenteric neurons. The vitality of the coeliac ganglion was deduced from the qualitative comparability of all experiments monitoring neuronal activity.

In conclusion, the *kinetic model* by Glab *et al.* [49] was proven to be an excellent tool for the quantitative analysis of EnFETs with regard to reproducibility, stability and changing measurement conditions. However, it was also shown that the applicability of this *kinetic model* reaches its limits if a second degradation pathway besides the enzymatic one is introduced by the measurement conditions. Further, the successful application of the *kinetic model* to response curves of AcFETs and PenFETs indicates that AlGaN/GaN SGFETs in conjunction with the preparation method used in this work present a promising platform for methodic quantitative analysis of covalently immobilized enzyme layers. The only requirements being that the enzymatic reaction of the immobilized enzyme does affect the pH and that the enzyme layer is thin enough to not be limited by diffusion processes.

The use of thus characterized AcFETs for monitoring neuronal activity of three different biological samples demonstrates expansively the successful realization of a neuron/AcFET hybrid as well as the ability of AcFETs to detect ACh *in situ*. As the AcFETs detection limit of $1\,\mu M$ corresponds to approximately $10\,amol$ in the enzyme layer, those experiments display that further developed AcFETs with an improved sensitivity, *id est* a lower detection limit, might be used complementary to established ACh detection methods sensitive in the (sub-)nmol-range.

Further developed AcFETs might as well be used for detecting the release of ACh by non-neuronal tissue, thus being of value for studying the non-cholinergic system. Within this context one can also envision microarrays consisting of multiple, individually controllable AcFETs which enable the localized detection of the release of the neurotransmitter ACh. The main advantages of AcFETs being their applicability *in situ* and their time resolution on the sub-second scale.

# 6 Outlook

A possible starting point for the improvement of EnFETs based on AlGaN/GaN SGFETs is the replacement of the wet-chemical oxidation by the deposition of a uniform oxide layer which should improve the homogeneity of the APTES layer and thus increase the density of covalently immobilized enzymes.

As the transconductance of a SGFET decreases with increasing thickness of the oxide layer, *id est* the 2DEG is buried deeper underneath the gate surface, one requirement for the deposition method is the ability to control the thickness of the oxide layer. In addition, the deposition method has to introduce a density of active hydroxyl groups on the oxide surface that ensures a high and reproducible pH-sensitivity (cf. section 2.1). A deposition method that meets those requirements is atomic layer deposition (ALD).

For the preliminary experiments shown in this chapter the used oxide was $Al_2O_3$ which was chosen for its known pH-sensitivity [129] and stability in aqueous environments. The deposition of the $2\,nm$ thick $Al_2O_3$ layer was performed with a R-200 ALD system from Picosun (Espoo, Finland) in 20 ALD cycles at a temperature of $250\,°C$. Water and trimethylaluminum were used as precursors with pulse times of $0.1\,s$ and purge times of $15\,s$ and $10\,s$, respectively. Besides this alteration the preparation of those so-called ALD-PenFETs was carried out according to the procedure described in section 3.2.

Comparison of the transconductance and the pH-sensitivity of ALD-PenFETs and PenFETs showed no measurable difference, while the drift of ALD-PenFETs ($0.1\,\mu V\,s^{-1}$ to $3\,\mu V\,s^{-1}$) is lower and varies over a smaller range than the drift of wet-chemically oxidized PenFETs ($0.1\,\mu V\,s^{-1}$ to $50\,\mu V\,s^{-1}$). The lower drift of ALD-PenFETs is illustrated in Figure 6.1 by means of the $\Delta U_{GS}$ transients. The ALD-PenFET exhibits a drift of $0.5\,\mu V\,s^{-1}$ while the PenFET exhibits a drift of $5.2\,\mu V\,s^{-1}$ as represented by the dotted lines in the inset of Figure 6.1. For the illustration of the differences in the response curves of ALD-PenFETs and PenFETs, the response curves of a freshly prepared PenFET and a freshly

prepared ALD-PenFET (day 0 after production) as well as of a nine days old PenFET and a nine days old ALD-PenFET are shown in Figure 6.2. Day 9 after the production was chosen as from this day on reproducible response curves are obtained (cf. section 4.1).
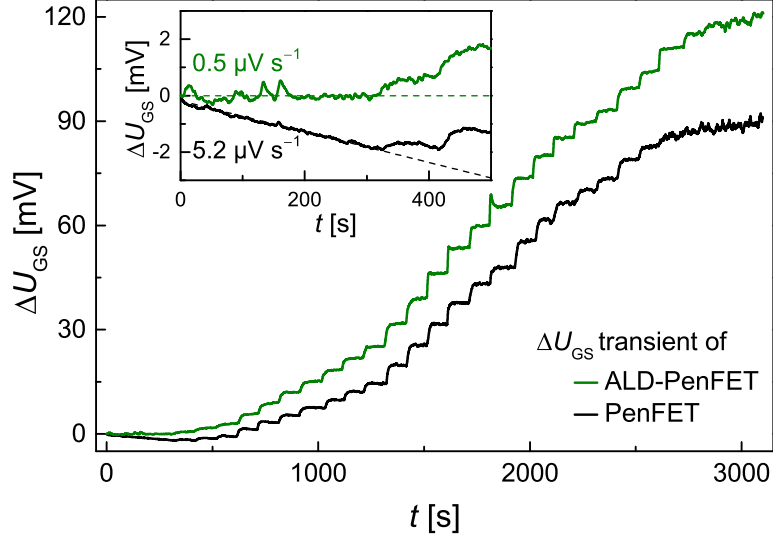


*Figure* 6.1 *Comparison of the transient behavior of a PenFET (black line) and an ALD-PenFET (green line). The inset shows the first 500 s with the drift indicated by the dotted lines.*

On day 0, the response curves of the ALD-PenFET and the PenFET differ in the sensitive region, in the transition region and in the saturation region (cf. Figure 2.9): The sensitivity of the freshly prepared ALD-PenFET determined up to $[S]^E = 500\,\mu M$ is $(135 \pm 1)\,\mu V\,\mu M^{-1}$ and thus 15% higher than the sensitivity of the freshly prepared PenFET $((117 \pm 1)\,\mu V\,\mu M^{-1})$. The transition region and the saturation region of the ALD-PenFET are both shifted towards higher values of $[S]^E$ and the saturation of the ALD-PenFET response cannot be observed using the standard measurement protocol.

This shift of the transition region and the saturation region can also be observed after nine days although the sensitivity of the ALD-PenFET $((102 \pm 3)\,\mu V\,\mu M^{-1})$ is then lower than the PenFET's sensitivity of $(110 \pm 1)\,\mu V\,\mu M^{-1}$. The height of the saturation signal is decreased by 25% for the ALD-PenFET and by 15% for the PenFETs.

Taking into account that the height of the saturation signal is associated with the density of immobilized enzyme $[E]_0$ (cf. subsections 4.1.2 and 4.2.2), those results indicate that $[E]_0$ decrease for both PenFETs during the first nine days

of storage due to the detachment of physisorbed penicillinase, although $[E]_0$ is always higher for ALD-PenFETs than for PenFETs.

For a better understanding of the changes observed in the ALD-PenFET response curves a quantitative analysis with the *kinetic model* would be needed. However, this was not possible as the transition region as well as the saturation region were shifted to higher values of $[S]^E$, and saturation was not reached. Thus, the utilized standard measurement protocol could not provide sufficient data points in those regions which is crucial for obtaining fits with a fit quality parameters $\Phi$ smaller than 0.01.
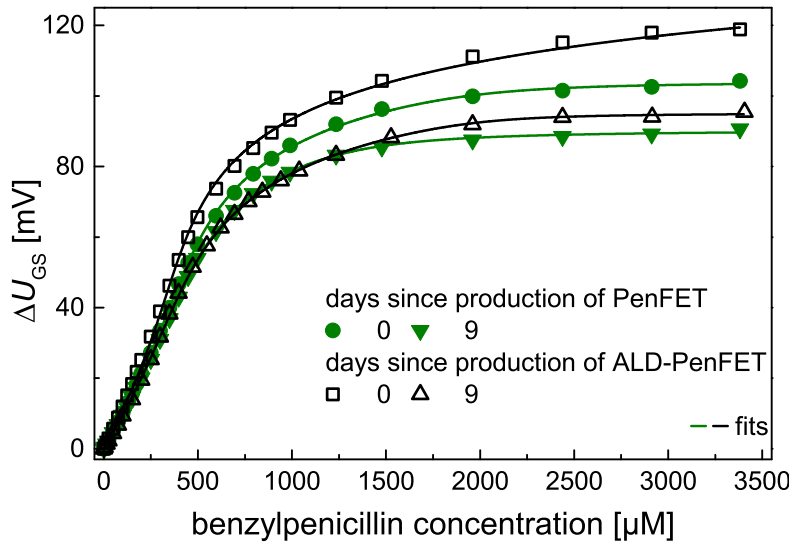


*Figure* 6.2 *Comparison of the response curves of a PenFET (closed symbols) and an ALD-PenFET (open symbols) measured at day 0 and at day 9 after production. The response curves of the PenFET are taken from Figure 4.3 depicting the chronological development of the PenFET response curves.*

Nevertheless, the preliminary results discussed in this chapter illustrate that the replacement of the wet-chemical oxidation by ALD deposition of a 2 nm thick $Al_2O_3$ layer is a promising approach for the improvement of EnFETs based on AlGaN/GaN SGFETs.

# A  Silanization with APTES

- Cleaning step in acetone and isopropyl alcohol for 2 min each at 80% (384 W) in an ultrasonic bath
    - Dry under nitrogen flow
- Mix sulfuric acid (98%) and hydrogen peroxide (30%) in a ratio 3:1
    - Use 5 ml of sulfuric acid and 1.6 ml of hydrogen peroxide per transistor
    - Use 10 ml of sulfuric acid and 3.3 ml of hydrogen peroxide per GaN sample
    - Add hydrogen peroxide last and ensure good mixing by stirring
    - Oxidize samples for 20 min
- Wash samples extensively in bidestilled water
    - Dry under nitrogen flow
    - Dry in a desiccator for at least 2 h 30 min

    - Put samples into Teflon sieve
    - Set temperature of ultrasonic bath to 49.5 °C (via continuous-flow water heater/chiller)
- Prepare 20 mM APTES solution with 120 ml anhydrous toluene and 562 µl APTES (≥98%) in a reactor
- Give samples in reactor and close with glass lid
    - Seal thoroughly with Parafilm
    - Silanize in an ultrasonic bath for 90 min at 90% (432 W)
    - Temperature should not rise above 50 °C; control regularly
- Leave samples in the reactor in the ultrasonic bath for 60 min after silanization
    - Continuous-flow water heater/chiller at 5 °C
- Take samples out of the reactor but leave them in the Teflon sieve and pre-rinse them with anhydrous toluene

85

- Cleaning step in anhydrous toluene for 15 min at 60% (288 W) in an ultrasonic bath
- Pre-rinse samples with isopropyl alcohol
- Cleaning step in isopropyl alcohol for 15 min at 80% (384 W) in an ultrasonic bath
- Pre-rinse samples with diluted acetic acid (pH = 4)
  - 50 µl acetic acid (4 %vol.) in 50 ml bidestilled water
- Cleaning step in diluted acetic acid for 30 min at 10% (48 W) in an ultrasonic bath
- Rinse samples extensively with bidestilled water
  - Dry samples under nitrogen flow
  - Store samples light protected in a desiccator

# B Immobilization of Enzymes

## B.1 Penicillinase

- Use transistors silanized with APTES dried in a desiccator for at least 12 h
- Prepare 20 mM gultaraldehyde solution with 20 ml bidestilled water and 72.7 µl glutaraldehyde (50%) in 50 ml beaker to treat four transistors
  - Incubate transistors for 1 h at room temperature
- Rinse transistors extensively with bidestilled water
  - Dry transistors under nitrogen flow
  - Do not blow dry the gate directly

- Prepare 800 nM penicillinase solution with 224 µg penicillinase from *bacillus cereus* and 1 ml cyanoborohydride coupling buffer
  - Vortex solution for homogeneity
- Place one 100 µl droplet of the 800 nM penicillinase solution on each transistor gate
  - Incubate transistors for 1 h at room temperature

- Pre-rinse transistors with 10 mM phosphate buffered saline (PBS) solution (pH 7)
- Cleaning step in 10 mM PBS solution (pH 7) for 10 min at 40% (192 W) in an ultrasonic bath
  - Continuous-flow water heater/chiller at 5 °C
- Store transistors light protected in 10 mM PBS solution (pH 7) in 50 ml beakers at 5 °C

## B.2 Acetylcholinesterase

- Use transistors silanized with APTES dried in a desiccator for at least 12 h
- Prepare 20 mM gultaraldehyde solution with 20 ml bidestilled water and 72.7 µl glutaraldehyde (50%) in 50 ml beaker to treat four transistors
  - ◦ Incubate transistors for 1 h at room temperature
- Rinse transistors extensively with bidestilled water
  - ◦ Dry transistors under nitrogen flow
  - ◦ Do not blow dry the gate directly

- Prepare 400 nM AChE solution with 187 µg AChE from *electrophorus electricus* and 1 ml cyanoborohydride coupling buffer
  - ◦ Vortex solution for homogeneity
- Place AcFETs in a Petri dish with bidestilled water covering the bottom
- Place one 100 µl droplet of the 400 nM AChE solution on each transistor gate
- Seal the Petri dish with Parafilm
  - ◦ Incubate transistors for 20 h at 5 °C in a humid controlled environment

- Pre-rinse transistors with 10 mM PBS solution (pH 7.5)
- Cleaning step in 10 mM PBS solution (pH 7.5) for 10 min at 40% (192 W) in an ultrasonic bath
  - ◦ Continuous-flow water heater/chiller at 5 °C
- Store transistors light protected in 10 mM PBS solution (pH 7.5) in 50 ml beakers at 5 °C

# C Buffer Solutions

## C.1 Phosphate Buffered Saline Solution

Weigh out the following salt quantities:

| | |
|---|---|
| 4.09 g NaCl | (>99.8%; Carl Roth, Karlsruhe, Germany) |
| 0.72 g $Na_2HPO_4$ | (≥99.5%; Carl Roth, Karlsruhe, Germany) |
| 0.12 g $KH_2PO_4$ | (≥98%; Carl Roth, Karlsruhe, Germany) |
| 0.10 g KCl | (≥99%; Carl Roth, Karlsruhe, Germany) |

Add the weighed out salts to a 500 ml graduated flask and fill to the mark with bidestilled water to obtain a 10 mM PBS solution with a NaCl concentration of 137 mM and a KCl concentration of 2.7 mM. Adjust pH with sodium hydroxide and hydrochloric acid.

For a 0.5 mM PBS solution with a NaCl concentration of 25 mM and a KCl concentration of 0.1 mM add 50 ml 10 mM PBS solution and 1.06 g NaCl to a 1000 ml graduated flask and fill to the mark with bidestilled water. Adjust pH with sodium hydroxide and hydrochloric acid.

## C.2 Tyrode's Solution

Weigh out the following quantities:

| | |
|---|---|
| 4.09 g NaCl | (>99.8%; Carl Roth, Karlsruhe, Germany) |
| 1.92 g HEPES | (≥99.5%; Carl Roth, Karlsruhe, Germany) |
| 0.20 g KCl | (≥99%; Carl Roth, Karlsruhe, Germany) |
| 1.10 g glucose | (≥99.5%; Carl Roth, Karlsruhe, Germany) |

Add the weighed out substances as well as 0.5 ml of 1.25 M $CaCl_2$ solution (from $CaCl_2$*$2H_2O$; ≥99%; Merck Millipore, Darmstadt, Germany) and 0.5 ml of 1.00 M $MgCl_2$ solution (from $MgCl_2$*$6H_2O$; ≥99%; Merck Millipore, Darmstadt, Germany) to a 500 ml graduated flask and fill to the mark with bidestilled water to obtain Tyrode's solution. The concentrations of the respective

ingredients are: 140 mM (NaCl), 10 mM (HEPES), 5,4 mM (KCl), 12.2 mM (glucose), 1.25 mM ($CaCl_2$) and 1.00 mM ($MgCl_2$). Adjust pH with sodium hydroxide and hydrochloric acid.

## C.3 Modified Tyrode's Solution

Weigh out the following quantities:

| | |
|---|---|
| 8.18 g NaCl | (>99.8%; Carl Roth, Karlsruhe, Germany) |
| 0.29 g $Na_2HPO_4$ | (≥99.5%; Carl Roth, Karlsruhe, Germany) |
| 0.03 g $NaH_2PO_4$ | (≥98%; Carl Roth, Karlsruhe, Germany) |
| 0.40 g KCl | (≥99%; Carl Roth, Karlsruhe, Germany) |
| 2.20 g glucose | (≥99.5%; Carl Roth, Karlsruhe, Germany) |

Add the weighed out substances as well as 1 ml of 1.25 M $CaCl_2$ solution (from $CaCl_2*2H_2O$; ≥99%; Merck Millipore, Darmstadt, Germany) and 1 ml of 1.00 M $MgCl_2$ solution (from $MgCl_2*6H_2O$; ≥99%; Merck Millipore, Darmstadt, Germany) to a 1000 ml graduated flask and fill to the mark with bidestilled water. The solution is called modified Tyrode's solution. The concentrations of the respective ingredients are: 140 mM (NaCl), 1 mM (phosphate buffer), 5.4 mM (KCl), 12.2 mM (glucose), 1.25 mM ($CaCl_2$) and 1.00 mM ($MgCl_2$). Adjust pH to 7.5 with sodium hydroxide and hydrochloric acid.

## C.4 Parsons' Solution

Weigh out the following quantities:

| | |
|---|---|
| 6.25 g NaCl | (>99.8%; Carl Roth, Karlsruhe, Germany) |
| 2.10 g $NaHCO_3$ | (≥99.5%; Merck Millipore, Darmstadt, Germany) |
| 0.65 g $Na_2HPO_4*12H_2O$ | (≥98.5%; Merck Millipore, Darmstadt, Germany) |
| 0.03 g $NaH_2PO_4*H_2O$ | (≥98%; Merck Millipore, Darmstadt, Germany) |
| 0.34 g KCl | (≥99%; Carl Roth, Karlsruhe, Germany) |
| 2.20 g glucose | (≥99.5%; Carl Roth, Karlsruhe, Germany) |

Add the weighed out substances as well as 1 ml of 1.00 M $MgSO_4$ solution (from $MgSO_4*7H_2O$; ≥99.5%; Merck Millipore, Darmstadt, Germany) to a 1000 ml graduated flask and fill with bidestilled water. Purge solution with a gas mixture of 5 Vol.-% $CO_2$ and 95 Vol.-% $O_2$. When pH is below 7.8

add 1 ml of 1.25 M $CaCl_2$ solution (from $CaCl_2$*$2H_2O$; ≥99%; Merck Millipore, Darmstadt, Germany) and fill the graduated flask to the mark. The solution is called Parsons' solution. The concentrations of the respective ingredients are: 107 mM (NaCl), 25 mM ($NaHCO_3$), 2 mM (phosphate buffer), 4.5 mM (KCl), 12.2 mM (glucose), 1.25 mM ($CaCl_2$) and 1.00 mM ($MgSO_4$). Adjust pH to 7.4 with sodium bicarbonate and hydrochloric acid.

# D Preparation of Biological Samples

All experiments stated in the following chapter were approved by *Regierungspräsidium Gießen*, Gießen, Germany and performed according to the German and European animal welfare law.

## D.1 Myenteric Plexus

- Female and male Wistar rats with a body mass of $(140\text{-}160)\,\mathrm{g}$ are killed by stunning followed by exanguination
- Open abdominal cavity along the *linea alba*
- Remove the colon by severing it at the proximal and distal end
- Rinse the colon with Parson's solution
- Place colon on a plastic rod with a diameter of $5\,\mathrm{mm}$
- Make a circular incision near the anal end with a blunt scalpel
- Remove the *serosa* and *muscularis propria* embedding the myenteric plexus in proximal direction
- Place tissue on a cooled glass plate
- Dissect the distal end of the tissue into small pieces of $(1\,\mathrm{mm} \times 2\,\mathrm{mm})$
- Using fine forceps transfer one piece of tissue onto the gate of an AcFET
  - Cover with polyester gauze (pore size $70\,\mu\mathrm{m}$) and fix with plastic clip
- Transfer AcFETs into a $50\,\mathrm{ml}$ beaker with $37\,°\mathrm{C}$ warm Tyrode's solution for transport

## D.2 Isolated Myenteric Neurons

- (4 - 12) days old Wistar rats are killed by stunning followed by exanguination
- Open abdominal cavity along the *linea alba*
- Sever the intestine at the distal end using a binocular microscope
- Extract intestine up to the cardia minding the mesentery
- Place intestine into $Ca^{2+}$- and $Mg^{2+}$-free Hanks' balanced salt solution (HBSS) supplemented with 1% (v/v) PenStrep
- Cut off and remove colon as well as appendix
- Strip off the *muscularis propria* from the distal end using two fine forceps
- Incubate *muscularis propria* in a $0.5\,mg\,ml^{-1}$ collagenase type II solution at 37 °C for 80 min

- Vortex for (10 - 15) s
- Dilute 1 ml of the tissue-collagenase solution with 1 ml of $Ca^{2+}$- and $Mg^{2+}$-free HBSS supplemented with 1% (v/v) PenStrep
- Distribute this dilution in small Petri dishes in aliquots of 0.5 ml
  - Add 1.5 ml of $Ca^{2+}$- and $Mg^{2+}$-free HBSS supplemented with 1% (v/v) PenStrep to each Petri dish
- Collect the myenteric ganglia forming net-like structures from those dilutions using a binocular microscope and place them into warm Neurobasal medium supplemented with 0.25% (v/v) L-glutamine, 1% (v/v) PenStrep and 10% (v/v) foetal calf serum
  - Repeat this routine until a convenient amount of myenteric ganglia is reached

- To obtain a cell suspension pass the ganglia through a 23G hypodermic needle (0.60 mm × 60 mm) three to five times
- Transfer 20 µl of the cell suspension to the gate of an AcFET
- Place AcFETs in a Petri dish with bidestilled water covering the bottom
  - Cap with another Petri dish

- Incubated AcFETs overnight at 37 °C in an atmosphere of 5% (v/v) $CO_2$ in 95% (v/v) air
- Transfer AcFETs into a 50 ml beaker with 37 °C warm Tyrode's solution for transport

## D.3  Coeliac Ganglia

- Female and male Wistar rats with a body mass of (160 - 220) g are killed by stunning followed by exanguination
- Open abdominal cavity along the *linea alba*
- Make lateral relief incisions
- Move colon, stomach, kidneys, liver and spleen cranialwards to expose the aorta (cf. Figure 3.10)
- Remove fatty tissue around the aorta using fine forceps
  - Remove fluids carefully from tissue and/or organs with delicate task wipes
- Hold coeliac ganglion gingerly with fine forceps and dissect with a sharp scalpel
- Clean coeliac ganglion in Petri dish filled with isotonic 10 mM PBS solution
- Transfer coeliac ganglion onto the gate of an AcFET
  - Cover with polyester gauze (pore size 70 μm) and fix with plastic clip
- Transfer AcFETs into a 50 ml beaker with 37 °C warm Tyrode's solution for transport

# E Viability Assays

## E.1 Myenteric Plexus

This viability test was performed on pieces of the *muscularis propria* after measurements for monitoring of neuronal activity had taken place (cf. section 3.4). After the measurements the pieces of *muscularis propria* covering AcFETs were transported in warm Tyrode's solution from the *I. Physikalisches Institut* to the *Institut für Veterinär-Physiologie und -Biochemie* where the tissue pieces were removed from the AcFETs. Directly after arriving at the *Institut für Veterinär-Physiologie und -Biochemie* the tissue's viability was pharmacologically tested as follows:

- Collect a piece of *muscularis propria* from the gate of an AcFET and place it onto a cover slip ($\varnothing = 13\,\text{mm}$) coated with poly-L-lysine ($M > 300,000\,\text{g}\,\text{mol}^{-1}$)

- Incubate in $(30\text{-}50)\,\mu\text{l}$ Tyrode's solution with $2.5\,\mu\text{mol}\,\text{l}^{-1}$ fura-2 acetoxymethylester and $0.05\,\text{g}\,\text{l}^{-1}$ pluronic acid at $37\,°\text{C}$ for $40\,\text{min}$

- Place the cover slip in an experimental chamber on an inverted microscope equipped with an epifluorescence set-up and an image analysis system

- Top cover slip with $1\,\text{ml}$ of Tyrode's solution

- Select several regions of interest each with the size of a about one cell
  - Sample the change in the fura-2 ratio with a rate of $0.2\,\text{Hz}$
      Fura-2 ratio is defined by dividing the emission value at an excitation wavelength of $340\,\text{nm}$ by the emission value at an excitation wavelength of $380\,\text{nm}$
  - Emission is measured with a sample rate of $0.2\,\text{Hz}$ for wavelengths above $420\,\text{nm}$

- Add $2\,\mu\text{l}$ of $50\,\text{mM}$ nicotine solution to yield a final concentration of $100\,\mu\text{M}$
  - $50\,\text{mM}$ nicotine solution is obtained by dissolving $23.12\,\text{mg}$ nicotine

hydrogen tartrate salt in 1 ml bidestilled water

- After 180 s add 5 µl of 10 mM CPA solution to yield a final concentration of 50 µM
    - ◦ 10 mM CPA solution is obtained by dissolving 0.34 mg CPA in 100 µl DMSO
    - ◦ CPA addition might be repeated or being the only addition made

## E.2  Isolated Myenteric Neurons

Throughout this viability test capsule-free transistors with AChE immobilized on the gate area were used. The isolated neurons were cultured on the gate area of those AcFETs according to appendix D.2. Then they were submitted to the same conditions as during routinely performed measurements for monitoring neuronal activity (cf. section 3.4). Directly thereafter the immunocytochemistry and propidium iodide staining were carried out as follows:

- Rinse the transistors with pre-warmed isotonic 10 mM PBS solution
- Cover the transistors with 300 µM propidium iodide solution for 5 min at 37 °C
    - ◦ 300 µM propidium iodide solution is obtained by dissolving 0.21 mg propidium iodide in 1 ml bidestilled water
- Rinse the transistors with pre-warmed isotonic 10 mM PBS solution
- Fix the cells by covering the transistor with a solution of 4% (w/v) paraformaldehyde and 2% (w/v) saccharose for 5 min at 37 °C
- Stop the fixation by rinsing the transistors covered with cells three times, 5 min each in pre-warmed isotonic 10 mM PBS solution
- Incubate the transistors for 30 min in warm isotonic 10 mM PBS solution containing 0.05% (w/v) Tween 20 for permeabilization and 4% BSA in order to block unspecific bindings
- Siphon the PBS solution
- Incubate the transistors overnight at 4 °C with the primary antibody mouse monoclonal anti-MAP2 (final dilution 1:400) dissolved in isotonic 10 mM PBS solution containing 1% (w/v) BSA, 0.05% (v/v) Tween 20 and 1% (v/v) donkey serum
- To remove unbound primary antibody, rinse the transistors three times,

5 min each in pre-warmed isotonic 10 mM PBS solution

- Incubate the transistors for 1 h at room temperature in the dark with the secondary antibody Alexa-488-donkey anti-mouse IgG (final dilution 1:400) dissolved in isotonic 10 mM PBS solution containing 1% (w/v) BSA and 0.05% (v/v) Tween 20
- Siphon the PBS solution
- Place the transistors on glass slide
- Examine the transistors with a fluorescence microscope using the FITC filter system for Alexa-488 and the CY3 filter system for propidium iodide
  - Neurons fluoresce green
  - Nuclei of dead cells fluoresce red
- Take digital images with a black and white camera using NIS Elements 2.30 software to adjust the color

# Bibliography

[1] D. R. Thévenot, K. Toth, R. A. Durst, and G. S. Wilson, *Electrochemical biosensors: Recommended definitions and classification*, Biosensors and Bioelectronics **16** (2001), 121 – 131, http://dx.doi.org/10.1016/S0956-5663(01)00115-4.

[2] G. M. Müntze, B. Baur, W. Schäfer, A. Sasse, J. Howgate, K. Röth, and M. Eickhoff, *Quantitative analysis of immobilized penicillinase using enzyme-modified AlGaN/GaN field-effect transistors*, Biosensors and Bioelectronics **64** (2015), 605 – 610, http://dx.doi.org/10.1016/j.bios.2014.09.062.

[3] R. Thapa, S. Alur, K. Kim, F. Tong, Y. Sharma, M. Kim, C. Ahyi, J. Dai, J. W. Hong, M. Bozack, J. Williams, A. Son, A. Dabiran, and M. Park, *Biofunctionalized AlGaN/GaN high electron mobility transistor for DNA hybridization detection*, Applied Physics Letters **100** (2012), 232109, http://dx.doi.org/10.1063/1.4727895.

[4] C.-C. Huang, G.-Y. Lee, J.-I. Chyi, H.-T. Cheng, C.-P. Hsu, Y.-R. Hsu, C.-H. Hsu, Y.-F. Huang, Y.-C. Sun, C.-C. Chen, S.-S. Li, J. A. Yeh, D.-J. Yao, F. Ren, and Y.-L. Wang, *AlGaN/GaN high electron mobility transistors for protein-peptide binding affinity study*, Biosensors and Bioelectronics **41** (2013), 717 – 722, http://dx.doi.org/10.1016/j.bios.2012.09.066.

[5] L. C. Clark and C. Lyons, *Electrode systems for continuous monitoring in cardiovascular surgeries*, Annals of the New York Academy of Sciences **102** (1962), 29 – 45, http://dx.doi.org/10.1111/j.1749-6632.1962.tb13623.x.

[6] J. D. Newman and A. P. Turner, *Home blood glucose biosensors: A commercial perspective*, Biosensors and Bioelectronics **20** (2005), 2435 – 2453, http://dx.doi.org/10.1016/j.bios.2004.11.012.

[7] A. P. F. Turner, *Biosensors: Sense and sensibility*, Chemical Society Reviews **42** (2013), 3184 – 3196, `http://dx.doi.org/10.1039/C3CS35528D`.

[8] M. Gebinoga, P. Mai, M. Donahue, M. Kittler, I. Cimalla, B. Lübbers, M. Klett, V. Lebedev, L. Silveira, S. Singh, and A. Schober, *Nerve cell response to inhibitors recorded with an aluminum-galliumnitride/galliumnitride field-effect transistor*, Journal of Neuroscience Methods **206** (2012), 195 – 199, `http://dx.doi.org/10.1016/j.jneumeth.2012.02.018`.

[9] Y.-W. Kang, G.-Y. Lee, J.-I. Chyi, C.-P. Hsu, Y.-R. Hsu, C.-H. Hsu, Y.-F. Huang, Y.-C. Sun, C.-C. Chen, S. C. Hung, F. Ren, J. A. Yeh, and Y.-L. Wang, *Human immunodeficiency virus drug development assisted with AlGaN/GaN high electron mobility transistors and binding-site models*, Applied Physic Letters **102** (2013), 173704, `http://dx.doi.org/10.1063/1.4803916`.

[10] M. S. Makowski, I. Bryan, Z. Sitar, C. Arellano, J. Xie, R. Collazo, and A. Ivanisevic, *Kinase detection with gallium nitride based high electron mobility transistors*, Applied Physics Letters **103** (2013), 013701, `http://dx.doi.org/10.1063/1.4812987`.

[11] S. Chen, M. Svedendahl, R. P. V. Duyne, and M. Käll, *Plasmon-enhanced colorimetric ELISA with single molecule sensitivity*, Nano Letters **11** (2011), 1826 – 1830, `http://dx.doi.org/10.1021/nl2006092`.

[12] X. Zhang, X. Ma, F. Dou, P. Zhao, and H. Liu, *A biosensor based on metallic photonic crystals for the detection of specific bioreactions*, Advanced Functional Materials **21** (2011), 4219 – 4227, `http://dx.doi.org/10.1002/adfm.201101366`.

[13] B. S. Kang, F. Ren, L. Wang, C. Lofton, W. W. Tan, S. J. Pearton, A. Dabiran, A. Osinsky, and P. P. Chow, *Electrical detection of immobilized proteins with ungated AlGaN/GaN high-electron-mobility transistors*, Applied Physic Letters **87** (2005), 023508, `http://dx.doi.org/10.1063/1.1994951`.

[14] S. Andreescu and J.-L. Marty, *Twenty years research in cholinesterase biosensors: From basic research to practical applications*, Biomolecular Engineering **23** (2006), 1 – 15,

`http://dx.doi.org/10.1016/j.bioeng.2006.01.001`.

[15] K. D. Spradling and J. F. D. III, *Chapter three – The molecular toxicology of chemical warfare nerve agents* (Elsevier, 2011).

[16] J. E. Storm, K. K. Rozman, and J. Doull, *Occupational exposure limits for 30 organophosphate pesticides based on inhibition of red blood cell acetylcholinesterase*, Toxicology **150** (2000), $1-29$, `http://dx.doi.org/10.1016/S0300-483X(00)00219-5`.

[17] F. Arduini, S. Guidone, A. Amine, G. Palleschi, and D. Moscone, *Acetylcholinesterase biosensor based on self-assembled monolayer-modified gold-screen printed electrodes for organophosphorus insecticide detection*, Sensors and Actuators B: Chemical **179** (2013), $201-208$, `http://dx.doi.org/10.1016/j.snb.2012.10.016`.

[18] S. V. Dzyadevych, V. N. Arkhypova, C. Martelet, N. Jaffrezic-Renault, J.-M. Chovelon, A. V. El'skaya, and A. P. Soldatkin, *Potentiometric biosensors based on ISFETs and immobilized cholinesterases*, Electroanalysis **16** (2004), 1873–1882, `http://dx.doi.org/10.1002/elan.200403075`.

[19] X. Meng, J. Wei, X. Ren, J. Ren, and F. Tang, *A simple and sensitive fluorescence biosensor for detection of organophosphorus pesticides using $H_2O_2$-sensitive quantum dots/bienzyme*, Biosensors and Bioelectronics **47** (2013), $402-407$, `http://dx.doi.org/10.1016/j.bios.2013.03.053`.

[20] G. Yu, W. Wu, Q. Zhao, X. Wei, and Q. Lu, *Efficient immobilization of acetylcholinesterase onto amino functionalized carbon nanotubes for the fabrication of high sensitive organophosphorus pesticides biosensors*, Biosensors and Bioelectronics **68** (2015), $288-294$, `http://dx.doi.org/10.1016/j.bios.2015.01.005`.

[21] F. Arduini, A. Amine, D. Moscone, and G. Palleschi, *Biosensors based on cholinesterase inhibition for insecticides, nerve agents and aflatoxin B1 detection (review)*, Microchimica Acta **170** (2010), $193-214$, `http://dx.doi.org/10.1007/s00604-010-0317-1`.

[22] Y. Ikarashi, Y. Harigaya, Y. Tomidokoro, M. Kanai, M. Ikeda, E. Matsubara, T. Kawarabayashi, H. Kuribara, S. G. Younkin, Y. Maruyama, and M. Shoji, *Decreased level of brain acetylcholine and memory dis-*

*turbance in APPsw mice*, Neurobiology of Aging **25** (2004), 483 – 490, `http://dx.doi.org/10.1016/S0197-4580(03)00122-2`.

[23] B. Dubois, M. Ruberg, F. Javoy-Agid, A. Ploska, and Y. Agid, *A subcortico-cortical cholinergic system is affected in Parkinson's disease*, Brain Research **288** (1983), 213 – 218, `http://dx.doi.org/10.1016/0006-8993(83)90096-3`.

[24] R. Bartus, R. Dean, B. Beer, and A. Lippa, *The cholinergic hypothesis of geriatric memory dysfunction*, Science **217** (1982), 408–414, `http://dx.doi.org/10.1126/science.7046051`.

[25] N. Chauhan and C. Pundir, *Amperometric determination of acetylcholine – A neurotransmitter, by chitosan/gold-coated ferric oxide nanoparticles modified gold electrode*, Biosensors and Bioelectronics **61** (2014), 1 – 8, `http://dx.doi.org/10.1016/j.bios.2014.04.048`.

[26] K. E. White and J. L. Cummings, *Schizophrenia and Alzheimer's disease: Clinical and pathophysiologic analogies*, Comprehensive Psychiatry **37** (1996), 188 – 195, `http://dx.doi.org/10.1016/S0010-440X(96)90035-8`.

[27] K. S. Lips, J. Wunsch, S. Zarghooni, T. Bschleipfer, K. Schukowski, W. Weidner, I. Wessler, U. Schwantes, H. Koepsell, and W. Kummer, *Acetylcholine and molecular components of its synthesis and release machinery in the urothelium*, European Urology **51** (2007), 1042 – 1053, `http://dx.doi.org/10.1016/j.eururo.2006.10.028`.

[28] S. Bader, J. Klein, and M. Diener, *Choline acetyltransferase and organic cation transporters are responsible for synthesis and propionate-induced release of acetylcholine in colon epithelium*, European Journal of Pharmacology **733** (2014), 23 – 33, `http://dx.doi.org/10.1016/j.ejphar.2014.03.036`.

[29] W. Kummer, K. Lips, and U. Pfeil, *The epithelial cholinergic system of the airways*, Histochemistry and Cell Biology **130** (2008), 219 – 234, `http://dx.doi.org/10.1007/s00418-008-0455-2`.

[30] I. Wessler and C. J. Kirkpatrick, *Acetylcholine beyond neurons: The non-neuronal cholinergic system in humans*, British Journal of Pharmacology **154** (2008), 1558 – 1571, `http://dx.doi.org/10.1038/bjp.2008.185`.

[31] T. Huang, L. Yang, J. Gitzen, P. T. Kissinger, M. Vreeke, and A. Heller, *Detection of basal acetylcholine in rat brain microdialysate*, Journal of Chromatography B: Biomedical Sciences and Applications **670** (1995), 323−327, `http://dx.doi.org/10.1016/0378-4347(95)00181-6`.

[32] M. Persike, M. Zimmermann, J. Klein, and M. Karas, *Quantitative determination of acetylcholine and choline in microdialysis samples by MALDI-TOF MS*, Analytical Chemistry **82** (2010), 922−929, `http://dx.doi.org/10.1021/ac902130h`.

[33] P. Uutela, R. Reinilä, P. Piepponen, R. A. Ketola, and R. Kostiainen, *Analysis of acetylcholine and choline in microdialysis samples by liquid chromatography/tandem mass spectrometry*, Rapid Communications in Mass Spectrometry **19** (2005), 2950−2956, `http://dx.doi.org/10.1002/rcm.2160`.

[34] A. Hai, D. Ben-Haim, N. Korbakov, A. Cohen, J. Shappir, R. Oren, M. E. Spira, and S. Yitzchaik, *Acetylcholinesterase-ISFET based system for the detection of acetylcholine and acetylcholinesterase inhibitors*, Biosensors and Bioelectronics **22** (2006), 605−612, `http://dx.doi.org/10.1016/j.bios.2006.01.028`.

[35] J. Wei, J. Ren, J. Liu, X. Meng, X. Ren, Z. Chen, and F. Tang, *An eco-friendly, simple, and sensitive fluorescence biosensor for the detection of choline and acetylcholine based on C-dots and the Fenton reaction*, Biosensors and Bioelectronics **52** (2014), 304−309, `http://dx.doi.org/10.1016/j.bios.2013.09.006`.

[36] K. Ma, L. Lu, Z. Qi, J. Feng, C. Zhuo, and Y. Zhang, *In situ induced metal-enhanced fluorescence: A new strategy for biosensing the total acetylcholinesterase activity in sub-microliter human whole blood*, Biosensors and Bioelectronics **68** (2015), 648−653, `http://dx.doi.org/10.1016/j.bios.2015.01.061`.

[37] L.-G. Zamfir, L. Rotariu, and C. Bala, *Acetylcholinesterase biosensor for carbamate drugs based on tetrathiafulvalene-tetracyanoquinodimethane/ionic liquid conductive gels*, Biosensors and Bioelectronics **46** (2013), 61−67, `http://dx.doi.org/10.1016/j.bios.2013.02.018`.

[38] E. Aynacı, A. Yaşar, and F. Arslan, *An amperometric biosen-*

*sor for acetylcholine determination prepared from acetylcholinesterase-choline oxidase immobilized in polypyrrole-polyvinylsulpfonate film*, Sensors and Actuators B: Chemical **202** (2014), 1028 – 1036, `http://dx.doi.org/10.1016/j.snb.2014.06.049`.

[39] A. Härtl, B. Baur, M. Stutzmann, and J. A. Garrido, *Enzyme-modified field effect transistors based on surface-conductive single-crystalline diamond*, Langmuir **24** (2008), 9898 – 9906, `http://dx.doi.org/10.1021/la8014139`.

[40] A. B. Kharitonov, M. Zayats, A. Lichtenstein, E. Katz, and I. Willner, *Enzyme monolayer-Functionalized field-effect transistors for biosensor applications*, Sensors and Actuators B: Chemical **70** (2000), 222 – 231, `http://dx.doi.org/10.1016/S0925-4005(00)00573-6`.

[41] I.-Y. Sohn, D.-J. Kim, J.-H. Jung, O. J. Yoon, T. N. Thanh, T. T. Quang, and N.-E. Lee, *pH sensing characteristics and biosensing application of solution-gated reduced graphene oxide field-effect transistors*, Biosensors and Bioelectronics **45** (2013), 70 – 76, `http://dx.doi.org/10.1016/j.bios.2013.01.051`.

[42] P. Fromherz, *Semiconductor chips with ion channels, nerve cells and brain*, Physica E: Low-dimensional Systems and Nanostructures **16** (2003), 24 – 34, `http://dx.doi.org/10.1016/S1386-9477(02)00578-7`.

[43] G. Steinhoff, O. Purrucker, M. Tanaka, M. Stutzmann, and M. Eickhoff, $Al_x Ga_{1-x} N$ – *A new material system for biosensors*, Advanced Functional Materials **13** (2003), 841 – 846, `http://dx.doi.org/10.1002/adfm.200304397`.

[44] G. Steinhoff, B. Baur, G. Wrobel, S. Ingebrandt, A. Offenhausser, A. Dadgar, A. Krost, M. Stutzmann, and M. Eickhoff, *Recording of cell action potentials with AlGaN/GaN field-effect transistors*, Applied Physic Letters **86** (2005), 033901–1 – 033901–3, `http://dx.doi.org/10.1063/1.1853531`.

[45] A. Podolska, S. Tham, R. D. Hart, R. M. Seeber, M. Kocan, M. Kocan, U. K. Mishra, K. D. Pfleger, G. Parish, and B. D. Nener, *Biocompatibility of semiconducting AlGaN/GaN material with living cells*, Sensors and Actuators B: Chemical **169** (2012), 401 – 406,

`http://dx.doi.org/10.1016/j.snb.2012.04.015`.

[46] I. Cimalla, F. Will, K. Tonisch, M. Niebelschütz, V. Cimalla, V. Lebedev, G. Kittler, M. Himmerlich, S. Krischok, J. Schaefer, M. Gebinoga, A. Schober, T. Friedrich, and O. Ambacher, *AlGaN/GaN biosensor – Effect of device processing steps on the surface properties and biocompatibility*, Sensors and Actuators B: Chemical **123** (2007), 740 – 748, `http://dx.doi.org/10.1016/j.snb.2006.10.030`.

[47] J. I. Pankove, *Electrolytic etching of GaN*, Journal of The Electrochemical Society **119** (1972), 1118 – 1119, `http://dx.doi.org/10.1149/1.2404410`.

[48] H. P. Maruska and J. J. Tietjen, *The preparation and properties of vapor-deposited single-crystal-line GaN*, Applied Physics Letters **15** (1969), 327 – 329, `http://dx.doi.org/10.1063/1.1652845`.

[49] S. Glab, R. Koncki, and A. Hulanicki, *Kinetic model of pH-based potentiometric enzymic sensors. Part 1. Theoretical considerations*, Analyst **116** (1991), 453 – 458, `http://dx.doi.org/10.1039/AN9911600453`.

[50] S. D. Caras, D. Petelenz, and J. Janata, *pH-based enzyme potentiometric sensors. Part 2. Glucose-sensitive field effect transistor*, Analytical Chemistry **57** (1985), 1920 – 1923, `http://dx.doi.org/10.1021/ac00286a028`.

[51] S. D. Caras and J. Janata, *pH-based enzyme potentiometric sensors. Part 3. Penicillin-sensitive field effect transistor*, Analytical Chemistry **57** (1985), 1924 – 1925, `http://dx.doi.org/10.1021/ac00286a029`.

[52] M. Zayats, A. B. Kharitonov, E. Katz, A. F. Bückmann, and I. Willner, *An integrated NAD+-dependent enzyme-functionalized field-effect transistor (ENFET) system: Development of a lactate biosensor*, Biosensors and Bioelectronics **15** (2000), 671 – 680, `http://dx.doi.org/10.1016/S0956-5663(00)00120-2`.

[53] A. Poghossian, M. J. Schöning, P. Schroth, A. Simonis, and H. Lüth, *An ISFET-based penicillin sensor with high sensitivity, low detection limit and long lifetime*, Sensors and Actuators B: Chemical **76** (2001), 519 – 526, `http://dx.doi.org/10.1016/S0925-4005(01)00609-8`.

[54] D. Pijanowska, M. Dawgul, and W. Torbicz, *Comparison of urea deter-*

*mination in biological samples by Enfets based on pH and pNH$_4$ detection*, Sensors **3** (2003), 160 – 165, `http://dx.doi.org/10.3390/s30600160`.

[55] A. Diallo, L. Djeghlaf, L. Mazenq, J. Launay, W. Sant, and P. Temple-Boyer, *Development of pH-based ElecFET biosensors for lactate ion detection*, Biosensors and Bioelectronics **40** (2013), 291 – 296, `http://dx.doi.org/10.1016/j.bios.2012.07.063`.

[56] W. J. Blaedel, T. R. Kissel, and R. C. Boguslaski, *Kinetic behavior of enzymes immobilized in artificial membranes*, Analytical Chemistry **44** (1972), 2030 – 2037, `http://dx.doi.org/10.1021/ac60320a021`.

[57] P. W. Carr, *Fourier analysis of the transient response of potentiometric enzyme electrodes*, Analytical Chemistry **49** (1977), 799 – 802, `http://dx.doi.org/10.1021/ac50014a032`.

[58] S. D. Caras, J. Janata, D. Saupe, and K. Schmitt, *pH-based enzyme potentiometric sensors. Part 1. Theory*, Analytical Chemistry **57** (1985), 1917 – 1920, `http://dx.doi.org/10.1021/ac00286a027`.

[59] M. Eddowes, *Response of an enzyme-modified pH-sensitive ion-selective device, consideration of the influence of the buffering capacity of the analyte solution*, Sensors and Actuators **7** (1985), 97 – 115, `http://dx.doi.org/10.1016/0250-6874(85)85012-5`.

[60] T. Lei, M. Fanciulli, R. J. Molnar, T. D. Moustakas, R. J. Graham, and J. Scanlon, *Epitaxial growth of zinc blende and wurtzitic gallium nitride thin films on (001) silicon*, Applied Physics Letters **59** (1991), 944 – 946, `http://dx.doi.org/10.1063/1.106309`.

[61] A. Allred, *Electronegativity values from thermochemical data*, Journal of Inorganic and Nuclear Chemistry **17** (1961), 215 – 221, `http://dx.doi.org/10.1016/0022-1902(61)80142-5`.

[62] F. Bernardini, V. Fiorentini, and D. Vanderbilt, *Spontaneous polarization and piezoelectric constants of III-V nitrides*, Physical Review B **56** (1997), R10024 – R10027, `http://dx.doi.org/10.1103/PhysRevB.56.R10024`.

[63] O. Ambacher, J. Smart, J. R. Shealy, N. G. Weimann, K. Chu, M. Murphy, W. J. Schaff, L. F. Eastman, R. Dimitrov, L. Wittmer, M. Stutzmann, W. Rieger, and J. Hilsenbeck, *Two-dimensional electron gases*

*induced by spontaneous and piezoelectric polarization charges in N- and Ga-face AlGaN/GaN heterostructures*, Journal of Applied Physics **85** (1999), 3222 – 3233, `http://dx.doi.org/10.1063/1.369664`.

[64] I. Vurgaftman and J. R. Meyer, *Band parameters for nitrogen-containing semiconductors*, Journal of Applied Physics **94** (2003), 3675 – 3696, `http://dx.doi.org/10.1063/1.1600519`.

[65] D. Brunner, H. Angerer, E. Bustarret, F. Freudenberg, R. Hopler, R. Dimitrov, O. Ambacher, and M. Stutzmann, *Optical constants of epitaxial AlGaN films and their temperature dependence*, Journal of Applied Physics **82** (1997), 5090 – 5096, `http://dx.doi.org/10.1063/1.366309`.

[66] A. Polian, M. Grimsditch, and I. Grzegory, *Elastic constants of gallium nitride*, Journal of Applied Physics **79** (1996), 3343 – 3344, `http://dx.doi.org/10.1063/1.361236`.

[67] A. F. Wright, *Elastic properties of zinc-blende and wurtzite AlN, GaN, and InN*, Journal of Applied Physics **82** (1997), 2833 – 2839, `http://dx.doi.org/10.1063/1.366114`.

[68] O. Ambacher, B. Foutz, J. Smart, J. R. Shealy, N. G. Weimann, K. Chu, M. Murphy, A. J. Sierakowski, W. J. Schaff, L. F. Eastman, and et al., *Two dimensional electron gases induced by spontaneous and piezoelectric polarization in undoped and doped AlGaN/GaN heterostructures*, Journal of Applied Physics **87** (2000), 334 – 344, `http://dx.doi.org/10.1063/1.371866`.

[69] W. Q. Chen and S. K. Hark, *Strain-induced effects in (111)-oriented InAsP/InP, InGaAs/InP, and InGaAs/InAlAs quantum wells on InP substrates*, Journal of Applied Physics **77** (1995), 5747 – 5750, `http://dx.doi.org/10.1063/1.359219`.

[70] I. P. Smorchkova, C. R. Elsass, J. P. Ibbetson, R. Vetury, B. Heying, P. Fini, E. Haus, S. P. DenBaars, J. S. Speck, and U. K. Mishra, *Polarization-induced charge and electron mobility in AlGaN/GaN heterostructures grown by plasma-assisted molecular-beam epitaxy*, Journal of Applied Physics **86** (1999), 4520 – 4526, `http://dx.doi.org/10.1063/1.371396`.

[71] L. Hsu and W. Walukiewicz, *Electron mobility in* $Al_x Ga_{1-x}N/GaN$

*heterostructures*, Physical Review B **56** (1997), 1520 – 1528, http://dx.doi.org/10.1103/PhysRevB.56.1520.

[72] J. Antoszewski, M. Gracey, J. M. Dell, L. Faraone, T. A. Fisher, G. Parish, Y.-F. Wu, and U. K. Mishra, *Scattering mechanisms limiting two-dimensional electron gas mobility in $Al_{0.25}Ga_{0.75}N/GaN$ modulation-doped field-effect transistors*, Journal of Applied Physics **87** (2000), 3900 – 3904, http://dx.doi.org/10.1063/1.372432.

[73] R. Oberhuber, G. Zandler, and P. Vogl, *Mobility of two-dimensional electrons in AlGaN/GaN modulation-doped field-effect transistors*, Applied Physics Letters **73** (1998), 818 – 820, http://dx.doi.org/10.1063/1.122011.

[74] I. P. Smorchkova, L. Chen, T. Mates, L. Shen, S. Heikman, B. Moran, S. Keller, S. P. DenBaars, J. S. Speck, and U. K. Mishra, *AlN/GaN and (Al,Ga)N/AlN/GaN two-dimensional electron gas structures grown by plasma-assisted molecular-beam epitaxy*, Journal of Applied Physics **90** (2001), 5196 – 5201, http://dx.doi.org/10.1063/1.1412273.

[75] S. Elhamri, A. Saxler, W. C. Mitchel, C. R. Elsass, I. P. Smorchkova, B. Heying, E. Haus, P. Fini, J. P. Ibbetson, S. Keller, P. M. Petroff, S. P. DenBaars, U. K. Mishra, and J. S. Speck, *Persistent photoconductivity study in a high mobility AlGaN/GaN heterostructure*, Journal of Applied Physics **88** (2000), 6583 – 6588, http://dx.doi.org/10.1063/1.1322386.

[76] J. Z. Li, J. Y. Lin, H. X. Jiang, M. A. Khan, and Q. Chen, *Persistent photoconductivity in a two-dimensional electron gas system formed by an AlGaN/GaN heterostructure*, Journal of Applied Physics **82** (1997), 1227 – 1230, http://dx.doi.org/10.1063/1.365893.

[77] M. Fagerlind and N. Rorsman, *Illumination effects on electrical characteristics of GaN/AlGaN/GaN heterostructures and heterostructure field effect transistors and their elimination by proper surface passivation*, Journal of Applied Physics **112** (2012), 014511, http://dx.doi.org/10.1063/1.4730782.

[78] X. Z. Dang, C. D. Wang, E. T. Yu, K. S. Boutros, and J. M. Redwing, *Persistent photoconductivity and defect levels in n-type AlGaN/GaN heterostructures*, Applied Physics Letters **72** (1998), 2745 –

2747, `http://dx.doi.org/10.1063/1.121077`.

[79] T. Y. Lin, H. M. Chen, M. S. Tsai, Y. F. Chen, F. F. Fang, C. F. Lin, and G. C. Chi, *Two-dimensional electron gas and persistent photoconductivity in* $Al_xGa_{1-x}N/GaN$ *heterostructures*, Physical Review B **58** (1998), 13793 – 13798, `http://dx.doi.org/10.1103/PhysRevB.58.13793`.

[80] G. Steinhoff, M. Hermann, W. J. Schaff, L. F. Eastman, M. Stutzmann, and M. Eickhoff, *pH response of GaN surfaces and its application for pH-sensitive field-effect transistors*, Applied Physic Letters **83** (2003), 177 – 179, `http://dx.doi.org/10.1063/1.1589188`.

[81] B. Baur, G. Steinhoff, J. Hernando, O. Purrucker, M. Tanaka, B. Nickel, M. Stutzmann, and M. Eickhoff, *Chemical functionalization of GaN and AlN surfaces*, Applied Physic Letters **87** (2005), 263901–1 – 263901–3, `http://dx.doi.org/10.1063/1.2150280`.

[82] D. E. Yates, S. Levine, and T. W. Healy, *Site-binding model of the electrical double layer at the oxide/water interface*, Journal of the Chemical Society, Faraday Transactions 1 **70** (1974), 1807 – 1818, `http://dx.doi.org/10.1039/F19747001807`.

[83] M. Bayer, C. Uhl, and P. Vogl, *Theoretical study of electrolyte gate AlGaN/GaN field effect transistors*, Journal of Applied Physics **97** (2005), 033703, `http://dx.doi.org/10.1063/1.1847730`.

[84] B. Baur, J. Howgate, H.-G. von Ribbeck, Y. Gawlina, V. Bandalo, G. Steinhoff, M. Stutzmann, and M. Eickhoff, *Catalytic activity of enzymes immobilized on AlGaN/GaN solution gate field-effect transistors*, Applied Physic Letters **89** (2006), 183901–1 – 183901–3, `http://dx.doi.org/10.1063/1.2369534`.

[85] G. M. Müntze, E. Pouokam, J. Steidle, W. Schäfer, A. Sasse, K. Röth, M. Diener, and M. Eickhoff, *In situ monitoring of myenteric neuron activity using acetylcholinesterase-modified AlGaN/GaN solution-gate field-effect transistors*, Biosensors and Bioelectronics **77** (2016), 1048 – 1054, `http://dx.doi.org/j.bios.2015.10.076`.

[86] N. Rohrbaugh, I. Bryan, Z. Bryan, R. Collazo, and A. Ivanisevic, *Long-term stability assessment of AlGaN/GaN field effect transistors modified with peptides: Device characteristics vs. surface properties*, AIP Advances **5** (2015), 097102, `http://dx.doi.org/10.1063/1.4930192`.

[87] W. E. Morf, *Theoretical evaluation of the performance of enzyme electrodes and of enzyme reactors*, Microchimica Acta **74** (1980), 317 – 332, `http://dx.doi.org/10.1007/BF01196457`.

[88] L. Michaelis and M. L. Menten, *Die Kinetik der Invertinwirkung*, Biochemische Zeitschrift **49** (1913), 333 – 369.

[89] K. A. Johnson and R. S. Goody, *The original Michaelis constant: Translation of the 1913 Michaelis-Menten paper*, Biochemistry **50** (2011), 8264 – 8269, `http://dx.doi.org/10.1021/bi201284u`.

[90] S. Glab, R. Koncki, and I. Holona, *Kinetic model of pH-based potentiometric enzymic sensors. Part 2. Method of fitting*, Analyst **117** (1992), 1671 – 1674, `http://dx.doi.org/10.1039/AN9921701671`.

[91] S. W. Kuffler and D. Yoshikami, *The number of transmitter molecules in a quantum: an estimate from iontophoretic application of acetylcholine at the neuromuscular synapse*, The Journal of Physiology **251** (1975), 465 – 482, `http://dx.doi.org/10.1113/jphysiol.1975.sp011103`.

[92] A. Draguhn, *Membranpotenzial und Signalübertragung in Zellverbänden*, R. Klinke, H.-C. Pap, A. Kurtz, and S. Silbernagel, editors, *Physiologie*, 6th edition (Thieme, 2009).

[93] M. Heckmann and J. Dudel, *Synaptische Übertragung*, R. F. Schmidt, F. Lang, and M. Heckmann, editors, *Physiologie des Menschen mit Pathophysiologie*, 31st edition (Springer, 2010).

[94] B. Brenner, *Muskulatur*, R. Klinke, H.-C. Pap, A. Kurtz, and S. Silbernagel, editors, *Physiologie*, 6th edition (Thieme, 2009).

[95] S. K. Fisher and J. Wonnacott, *Acetylcholine*, S. T. Brady, G. J. Siegel, R. W. Albers, and D. L. Price, editors, *Basic Neurochemistry - Principles of Molecular, Cellular, and Medical Neurobiology*, 8th edition (Academic Press, 2012).

[96] S. M. Parsons, B. A. Bahr, G. A. Rogers, E. D. Clarkson, K. Noremberg, and B. W. Hicks, *Chapter 20: Acetylcholine transporter – Vesamicol receptor pharmacology and structure*, A. C. Cuello, editor, *Cholinergic function and dysfunction* (Elsevier, 1993).

[97] R. Carin, J. P. Deville, and J. Werckmann, *An XPS study of GaN thin films on GaAs*, Surface and Interface Analysis **16** (1990), 65 – 69,

`http://dx.doi.org/10.1002/sia.740160116`.

[98] D. A. Shirley, *High-resolution X-ray photoemission spectrum of the valence bands of gold*, Physical Review B **5** (1972), 4709 – 4714, `http://dx.doi.org/10.1103/PhysRevB.5.4709`.

[99] A. Arranz, C. Palacio, D. García-Fresnadillo, G. Orellana, A. Navarro, and E. Munñoz, *Influence of surface hydroxylation on 3-aminopropyltriethoxysilane growth mode during chemical functionalization of GaN surfaces: An angle-resolved X-ray photoelectron spectroscopy study*, Langmuir **24** (2008), 8667 – 8671, `http://dx.doi.org/10.1021/la801259n`.

[100] T. Bekkay, E. Sacher, and A. Yelon, *Surface reaction during the argon ion sputter cleaning of surface oxidized crystalline silicon (111)*, Surface Science Letters **217** (1989), L377 – L381, `http://dx.doi.org/10.1016/0167-2584(89)90963-8`.

[101] H. Kim, P. E. Colavita, K. M. Metz, B. M. Nichols, B. Sun, J. Uhlrich, X. Wang, T. F. Kuech, , and R. J. Hamers, *Photochemical functionalization of gallium nitride thin films with molecular and biomolecular layers*, Langmuir **22** (2006), 8121 – 8126, `http://dx.doi.org/10.1021/la0610708`.

[102] P. Zhdan, A. Shepelin, Z. Osipova, and V. Sokolovskii, *The extent of charge localization on oxygen ions and catalytic activity on solid state oxides in allylic oxidation of propylene*, Journal of Catalysis **58** (1979), 8 – 14, `http://dx.doi.org/10.1016/0021-9517(79)90237-9`.

[103] Y.-J. Lin, C.-D. Tsai, Y.-T. Lyu, and C.-T. Lee, *X-ray photoelectron spectroscopy study of $(NH_4)_2S_x$-treated Mg-doped GaN layers*, Applied Physic Letters **77** (2000), 687 – 689, `http://dx.doi.org/10.1063/1.127086`.

[104] K. Bierbaum, M. Kinzler, C. Woell, M. Grunze, G. Haehner, S. Heid, and F. Effenberger, *A near edge X-ray absorption fine structure spectroscopy and X-ray photoelectron spectroscopy study of the film properties of self-assembled monolayers of organosilanes on oxidized Si(100)*, Langmuir **11** (1995), 512 – 518, `http://dx.doi.org/10.1021/la00002a025`.

[105] S. Tanuma, C. J. Powell, and D. R. Penn, *Calculations of electron inelastic mean free paths. V. Data for 14 organic compounds over the 50-2000 eV range*, Surface and Interface Analysis **21** (1994), 165 – 176,

`http://dx.doi.org/10.1002/sia.740210302`.

[106] R. A. B. Devine and J. Arndt, *Si–O bond-length modification in pressure-densified amorphous SiO₂*, Physical Review B **35** (1987), 9376 – 9379, `http://dx.doi.org/10.1103/PhysRevB.35.9376`.

[107] K. Gabrovska, I. Marinov, T. Godjevargova, M. Portaccio, M. Lepore, V. Grano, N. Diano, and D. G. Mita, *The influence of the support nature on the kinetics parameters, Iinhibition constants and reactivation of immobilized acetylcholinesterase*, International Journal of Biological Macromolecules **43** (2008), 339 – 345, `http://dx.doi.org/10.1016/j.ijbiomac.2008.07.006`.

[108] J. B. Furness, *The enteric nervous system and neurogastroenterology*, Nature Reviews Gastroenterology and Hepatology **9** (2012), 286 – 294, `http://dx.doi.org/10.1038/nrgastro.2012.32`.

[109] E. Pouokam, M. Rehn, and M. Diener, *Effects of $H_2O_2$ at rat myenteric neurones in culture*, European Journal of Pharmacology **615** (2009), 40 – 49, `http://dx.doi.org/10.1016/j.ejphar.2009.04.066`.

[110] A. Kambadakone, A. Thabet, D. A. Gervais, P. R. Mueller, and R. S. Arellano, *CT-guided celiac plexus neurolysis: A review of anatomy, indications, technique, and tips for successful treatment*, RadioGraphics **31** (2011), 1599 – 1621, `http://dx.doi.org/10.1148/rg.316115526`.

[111] G. L. Ellman, K. Courtney, V. A. jr., and R. M. Featherstone, *A new and rapid colorimetric determination of acetylcholinesterase activity*, Biochemical Pharmacology **7** (1961), 88 – 95, `http://dx.doi.org/10.1016/0006-2952(61)90145-9`.

[112] S. Jamasb, S. Collins, and R. L. Smith, *A physical model for drift in pH ISFETs*, Sensors and Actuators B: Chemical **49** (1998), 146 – 155, `http://dx.doi.org/10.1016/S0925-4005(98)00040-9`.

[113] G. Grynkiewicz, M. Poenie, and R. Y. Tsien, *A new generation of $Ca^{2+}$ indicators with greatly improved fluorescence properties*, Journal of Biological Chemistry **260** (1985), 3440 – 3450.

[114] G. Huber and A. Matus, *Differences in the cellular distributions of two microtubule-associated proteins, MAP1 and MAP2, in rat brain*, The Journal of Neuroscience **4** (1984), 151 – 160.

[115] S. Glab, R. Koncki, and A. Hulanicki, *Kinetic model of pH-based poten-tiometric enzymic sensors. Part 3. Experimental verification*, Analyst **117** (1992), 1675 – 1678, http://dx.doi.org/10.1039/AN9921701675.

[116] Y. Klemes and N. Citri, *Preparation and properties of an immobilized derivative of penicillinase*, Biotechnology and Bioengineering **21** (1979), 897 – 905, http://dx.doi.org/10.1002/bit.260210512.

[117] S. G. Waley, *The pH-dependence and group modification of beta-lactamase I*, Biochemical Journal **149** (1975), 547 – 551, http://dx.doi.org/10.1042/bj1490547.

[118] J. P. Hou and J. W. Poole, *β-lactam antibiotics: Their physic-ochemical properties and biological activities in relation to struc-ture*, Journal of Pharmaceutical Sciences **60** (1971), 503 – 532, http://dx.doi.org/10.1002/jps.2600600402.

[119] P. Proctor, N. P. Gensmantel, and M. I. Page, *The chemical re-activity of penicillins and other β-lactam antibiotics*, Journal of the Chemical Society, Perkin Transactions 2 (1982), 1185 – 1192, http://dx.doi.org/10.1039/P29820001185.

[120] Y. Bourne, J. Grassi, P. E. Bougis, and P. Marchot, *Conformational flexibility of the acetylcholinesterase tetramer suggested by X-ray crys-tallography*, Journal of Biological Chemistry **274** (1999), 30370 – 30376, http://dx.doi.org/10.1074/jbc.274.43.30370.

[121] H.-J. Nolte, T. L. Rosenberry, and E. Neumann, *Effective charge on acetylcholinesterase active sites determined from the ionic strength dependence of association rate constants with cationic ligands*, Biochemistry **19** (1980), 3705 – 3711, http://dx.doi.org/10.1021/bi00557a011.

[122] F. Guo, J. Huynh, G. I. Dmitrienko, T. Viswanatha, and A. J. Clarke, *The role of the non-conserved residue at posi-tion 104 of class A β-lactamases in susceptibility to mechanism-based inhibitors*, Biochimica et Biophysica Acta (BBA) - Pro-tein Structure and Molecular Enzymology **1431** (1999), 132 – 147, http://dx.doi.org/10.1016/S0167-4838(99)00048-5.

[123] J. M. González, M.-R. Meini, P. E. Tomatis, F. J. M. Martín, J. A. Cricco, and A. J. Vila, *Metallo-β-lactamases withstand low Zn(II) con-*

*ditions by tuning metal-ligand interactions*, Nature Chemical Biology **8** (2012), 698 – 700, `http://dx.doi.org/10.1038/nchembio.1005`.

[124] J.-M. Contreras, Y. M. Rival, S. Chayer, J.-J. Bourguignon, and C. G. Wermuth, *Aminopyridazines as acetylcholinesterase inhibitors*, Journal of Medicinal Chemistry **42** (1999), 730 – 741, `http://dx.doi.org/10.1021/jm981101z`.

[125] W. Linke and G. Pfitzer, *Kontraktionsmechanismen*, R. F. Schmidt, F. Lang, and M. Heckmann, editors, *Physiologie des Menschen mit Pathophysiologie*, 31$^{\text{st}}$ edition (Springer, 2010).

[126] D. Kalamida, K. Poulas, V. Avramopoulou, E. Fostieri, G. Lagoumintzis, K. Lazaridis, A. Sideri, M. Zouridakis, and S. J. Tzartos, *Muscle and neuronal nicotinic acetylcholine receptors*, FEBS Journal **274** (2007), 3799 – 3845, `http://dx.doi.org/10.1111/j.1742-4658.2007.05935.x`.

[127] D. E. Goeger, R. T. Riley, J. W. Dorner, and R. J. Cole, *Cyclopiazonic acid inhibition of the $Ca^{2+}$-transport ATPase in rat skeletal muscle sarcoplasmic reticulum vesicles*, Biochemical Pharmacology **37** (1988), 978 – 981, `http://dx.doi.org/10.1016/0006-2952(88)90195-5`.

[128] W. G. Telford, L. E. King, and P. J. Fraker, *Comparative evaluation of several DNA binding dyes in the detection of apoptosis-associated chromatin degradation by flow cytometry*, Cytometry **13** (1992), 137 – 143, `http://dx.doi.org/10.1002/cyto.990130205`.

[129] J.-C. Chou and C.-Y. Weng, *Sensitivity and hysteresis effect in $Al_2O_3$ gate pH-ISFET*, Materials Chemistry and Physics **71** (2001), 120 – 124, `http://dx.doi.org/10.1016/S0254-0584(00)00513-7`.

# List of Publications

J. M. Philipps, G. M. Müntze, P. Hille, J. Wallys, J. Schörmann, J. Teubert, D. M. Hofmann, and M. Eickhoff, *Radical formation at the gallium nitride nanowire-electrolyte interface by photoactivated charge transfer*, Nanotechnology **24** (2013), 325701-1 – 325701-5, `http://dx.doi.org/10.1088/0957-4484/24/32/325701`.

G. M. Müntze, B. Baur, W. Schäfer, A. Sasse, J. Howgate, K. Röth, and M. Eickhoff, *Quantitative analysis of immobilized penicillinase using enzyme-modified AlGaN/GaN field-effect transistors*, Biosensors and Bioelectronics **64** (2015), 605 – 610, `http://dx.doi.org/10.1016/j.bios.2014.09.062`.

G. M. Müntze, E. Pouokam, J. Steidle, W. Schäfer, A. Sasse, K. Röth, M. Diener, and M. Eickhoff, *In situ monitoring of myenteric neuron activity using acetylcholinesterase-modified AlGaN/GaN solution-gate field-effect transistors*, Biosensors and Bioelectronics **77** (2016), 1048 – 1054, `http://dx.doi.org/j.bios.2015.10.076`.

114

# List of Scientific Contributions

G. M. Müntze, A. Sasse, W. Schäfer, and M. Eickhoff, *AlGaN/GaN enzyme-modified field-effect transistors for analysis of enzyme functionality*, presentation, 21ˢᵗ Workshop on Heterostructure Technology 2012, Barcelona, Spain.

G. M. Müntze, W. Schäfer, K. Röth, A. Sasse, and M. Eickhoff, *AlGaN/GaN enzyme-modified field-effect transistors for analysis of enzyme functionality*, presentation, DPG Spring Meeting of the Condensed Matter Section 2013, Regensburg, Germany.

G. M. Müntze, W. Schäfer, K. Röth, A. Sasse, and M. Eickhoff, *AlGaN/GaN enzyme-modified field-effect transistors for analysis of enzyme functionality*, poster presentation, 6ᵗʰ Annual GGL Conference 2013, Gießen, Germany.

G. M. Müntze, E. Pouokam, J. Steidle, W. Schäfer, K. Röth, A. Sasse, M. Diener, and M. Eickhoff, *AlGaN/GaN acetylcholinesterase-modified field-effect transistors for monitoring of myenteric neuron activity* , presentation, MRS Spring Meeting 2014, San Francisco, USA.

G. M. Müntze, E. Pouokam, J. Steidle, W. Schäfer, K. Röth, A. Sasse, M. Diener, and M. Eickhoff, *AlGaN/GaN acetylcholinesterase-modified field-effect transistors for monitoring of neuronal activity*, poster presentation, 7ᵗʰ Annual GGL Conference 2014, Gießen, Germany.

G. M. Müntze, E. Pouokam, J. Steidle, W. Schäfer, K. Röth, A. Sasse, M. Diener, and M. Eickhoff, *AlGaN/GaN acetylcholinesterase-modified field-effect transistors for monitoring of neuronal activity*, presentation, 23ʳᵈ Workshop on Heterostructure Technology 2014, Schloss Rauischholzhausen, Germany.

E. Pouokam, G. M. Müntze, M. Diener, and M. Eickhoff, *Multifunctional screening of cell transistor hybrid systems with enzyme-modified AlGaN/GaN-type field effect transistor arrays*, presentation, 26th Meeting of the European Intestinal Transport Group 2014, Marstrand, Sweden.

G. M. Müntze, E. Pouokam, J. Steidle, W. Schäfer, K. Röth, A. Sasse, M. Diener, and M. Eickhoff, *AlGaN/GaN acetylcholinesterase-modified field-effect transistors for monitoring of neuronal activity*, presentation, 8th Annual GGL Conference 2015, Gießen, Germany.

# Selbstständigkeitserklärung

Ich erkläre: Ich habe die vorgelegte Dissertation selbstständig und ohne unerlaubte fremde Hilfe und nur mit den Hilfen angefertigt, die ich in der Dissertation angegeben habe. Alle Textstellen, die wörtlich oder sinngemäß aus veröffentlichten Schriften entnommen sind, und alle Angaben, die auf mündlichen Auskünften beruhen, sind als solche kenntlich gemacht. Ich stimme einer evtl. Überprüfung meiner Dissertation durch eine Antiplagiat-Software zu. Bei den von mir durchgeführten und in der Dissertation erwähnten Untersuchungen habe ich die Grundsätze guter wissenschaftlicher Praxis, wie sie in der Satzung der Justus-Liebig-Universität Gießen zur Sicherung guter wissenschaftlicher Praxisniedergelegt sind, eingehalten.

Gießen, den 11.03.2016

_____

Gesche Mareike Müntze